NORTHWESTERN UNIVERSITY

Towards Understanding Plasmon-Molecule Interactions using Raman Spectroscopy

A DISSERTATION

SUBMITTED TO THE GRADUATE SCHOOL
IN PARTIAL FULFILLMENT OF THE REQUIREMENTS

for the degree

DOCTOR OF PHILOSOPHY

Field of Chemistry

By

Tyler W. Ueltschi

EVANSTON, ILLINOIS

June 2020

Copyright by Tyler W. Ueltschi 2020
All Rights Reserved

ABSTRACT

Towards Understanding Plasmon-Molecule Interactions using Raman Spectroscopy

Tyler W. Ueltschi

The unique ability of plasmonic nanoparticles to localize and enhance resonant electromagnetic fields has enabled a wealth of discoveries from enhanced spectroscopies to driving chemical reactions on the nanoscale. In this thesis, we strive to both drive and observe chemistry on plasmonic surfaces. First, we examine the possibility of driving the environmentally relevant reaction of carbon dioxide reduction to carbon monoxide using a plasmon driven electrochemical system. Then the interplay between hot carrier transfer and local heating are investigated during the process of plasmon driven ferrocyanide oxidation using environmental temperature control. Efforts towards driving and observing plasmon driven chemistry with ultrafast laser excitation were made, but ultimately the frequency and efficiency of plasmon driven reactions limited these attempts. With this in mind, we demonstrate time resolved surface-enhanced femtosecond stimulated Raman spectroscopy (SE-FSRS) using the time dependent response of the gold nanoparticle oligomers to plasmon excitation. This appears as transient depletion in the SE-FSRS gain that recovers over the course of picoseconds. The final work presented uses excitation dependent Raman spectroscopy to probe the hybrid resonances of a strongly couple j-aggregate/plasmon system. In this experiment we find that while the UV-vis extinction measurements show large Rabi splitting, the Raman excitation

profiles largely peak between the two split resonances indicating the largest degree of molecule plasmon interaction lies near the original contributing resonances. With this work we hope to advance the field of plasmonics by enabling new spectroscopic techniques and providing insight towards the mysteries of plasmon driven chemistry.

Professor Richard P. Van Duyne
Research Advisor

Professor George C. Schatz
Research Advisor

Acknowledgements

The first person I want to acknowledge and thank is Richard P. Van Duyne. I could not have asked for a better advisor and friend. He always made an effort to connect with his students beyond the lab whether it was our Friday beer hours, March madness beer brackets, or group BBQ's. This sense of openness and comradery, along with Rick's sharp sense for opportunity, drove our success. I always knew his favorite quote to be, "Serendipity favors the prepared mind," (Louis Pasteur). Rick was always a prepared mind, living on the forefront of spectroscopic technique development and plasmonics. Without his knowledge and insight, the field of plasmon enhanced spectroscopy would not be what it is today. For the opportunities and knowledge he gave me, I will be forever grateful.

Through all of the good times and bad I've had an excellent group of lab mates. I want to specifically thank Hannah Mayhew for being an excellent friend through this all and listening to me complain even after leaving Northwestern. I have to thank Michael McAnally for always giving me spot-on personal and professional advice despite the fact that I rarely listen. I also have to thank Yue Qi and Yue Wu, both of which I was supposed to mentor; however, in the end I believe they taught me way more than I could have taught them. I sincerely appreciate their willingness to try anything I asked of them and for working hard in the best and worst of times.

Finally, I have to thank my family. Throughout these five years in Chicago I've missed my home in the Pacific Northwest. I have to thank my Mom for giving me every opportunity to travel home and spend time with my family, she has always been my number one supporter. I could never say enough to thank her for everything she has given me. I want to thank my brother,

Justin, and Bob for getting me through the toughest of days. For more than a year, every Friday and Saturday night they would Facetime me so we could spend time together and I could feel more at home. Last but not least, I have to thank my friends in Chicago, David and Jasmin, for all the hours we spent playing Pokémon or hanging out at my apartment, you were always there whenever I needed a friend.

Dedication

This work is dedicated to my Mom, for without her unconditional love and support this would not have been possible.

Table of Contents

List of Figures

CHAPTER 1

Introduction to Plasmonics, Raman Scattering, and Plasmon Driven Chemistry

1.1 Abstract

This chapter introduces the key concepts and techniques that are utilized in this body of work. First an introduction to the concept of plasmonics will be presented, which gives a foundation for the plasmon coupled experimental techniques that follow. Spectroscopic techniques are first described in detail without the added complexity of the plasmonic component, then revisited to highlight the effects of coupling a molecular species to a plasmonic one. The main effect observed is plasmonic enhancement which confines and intensifies electromagnetic radiation at plasmonic hot spots allowing for large increases in the spectroscopic signal and in some cases initiating chemical reactions on the nanoparticle surface. Through an overview of both spontaneous and coherent Raman techniques, a spectroscopic perspective of plasmonic enhancement is given. Later, exploring the emergence of plasmon driven chemistry will elucidate possible chemical applications of plasmonic excitation.

1.2 Introduction to Plasmonics and Plasmonic Enhancement

A plasmon is defined as a coherent oscillation of the conduction band electrons. In order for a material to be deemed plasmonic at a given wavelength, the generation of this oscillation must be feasible upon excitation with an incident photon[1]. The presence of such a resonance is dictated by the dielectric function of the material. If a material has a negative real portion of the dielectric constant and a near zero imaginary portion, then a surface plasmon can be efficiently excited. This condition is met for gold and silver in the visible range, copper in the near infrared, and aluminum in the ultraviolet region.[2, 3] For flat surfaces exciting a plasmon requires sufficient

momentum of the incoming wavevector, which can be accomplished using a grating on the surface.[1] Or through using attenuated total reflection via a prism at the surface, which gives the incoming wavevector an imaginary component perpendicular to the plasmonic surface that can efficiently couple with a plasmon resonance.[1] This type of plasmon resonance is known as a surface plasmon-polariton (SPP), which can also be referred to as a propagating surface plasmon resonance due to the fact that the oscillation of the electrons actually translates across the surface of the material in the direction of the momentum until it is eventually dampened over the distance of nanometers to microns, depending on the material. The application of SPPs range from detection of small molecules[4, 5] to quantum information sciences[6, 7]; however, the body of this thesis is based on a second type of plasmon oscillation, the Localized Surface Plasmon (LSP) (Figure 1.1).

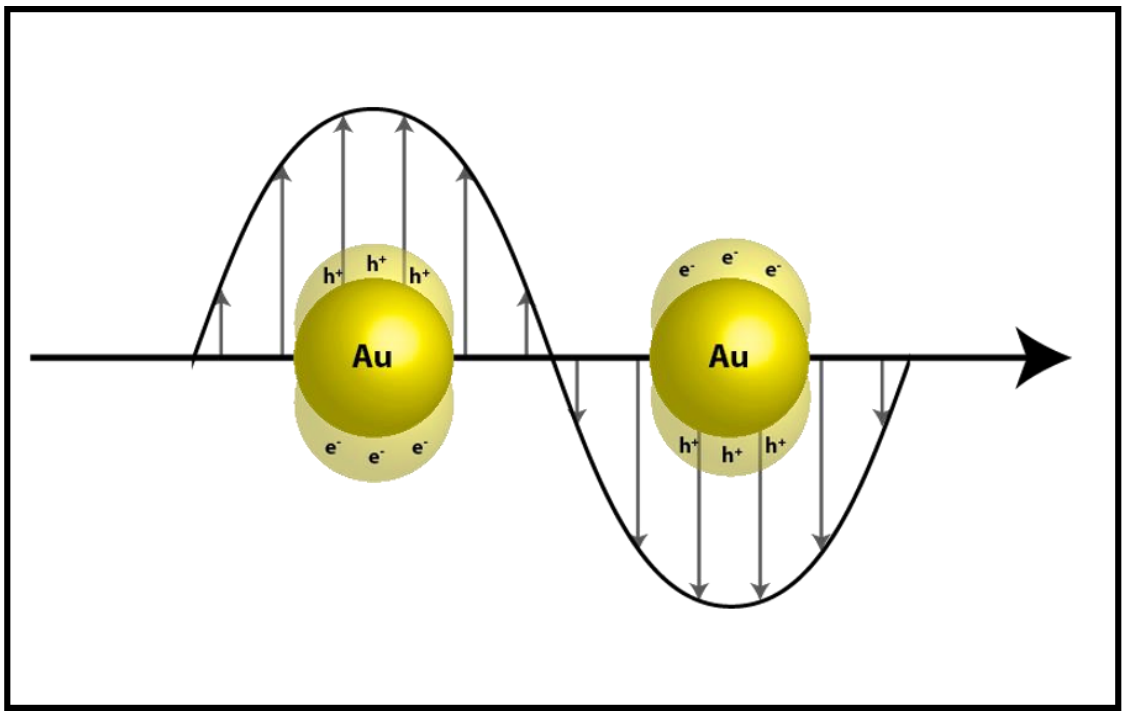

Figure 1.1 Illustration depicting the collective oscillation of conduction band electrons when excited by and electromagnetic field with wavelength much greater than the particle dimensions leading to a localized surface plasmon resonance.

For a material to have a localized surface plasmon resonance (LSPR) at a given wavelength, the dielectric conditions outlined above must be met and the surface of the material must be confined to a dimension much shorter than the wavelength of light used to excite the resonance. For an LSPR the electron oscillation does not propagate but is instead confined to the surface of the nanostructure. This interaction with light results in highly enhanced local electric fields on the nanoparticle surface. The intensity and spatial extent of the local fields are dictated by the wavelength and polarization of the incident light as well as the material and nanoparticle/nanoaggregate geometry.[8, 9] A few examples of local electric field distributions are shown in Figure 1.2 for reference.[3] The degree of localization and spatial distribution of the local electromagnetic field is strongly dependent on the geometry of the nanoparticle, which directly follows from Mie theory.[10] Therefore, by tuning the size and shape of the nanoparticle structures, light can be strategically localized to dimensions much smaller than its wavelength, which results in many interesting physical properties and applications.

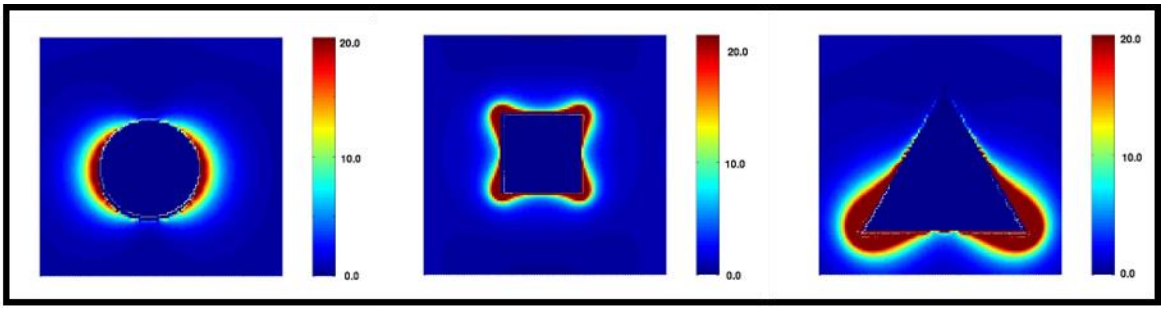

Figure 1.2. Calculated local electric field distributions for select nanoparticle geometries. Adapted from ref[3]. Copyright 2005 Materials Research Society.

The most direct of those properties and the true core of this research is plasmonic enhancement. This is simply a shorter way of stating the physics described in the previous paragraph, that is the localization of electromagnetic radiation leads to very high field strengths confined to very small dimensions, which in turn can probe or excite molecules nearby with high efficiency.[11] The most widely known application of this was realized in 1977 by Professor Richard P. Van Duyne, who discovered Surface Enhanced Raman Scattering (SERS).[12] This technique utilizes nanostructure plasmonic materials to enhance the efficiency of Raman scattering by a factor of up to 10^8.[13] While this is by far the most popular spectroscopic application of plasmonic enhancement, the principal is universal and thus can and has been applied to many different spectroscopic techniques including, but not limited to, SFG,[14, 15] FSRS,[16] CARS,[17] IR Absorption,[18] Fluorescence.[19]

Also, as will be discussed later in more detail, these highly localized fields can be used to generate non-equilibrium electron distributions at the nanoparticle surface to drive subsequent chemical reactions.[20] Since the early discovery of LSPRs and plasmonic enhancement, research efforts have elucidated many properties of the plasmonic nanoparticles such as field distributions dependent on geometry and excitation, but there is still much work to be done on plasmonic interactions with molecules and their possible application towards driving and observing chemical reactions.

1.3 Introduction to Raman Scattering Techniques

Raman scattering is a vibrational spectroscopy technique that probes the induced dipole of a vibrational normal mode. For a vibrational normal mode to be Raman active it must cause a

change in the molecular polarizability. This condition is met for totally symmetric vibrations, which are not accessible through infrared absorption measurements, as well as many non-symmetric vibrational modes. This also means all molecules have at least one Raman active vibrational mode, making it an ideal technique for molecule identification. In this inelastic scattering technique, the incoming Raman excitation photon exchanges a small amount of energy with the molecule equivalent the energy of a Raman active vibrational mode.[21] The incident photon is then red shifted or blue shifted, depending if energy was lost or gained to the molecule which is known as Stokes or anti-Stokes shifting, respectively (Figure 1.3). This shift in photon frequency can then be measured using a spectrometer to determine the vibrational energy levels of the molecular species. Stokes Raman scattering is an inherently weak process and occurs at a rate of approximately one in one million photons. While anti-Stokes Raman scattering is even weaker due to low population of excited vibrational states at room temperature. Given that Stokes and anti-Stokes events are interrelated based on the population of the vibrational normal modes, a proper measure of the Stoke/anti-Stokes ratio allows for a measure of the local temperature based on the Boltzmann distribution.[22, 23] While normal Raman spectroscopy (NRS) is a powerful technique, it largely suffers from inefficient signal generation.

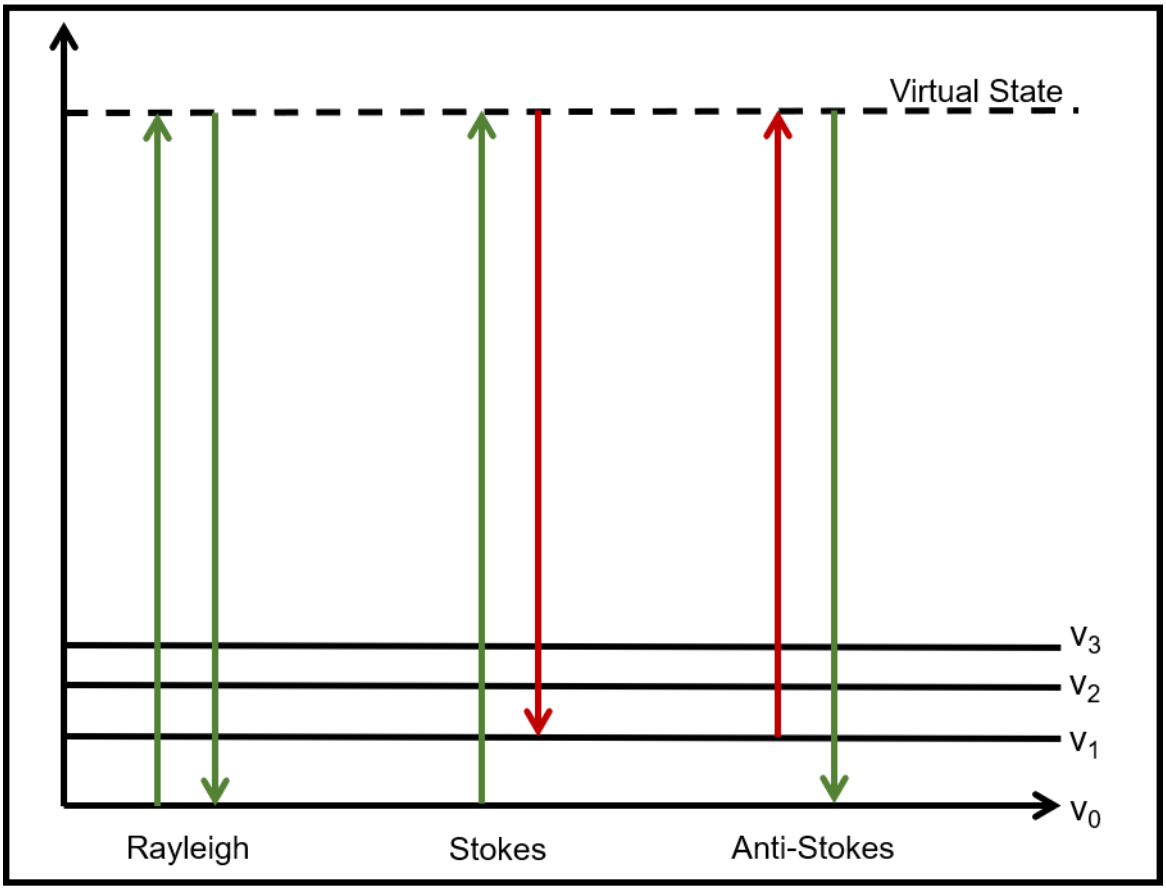

Figure 1.3. Energy level diagram of the relevant states in the normal Raman scattering process. Energy levels $v_{0\text{-}3}$ represent the vibrational energy levels of the molecular species. Both elastic and inelastic scattering events are depicted in terms of Rayleigh and Stoke/anti-Stokes events, respectively.

To overcome these limitations a large amount research has gone into exploiting the plasmonic enhancement of noble metal nanoparticles to increase Raman cross sections by factors of up to 10^8.[13] This technique is referred to as surface-enhanced Raman scattering (SERS). As implied by the name, in order to couple the nearfield plasmonic enhancement to a molecule of interest, the molecule must be on or near the surface of the plasmonic material.[24] By tailoring the size and composition of the nanostructured substrate, the LSPR can be tuned to a desired frequency

in order to achieve maximum coupling with the far field light.[3] Since the enhancement originates in the electromagnetic field, all photon interactions are enhanced by the plasmonic substrate given the interaction is sufficiently close to the surfaces and overlaps with an LSPR.[11] For Raman specifically, it indicates that for optimal enhancement the overlap of both the incident wavelength and the Stokes scattered wavelength with the LSPR should be considered. In practice this requirement is quite lose because the LSPR are often very broad compared to the separation between the incident and scattered photons. While the enhancements from this technique are very enticing, the high field strengths created at the plasmonic surface can easily alter the molecules of interest if you are not careful.

Another way the weak scattering cross section of the Raman process has been augmented is through excitation of a molecular resonance. When an incident photon is resonant with an electronic transition of the analyte, Raman scattering from the vibrational normal modes aligned along the transition dipole is increased by factors up to 10^3.[25] This technique is convenient when an electronic transition in the visible range is present, but it cannot be easily tuned like the LSPR. Also, excitation of the electronic transition can lead to fluorescence in some molecules that will quickly obfuscate the relatively weak Raman scattering signal.

A related technique that is useful to probe the fundamental characteristics of both plasmonic and molecular resonances from a Raman perspective is Raman excitation spectroscopy (RES), which is often referred to with respect to the resonances that are being observed such as resonance Raman excitation spectroscopy (RRES)[26, 27] and Surface-enhanced Raman excitation spectroscopy (SERES).[28] In this technique, by measure the Raman scattering signal from various

vibrational modes as a function of Raman excitation wavelengths the relative Raman enhancement can be deduced across the excitation range. The peaks in relative Raman enhancement directly indicate the presence of either molecular or plasmonic resonances. Since their enhancement scales differently with excitation and scattered photon frequencies, with a comprehensive study the two resonances can be distinguished, offering a more direct measure of the near-field picture.

While these techniques all utilize continuous wave (cw) lasers, a second group of Raman techniques using pulsed lasers has been developed in effort to observe molecular dynamics on the picosecond (ps) to femtosecond (fs) timescale. For each of the techniques discussed above, there is a spontaneous ultrafast technique that can be achieved by replacing the cw laser with a narrowband pulsed laser at the same frequency; in ultrafast measurements this is referred to as the Raman probe. For spontaneous ultrafast techniques the pulse duration of the Raman probe is ultimately limited by the uncertainty principle and the spectral resolution necessary to resolve the vibrational modes of interest. This effectively limits the pulse duration to values above one picosecond. In order to measure and clock dynamics in an ultrafast measurement, the dynamics must be initiated by an actinic pulse. This pulse has no effect on the final spectral resolution, so effectively it can be as short, or as long, as desirable for the experiment. Since the actinic pulse initiates the dynamics that are measured by the Raman probe, the instrument response time will be determined by the cross-correlation between the actinic and Raman probe pulses. Due to the limitations on the Raman probe side, the fastest instrument response time possible for a spontaneous ultrafast experiment is about one picosecond. This group of experiments includes but is not limited to the following: ps-ps pump-probe Raman spectroscopy,[29-31] fs-ps pump-probe Raman spectroscopy,[32] and time resolved resonance Raman spectroscopy.[33, 34] These techniques

also suffer from the low cross sections present in cw Raman scattering experiments so they often require high power densities and/or high analyte concentrations, but they do provide vibrational information that can be directly correlated to the molecular dynamics occurring during a reaction or excited state transition, providing a compliment to transient absorption experiments. Additionally, a large amount of signal loss from spontaneous Raman scattering experiments comes from the inherent nature of the process. That is, interacting photons are isotropically scattered, thus to collect all the signal you must collect light imitating in every possible direction from your sample. While there are experimental configurations that increase the maximum angle of collection using parabolic mirrors, it is impractical if not impossible to collect all the light.

Through the development of coherent Raman techniques, many limitations of spontaneous Raman experiments have been overcome. In a coherent Raman experiment, a vibrational coherence is initiated by a Raman pump probe pulse pair whose frequency difference is equivalent to the vibrational mode to be driven. Then a subsequent interaction with the Raman probe pulse stimulates the emission of a vibrationally shifted photon, which is often heterodyned with the probe pulse. This means the signal from this process is coherent and reliant on both Raman pump and probe pulses being overlapped in space and time allowing for a wider range of signal collection and processing capabilities. The simplest coherent Raman technique is stimulated Raman scattering (SRS) where a narrow band Raman pump and probe are used with a frequency difference precisely matched to the vibrational mode of interest. To measure the Raman cross-section, the pump or probe is chopped at a given frequency and the resulting modulation in the opposing pulse is measured to give the strength of the interaction at that frequency. Combined with lock-in detection this can be a very rapid and efficient technique useful for bioimaging and kinetics

measurements. The downside to this type of SRS is in order to measure different vibrational frequencies, you must tune the frequency difference between the two narrowband pulses.

The most recently developed technique in this subsection of Raman experiments is Femtosecond Stimulated Raman Spectroscopy (FSRS). While this technique follows in the same vein as the experiments described above, it presents some unique advantages. In these coherent experiments the Raman pump consists of a narrow band (ps) pulse while the probe is a stokes shifted broadband femtosecond continuum. The broadband pulse in this experiment allows for collection of the entire vibrational spectrum in a single shot, while the narrow band Raman pump provides the spectral resolution necessary to resolve the vibrational modes. Also, since the probe stimulates the emission of the signal photons, its cross correlation with the actinic pulse is what determines the instrument response time. So, the FSRS technique effectively separates the spectral and temporal components so the ultimate limits for optical spectroscopy can be approached.

1.4 Introduction to Plasmon Driven Chemistry

When a metal system is excited by electromagnetic radiation of sufficient energy, electrons from the conduction band are instantaneously promoted to energy levels above the Fermi level creating a non-equilibrium electron distribution consisting of high energy electrons (hot electrons) and positive vacancies (hot holes).[35] Molecules at the metal surface can then interact with these excited carriers, resulting in chemical processes such as oxidation, reduction, or desorption.[35] In the case of bulk metal substrates this process is inefficient due to the high reflectivity of most metals to visible irradiation.[35] However, by exploiting the high extinction cross section and ability

to localize electromagnetic fields of noble metal nanoparticles (NPs) this generation of hot carriers becomes an efficient process that can be used to drive chemistry on the nanoscale.[20, 36] This is a direct result of the fact that noble metal nanoparticles have a localized surface plasmon resonance (LSPR) in the visible region.[37] The LSPR is an oscillation of conduction band electrons generated when light interacts with NPs much smaller than the incident wavelength.[38] The decay of this plasmon resonance then results in a hot carrier distribution analogous to the bulk metal system, but with much higher efficiency with respect to incident laser intensity.[37] From this the ability to drive chemical reactions on NP substrates using visible light was realized.[36, 39-45] Now the field of plasmon driven chemistry has demonstrated applications including energy conversion[36, 44] and catalysis[39-43, 45] at the nanoscale.

With a large cross-section for light-matter interactions supported by their localized surface plasmon resonance (LSPR), plasmonic nanostructures have generated substantial interest as a promising candidate for capturing, harnessing, and converting solar energy[46-50]. Energetic hot carriers generated during plasmon decay can be transferred to surrounding molecules or semiconductors, inducing or enhancing processes such as photovoltaic current generation[51, 52] plasmon-mediated synthesis[53-56] and photocatalysis[57-60]. Conventionally, the yield of hot carrier generation, and thus the energy conversion efficiencies of most plasmon-based systems remain unsatisfying due to the existence of multiple competitive energy dissipating pathways inside plasmonic nanostructures[61, 62]. However, recent reports[63-66] have demonstrated that hot carrier generation and subsequent transfer to surrounding molecular species can be greatly enhanced within the sub-nanoscale gaps between aggregated noble metal nanoparticles. These plasmonic hot spots act to localize the incident electromagnetic field creating high power densities, enhancing

hot carrier generation and allowing for direct vibrational characterization of the molecular species present via surface-enhanced Raman spectroscopy (SERS).

The dimerization of nitrothiolphenol (NTP) to dimercaptoazobenzene (DMAB) has been heavily studied in the literature as a proof-of-principal demonstration of plasmon driven chemistry.[41-43] Initial studies utilized a degenerate continuous wave (cw) pump-probe scheme typically using 532 nm light and silver nanoparticles (NPs), which have an LSPR near the 532 nm pump, to drive and monitor the reaction.[41, 43] In these studies, the identifying observable is the disappearance of the vibrational mode attributed to the NO_2 group of NTP (around 1335 cm^{-1}) and the appearance of the N=N vibrational mode of DMAB (around 1380 and 1440 cm^{-1}).[42] Most report complete conversion of NTP to DMAB over the course of minutes.[43, 67] In addition one studies shows that red shifting the pump/probe wavelength from 532 nm to 633 nm results in ~100x slower reaction rates.[67] This body of work is important as a proof-of-principal in that reactions can be driven at nanoparticle surfaces. However, there have yet to be any ultrafast experiments to successfully drive and observe this reaction in order confirm the role of hot carriers despite attempts[65, 68].

Other experiments have demonstrate plasmon-driven electron transfer from gold nanosphere oligomers to bipyridine (BPY)[63] and bipyridyl ethylene (BPE)[64] molecules on the surface. The measurements utilize a cw pump-probe SERS technique that consisting of first pump the electron transfer events using a 532 nm cw laser source and then monitoring the local molecular population using SERS from a 785 nm cw probe. The results show that in the hot spot of the nanosphere oligomers, electrons are being transferred from the gold surface to BPY resulting in

the vibrational signature of the BPY radical anion appearing in the SERS spectra[63]. A follow up studying looking at a similar molecule, BPE, made a further effort to characterize not only plasmon-driven electron transfer events, but all observed spectral fluctuations. This work demonstrated that in addition to the generation of the BPE radical anion species, pumping the plasmon resonance lead to cis-trans isomerization and symmetry breaking more indicative of thermal processes[64]. These studies highlight the current state of plasmon driven chemistry from a fundamental experimental perspective in that much has been observed but there is still much to uncover.

CHAPTER 2

Towards Driving and Observing Carbon Dioxide Reduction via Plasmonics

2.1 Abstract

The unique capability of plasmonic nanoparticles to localize and enhance resonant electromagnetic fields has enabled a wealth of highly sensitive, surface-enhanced spectroscopic techniques. Furthermore, driving a plasmonic substrates localized surface plasmon resonance leads to generation of hot carriers that can be used to drive chemistry on the nanoscale. The decay of the plasmon resonance drives this hot carrier distribution, which cools on the picosecond timescale. Molecules at the metal surface can then interact with this non-equilibrium distribution resulting in chemical processes such as oxidation, reduction, or desorption.

In effort to use the photo-reductive/oxidative nature of these nanoparticle systems to drive the environmentally relevant process of carbon dioxide reduction to carbon monoxide, an electrocatalytic system was strategically selected. The rhenium bipyridine tricarbonyl chloride complex was selected because it is can be activated through both reductive and oxidative pathways, and it is a well-known catalyst of carbon dioxide reduction. Physisorbing the catalytic complex on spherical gold nanoparticles enables the plasmon driven chemical processes, which also allows for vibrational characterization of the molecular species using surface-enhanced Raman spectroscopy. Our results show that excitation of this system with 532 nm continuous wave irradiation results in chemical activity on the nanoparticle surface indicated by the appearance of transient vibrational modes measured by SERS with a 785 nm Raman probe. Appearance of sharp vibrational features at 2065 cm^{-1} and separately at 2110 cm^{-1} were attributed to CO adsorption on different sites on the gold nanoparticle surface. This indicates that we are able to drive chemistry using visible light excitation of the plasmonic nanoparticles. However, due to the complex nature of the reaction it is

difficult to say that carbon dioxide reduction to carbon monoxide was the direct cause of the spectroscopic signatures observed, as the free carbon monoxide could have been generated by many pathways.

2.2 Introduction

When a metal is excited by light, electrons from lower energy levels are promoted to energies above the fermi level creating an initial distribution consisting of hot electrons and hot holes (Figure 2.1).[35] In bulk metals generating this hot carrier distribution is inefficient due to high reflectivity of visible light, but plasmonic nanoparticles high scattering cross sections offer a more efficient route to this distribution. Upon excitation of a plasmonic nanoparticle, the dephasing of the plasmon resonance drives a hot carrier distribution which over hundreds of femtoseconds begins to cool through electron-electron scattering resulting in a thermalized distribution.[69] On the scale of picoseconds, the elevated electron temperature cools further through electron-phonon coupling resulting in a heating of the metal lattice and excitation of phonon modes that oscillate on the picosecond time scale.[70]

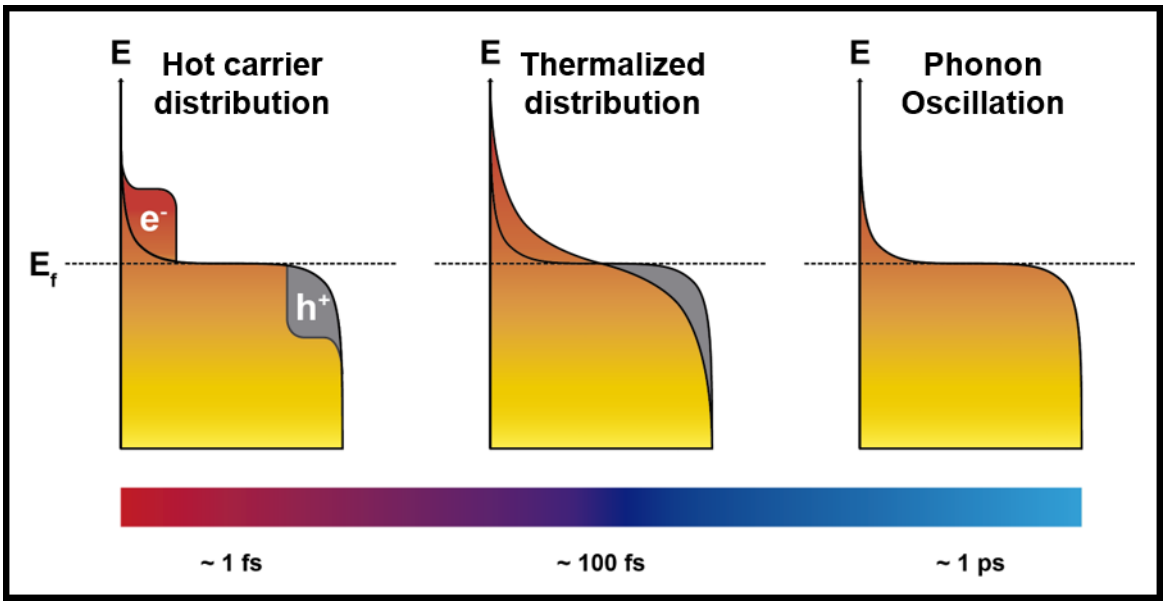

Figure 2.1. An illustration of a non-equillibrium electron distribution of a metal following excitation. Immediately following the excitation a hot carrier distribution is generated. This hot carrier distribution then begins to thermalize through electron-electron collisions over the course of about 100 femtoseconds. Then on the picosecond time scale electron-phonon coupling occurs resulting a cooling of the electrons and excitation of the metals phonon mode oscillations.

Recent research has demonstrated that these non-equilibrium distributions can be used to drive chemistry at the surface of plasmonic nanoparticles. One popular system is the dimerization of nitrothiolphenol (NTP) to dimercaptoazobenzene (DMAB).[41-43] In this experiment the authors show that irradiating silver nanoparticles with 532 nm light drives this dimerization over the course of minutes. They use surface enhanced Raman spectroscopy to monitor the progress of the reaction through the characteristic vibrations of the nitro-groups of NTP and the nitrogen-nitrogen double bond of DMAB. This reaction is of significance because it requires a 4-electron reduction indicating a strong dependence on the generated electron distribution.

Using similar methodologies efforts were made to examine the possibility of driving the environmentally relevant reaction of carbon dioxide reduction to carbon monoxide. The rhenium

bipyridine tricarbonyl chloride complex has been extensively researched over the past few decades because of its ability to perform this reaction under electrochemical conditions.[71-75] A simplified electrochemical cycle is shown in Figure 2.2. When the initial species is reduced by two electrons it loses the chlorine group, leaving an active site for carbon dioxide reduction. Alternatively, this chlorine binding site can be opened up by a one electron oxidation, from which the positively charged species needs to be reduced by 2 electrons to generate the active complex. Once the active species is generated the addition of 2 electrons and two protons reduces carbon dioxide resulting in the release of carbon monoxide and water. This represents a total of 4 electrons added to the molecular system, analogous to the dimerization of NTP.

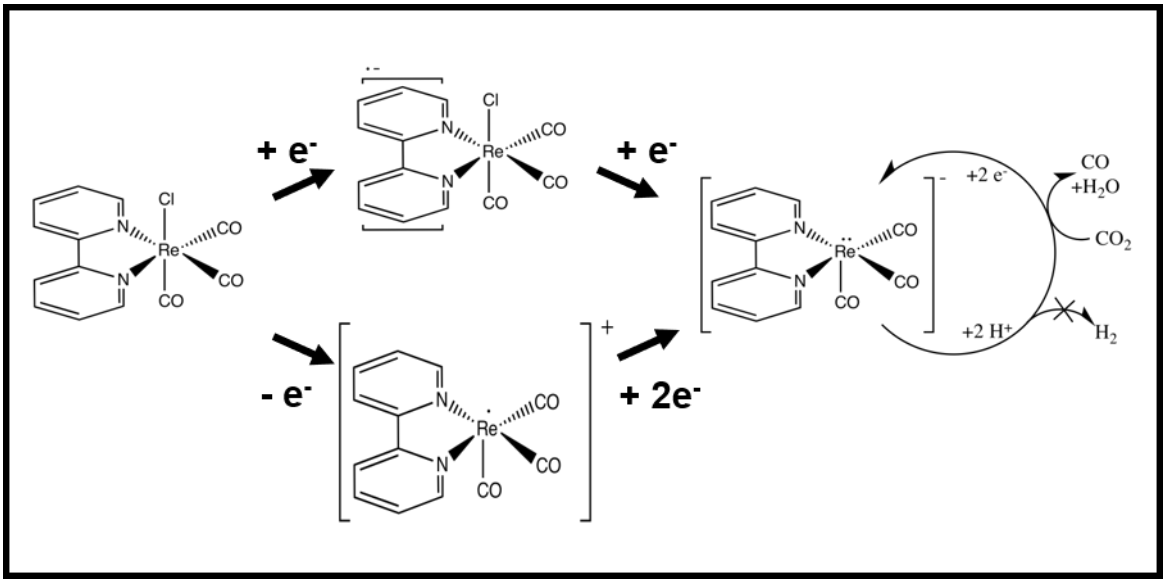

Figure 2.2. A simplified diagram of the electrochemical cycle for the rhenium bipyridine tricarbonyl chloride complex. Two main pathways lead to activation of the complex and subsequent carbon dioxide reduction.

Through methods pioneered by Sprague-Klein et. al.[63, 64] we probed the possibility of driving the electrochemical reaction via plasmonics using continuous wave (cw) pump-probe

SERS. By aggregating gold nanoparticles in the presence of the rhenium bipyridine tricarbonyl chloride complex, the molecular species was trapped in the plasmonic hotspot as evidenced by its SERS signature. The colloidal solution was then drop cast on a transmission electron microscopy (TEM) grid at low concentration to allow for interrogation of individual nanoparticle oligomers. Dark-field and cw pump-probe SERS measurements were done on selected particles, which were subsequently measured by TEM. From this we found the signature of carbon monoxide on the surface of the gold nanoparticles evidenced by sharp transient vibrational features upon plasmon excitation. However, this evidence is ultimately insufficient to confidently attribute the presence of carbon monoxide to the reduction of carbon dioxide through a plasmon driven pathway.

2.3 Experimental Methods

Colloidal sample preparation. Rhenium bipyridine tricarbonyl chloride functionalized gold nanoparticle oligomers were prepared by adding 40 µL of a saturated $Re(bpy)(CO)_3Cl$ (Sigma-Aldrich) solution in water to 2 mL of citrate capped 90 nm spherical gold nanoparticles (0.25 mg/mL, STA Technologies). Aggregation of the particles was monitored by UV-Visible extinction measurements using a benchtop spectrometer (Cary 5000, Agilent Technologies). Upon appearance of extinction at 950 nm, a 0.2 mL aliquot of 10 wt%/wt 55 kDa polyvinylpyrrolidone (PVP) solution in Milli-Q water (18.2 MΩ/cm) was added to the colloidal solution to halt aggregation.

Glass coverslip preparation. Microscope glass coverslips (VWR International, No.1, 25 mm diameter) underwent piranha treatment (3:1 H_2SO_4:30%H_2O_2) followed by thorough rinsing with Milli-Q water (18.2 MΩ/cm). Coverslips were then immersed in a base treatment, (5:1:1

H_2O:NH_4OH:30%H_2O_2), sonicated for sixty minutes, and again thoroughly rinsed with Milli-Q water. Sample grids were positioned on top of N2 dried coverslips and mounted on a sample stage above the microscope objective.

Single nanoparticle oligomer sample preparation. The prepared colloidal solution was diluted 100X with Milli-Q water (18.2 MΩ/cm) and were drop-casted onto 3 nm thick carbon/Formvar TEM grids (Ted Pella, Inc.). This allows for indexing and correlation of particles across dark-field, SERS, and TEM measurements.

Dark-field extinction measurements. Nanoparticle oligomers were imaged using dark-field optical microscopy with a dry condenser and a 100X/0.55 oil immersion microscope objective (Nikon Corporation) on an inverted microscope (Nikon Ti-U/E20L80) via a CCD camera (UNIQ vision, Inc.). The single nanoparticle oligomer extinction spectrum was collected by directing the scattered light from the nanoparticle oligomer to a spectrometer (Spectra Pro 2500i, Princeton Instruments) equip with a PIXIS 400 CCD (Princeton Instruments). The measure extinction is then normalized by the lamp profile to obtain the single aggregate scattering spectrum.

Single particle cw pump-probe SERS measurements. The experimental setup is configured such that a 785 nm cw laser (Renishaw Inc.) and 532 nm cw laser (Spectra-Physics) are focused through a 40x/0.60 objective (Nikon) overlapped at the focal plane of an inverted microscope ((Nikon Ti-U/E20L80). The 785 nm laser (10 $\mu W/\mu m^2$) was used to measure the SERS response of individual nanosphere oligomers. If the SERS signature of $Re(bpy)(CO)_3Cl$ is observed, the subsequent pump-probe measurement is performed. For this the nanoparticle oligomer is exposed to the 532nm laser (50 $\mu W/\mu m^2$) for a period of one second, after which the 532 nm laser is blocked and the SERS response is measure by the 785 nm pulse with an acquisition

time of one second. This process is iterated in sync with a USB shutter (Picard Industries) and triggered by the PIXIS 400 CCD camera mounted on a Spectra Pro 2500i spectrometer (Princeton Instruments). Data acquisition was automated with WinSpec (Princeton Instruments). A typical experiment captures approximately 250 SERS spectra following excitation by the 532 nm laser.

Transmission Electron Microscopy (TEM) Imaging. Following all spectroscopic measurements, single nanosphere oligomers were imaged using transmission electron microscopy (TEM). Scans were performed on a Hitachi 8100-TEM using 200 kV of thermionic emission and optimized aperture positions (Condenser = 1, Objective = 2, Selected area = 0).

Solution phase Raman measurements. Raman scattering spectra of the prepared colloidal solution and solutions of $Re(bpy)(CO)_3Cl$ in H_2O, DMSO, and ethanol were measured using a custom build Raman spectrometer. Excitation with a 785 nm cw laser (Renishaw Inc.) is done in a backscattering geometry. The backscattered light is focused into a Spectra Pro 2500i spectrometer equipped PIXIS 400 CCD (Princeton Instruments). Laser excitation is filtered with a 785 nm long pass (Thorlabs) before entering the spectrometer. Data collection is performed with WinSpec (Princeton Instruments).

2.4 Results and Discussion

In order to see the vibrational signature of a molecule via SERS, the molecule must be on or near the surface of the plasmonic substrate. An investigation in the distance dependence of plasmon enhancement has revealed that at a distance of 2 nm from the plasmonic surface there is a 90% reduction in the SERS signal measured.[24] Most of the time this is accomplished by using molecules with functional groups that preferentially chemi- or physisorb to the plasmonic surface.

For gold the best choices are thiols or pyridal groups. When a molecule with an affinity for the gold surface is mixed with a solution of gold nanoparticles, the molecules displace the capping ligands, in our case citrate, which causes instability in the system that leads to aggregation of the gold nanoparticles over time. The degree of affinity for the gold surface will dictate how quickly or slowly this process occurs, but eventually aggregation will lead to the particles precipitating from solution and losing their enhancement properties. In cases where the molecules do not have a natural affinity for the gold surface, there is not an issue with over aggregation; however, the molecules vibrational signature will be difficult to measure because the molecule is simply not close enough to the surface. Fortunately, both of the issues can be mitigated through simple techniques. To prevent over aggregation, we found that by adding a small amount of polyvinylpyrrolidone (PVP) the aggregation can be effectively paused.[76] This allows for a much more controlled aggregation process that can be tuned to produce more small aggregates (i.e. dimers and trimers) which yield the highest enhancement factors and are favorable for 785 nm excitation of gold.[13] The plasmon resonance can be easily monitored during the aggregation process by a simple UV-Vis extinction measurement, then stopped on demand with a 200 microliter addition of 10 wt%/wt 55 kDa PVP (Figure 2.3).

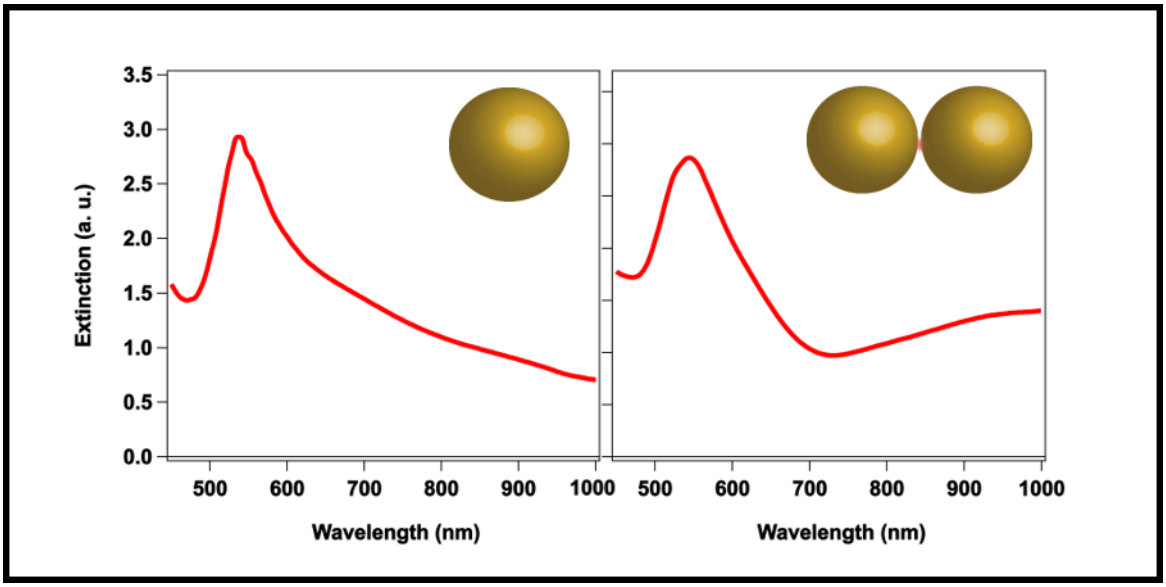

Figure 2.3. The left panel is the measured extinction of a colloidal solution of monomer 90 nm gold nanospheres. The right panel shows the extinction spectrum measured upon aggregation induced by addition of a molecular species, evidenced by the rise in extinction in the near infrared. At this point PVP is added to pause the aggregation.

This technique can be adjusted to accommodate molecules with a lower affinity for the gold surface, such as the Rhenium bipyridine tricarbonyl chloride complex. In this case when the molecule is added to the gold nanoparticle solution, no immediately noticeable aggregation occurs, both visually and as measured by UV-Vis extinction. Depending on the affinity of the molecule for the gold surface there are two approaches. If the molecule causes slight interaction with the gold surface, at high molecular concentrations and long wait times (~30 minutes) the particles will aggregate sufficiently and can be paused with the PVP addition. These samples often result in sufficient coupling between the molecule and plasmon to give high signal enhancement. If after this wait time the particles do not show any aggregation, a small amount of 10x PBS buffer solution can be added to induce aggregation,[77] which can then be held with the PVP addition. In this case your signal will be dictated by the number of molecules trapped between nanoparticles in the

aggregation process, thus the signal observed from these types of samples can vary widely from no signal observed for the least sticky of molecules to near optimal levels in more favorable situations. This is all to say that every molecule is different when trying to create a plasmonically enhanced sample, and that trial and error is required to reach the desired molecular concentrations on the surface as well as the degree of aggregation.

For the Rhenium bipyridine tricarbonyl chloride complex, the molecule does not have a high affinity for the gold surface. When the molecule was added to the gold nanoparticle solution there was no immediately noticeable aggregation. For this reason the concentration of the molecule in water was increased to near saturation (~1 mM) and the process repeated. After about 30 minutes the aggregation induced color shift occurred and the state was paused with a 200 microliter addition of PVP. This sample was then probed with a Raman spectrometer to confirm the presence of the Rhenium bipyridine tricarbonyl chloride complex on the surface of the nanoparticle aggregates (Figure 2.4). The measurement, when compared to DFT calculations performed by Dr. Michael McAnally, shows most of the signature vibrational modes; however, there is only two CO vibrational modes instead of the three observed experimentally. This hints that the surface species might be slightly altered electronically with respect to the species in solution. Since this is a highly active molecule electrochemically, the Raman spectra for possible electrochemical products were calculated. There was only one that exhibited three distinct CO vibrations, that molecule being the Rhenium bipyridine tetracarbonyl complex, $[Re(bpy)(CO)_4]^+$ (Figure 2.4). Further examination of the Rhenium bipyridine tricarbonyl chloride complex in solution and in solid form by standard Raman scattering measurements do not show this highly shifted carbonyl mode either (Figure 2.5). From this we conclude our surfaced species is most likely the tetracarbonyl complex indicating

reduction/oxidation when moving to the gold surface. Similar observations have been made in the plasmon driven NTP dimerization research, where the reaction partially completes after adsorption the gold surface[68, 78].

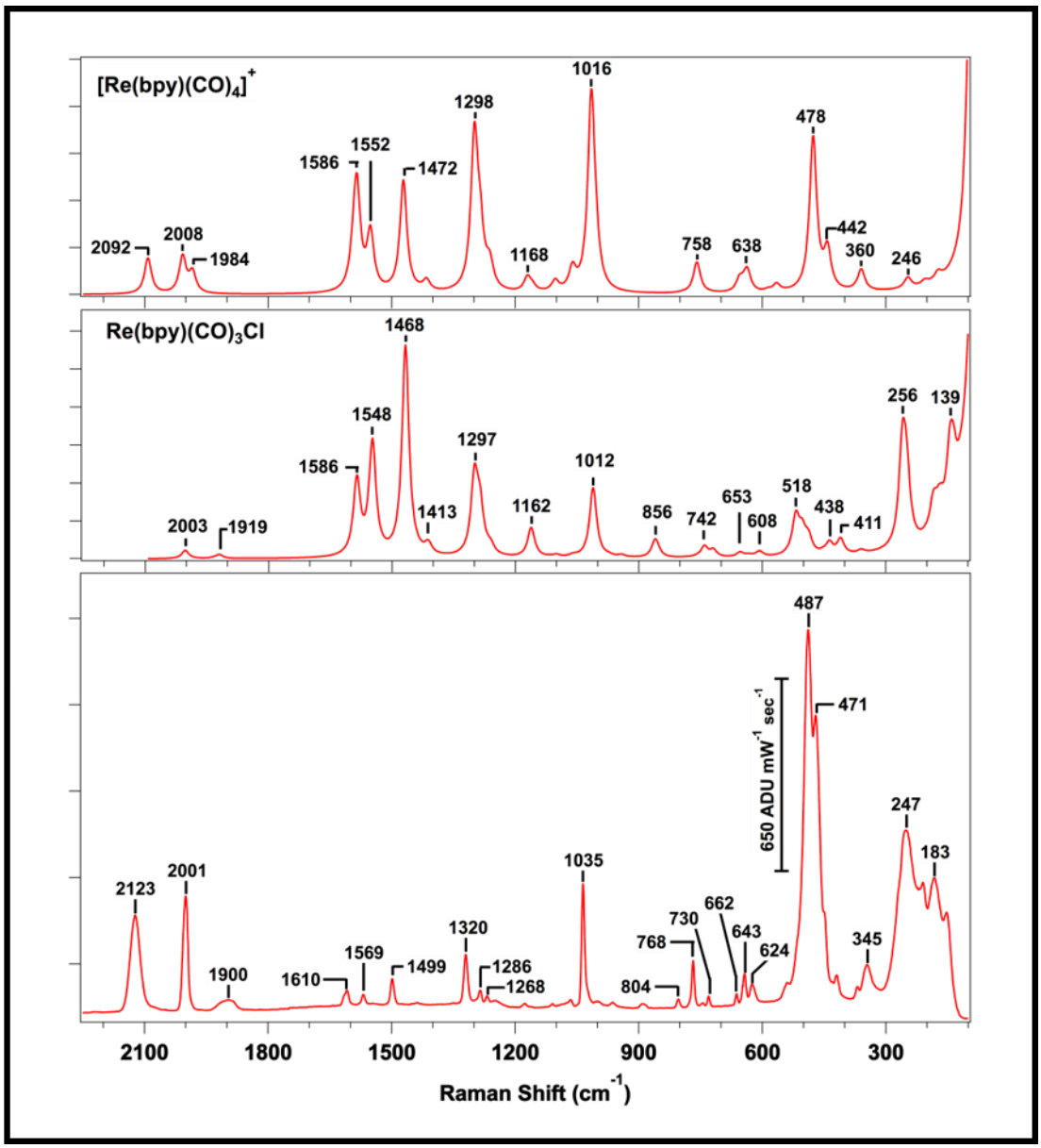

Figure 2.4. The bottom panel shows a SERS spectrum for the colloidal solution of $Re(bpy)(CO)_3Cl$ functionalized gold nanoparticles. The middle panel is a theoretical Raman spectrum of $Re(bpy)(CO)_3Cl$ calculated using DFT methods. The top panel displays the calculated Raman spectrum for the $[Re(bpy)(CO)_4]^+$ molecule.

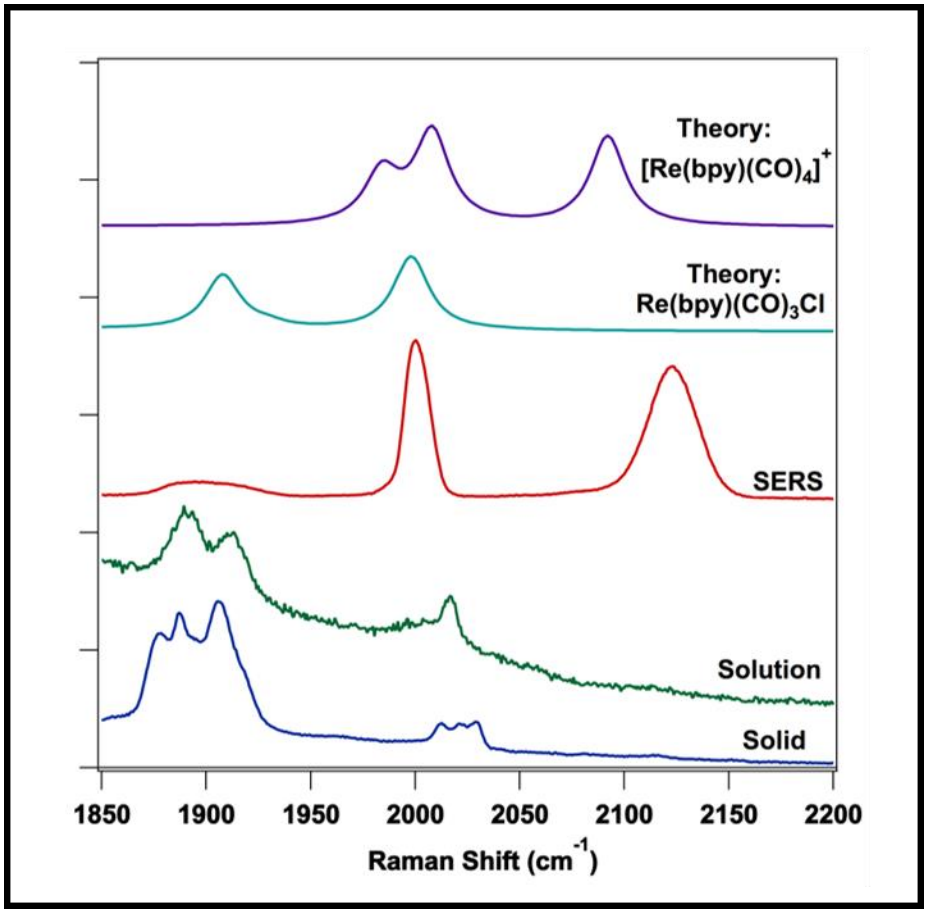

Figure 2.5. A comparison of $Re(bpy)(CO)_3Cl$ spectra in the high wavenumber region. In both solid phase and solution phase in water (~1mM) the peak at 2123 cm^{-1} observed in the SERS spectrum is not seen. The calculated spectrum for $Re(bpy)(CO)_3Cl$ closely matches the solution and solid phase spectra, while the calculated $[Re(bpy)(CO)_4]^+$spectrum more resembles the SERS peaks.

With the SERS active substrates made we were now primed to try to drive the reaction via plasmon excitation. For this our previously reported single aggregate continuous wave pump-probe SERS technique was implemented.[63, 64] The dilute colloidal sample was dropped on a TEM grid to allow for correlated LSPR, TEM and SERS measurements. For the experiments the TEM grid was positioned in a microscope and darkfield microscopy was used to measure the LSPR and locate particles. Then the chosen single aggregates, selected by observation of SERS signal, were

subjected to the pump probe scheme shown in Figure 2.6. The 532 nm pump irradiates the sample for 1 second, which is then blocked while the system is probed by a 785 nm laser. The 532 nm wavelength is chosen because it is of sufficient energy to promote electrons from the d band of gold and is near the peak of the monomer resonance.[79] The 785 nm wavelength is used as a probe because it gives high SERS signal with the gold aggregates and is low enough energy that it doesn't significantly perturb the system at the power densities shown.

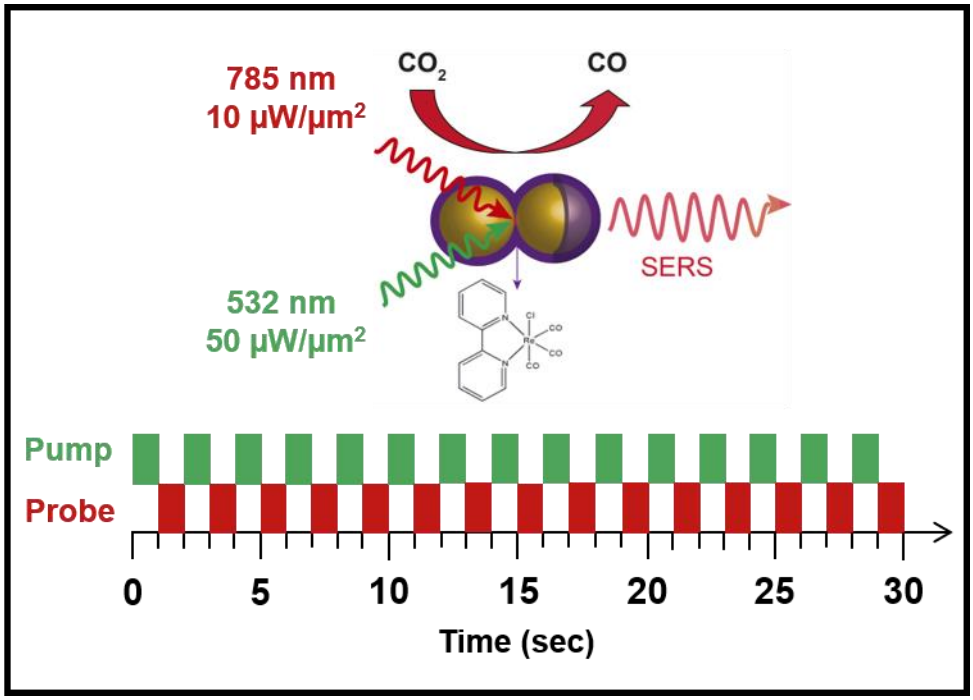

Figure 2.6. Pump-probe scheme for plasmon driven chemistry measurements. Individual nanoparticle oligomers are excited for 1 second by 532 nm light, then probed for 1 second with 785 nm light. This is repeated for approximately 250 iterations in most experiments.

The experiment was done for about ten separate nanoparticle oligomers and sequences of about 250 spectra were collected for each one. From this we found two sequences with behavior indicative of plasmon driven chemistry in the carbonyl stretching region. The first series is

highlighted in Figure 2.7, along with the corresponding TEM image and extinction spectrum from the single nanoparticle oligomer. Due to limitations in the detection range, only part of the vibrational spectrum can be measured at a time, so we decided to focus on the carbonyl stretching region because that is where we expect to see the highest activity upon carbon dioxide reduction and besides the carbonyl bands the region is spectrally quiet. In this first sequence the initial spectrum is shown in blue, exhibiting the common three modes in this region. Sequential spectra are shown in red upon pumping. Here there is a notable peak that grows in around 2065 cm^{-1} and persists for a number of sequential frames then disappears leaving the original spectrum. There are also less intense features that appear and could be attributed to different orientations or transition complexes. But most notably is the mode at 2065 cm^{-1}, which is both intense and narrow hinting that carbon monoxide is being generated in the hotspot. Additionally, literature[80] shows that carbon monoxide adsorbed on Au(111) has a vibrational frequency of 2060 cm^{-1}, which is in strong agreement with this modes 2065 cm^{-1} shift. This is indicative of some sort of process being driven on the plasmonic substrate, but it is difficult without other spectroscopic evidence to say that this indeed plasmon driven reduction or oxidation leading to carbon dioxide reduction. It is quite possible this is caused by carbon monoxide desorption from one of the molecules in the hotspot. A second possible event was seen on a different nanoparticle oligomer. In this sequence we see very similar behavior with a single dominate sharp peak appearing for a handful of seconds then disappearing. However, this time the peak occurs at 2120 cm^{-1}, significantly shifted from the first event. It is still possible and quite likely this second event is also indicative of carbon monoxide being generated in the plasmonic hotspot. The difference in shift can be attributed to the different binding sites available on the highly variable nanoparticle surface. Literature indicates that the

vibrational energy of CO on Au(110) is around 2110 cm^{-1}, while CO on a gold film is 2120 wavenumbers, closely agreeing with the Raman shift observed.[80]

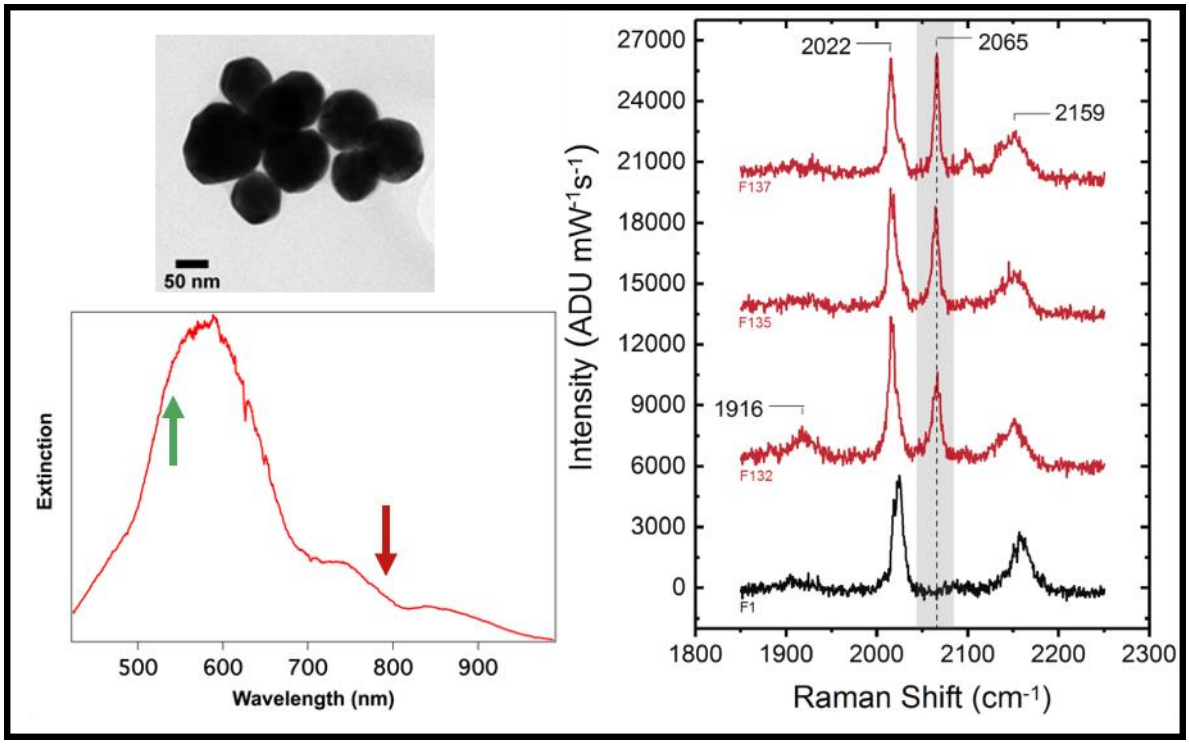

Figure 2.7. On the left is the correlated TEM image and darkfield extinction spectrum of a nanoparticle oligomer. Spectral positions of the pump and probe relative to the scattering response are depicted by the green and red arrows, respectively. On the right are select spectra from a pump probe sequence. The black spectrum is the SERS spectrum before any pumping. The red spectra are measure following one second of exposure to 532 nm. The most evident feature is the appearance of a sharp peak at 2065 cm^{-1}, while the other peaks remain relatively stable.

In order to definitively identify these species and their appearance due to plasmon driven reduction or oxidation, it is necessary to generate these species electrochemically on a plasmonic surface. Following earlier examples in our group, attempts at electrochemical SERS were made.[81] Unfortunately, due to low solubility and activity in water the electrochemical experiment would have to be done in non-aqueous conditions. This posed many difficulties that prohibited progress

of these experiments and ultimately stymied our efforts to definitively identify the species and mechanism in the pump probe SERS measurements.

2.5 Conclusions and Future Directions

We successfully demonstrated that the rhenium bipyridine tricarbonyl chloride complex could be physisorbed to plasmonic gold nanoparticles; however, the measured SERS response more closely resembled the rhenium bipyridine tetracarbonyl cation species. Regardless, later cw pump-probe SERS experiments we able to induce activity on the nanoparticle surface, noted by the appearance of a sharp peak in the carbonyl stretching region. This transient feature maybe attributed to carbon monoxide temporarily adsorbed to gold in the plasmonic hot spot. But ultimately there is no definitive evidence for this reaction being driven in a controllable, reproducible way. For this complimentary electrochemical SERS experiments are necessary in nonaqueous conditions.

While this is not an ideal result, this is still an important system to note. With the current efficiencies for plasmon driven reactions, an application of this system for reduction of carbon dioxide to carbon monoxide is impractical at best. However, if efficiencies in the field of plasmon driven chemistry increase this will be a very important reaction to revisit.

CHAPTER 3

Plasmon Driven Oxidation of Ferrocyanide: A Temperature Study

3.1 Abstract

In effort to further understand the balance of hot electron transfer and local heating within plasmon driven reactions we turn to a model electrochemical system. By studying the plasmon driven oxidation of ferrocyanide to ferricyanide on gold nanoparticles through pump-probe SERS measurements, we are able to controllably drive and observe the reaction and species generated. This alone is of significance due to the well-defined nature of both the reactant and product species with no secondary reactions interfering. From this we conducted a rigorous temperature study using a cryo-optic microscope, in which we measured the kinetics of this reaction under ambient temperatures ranging from 200 to 295 K. At low temperature there is some activity when pumped with 532 nm light attributed to oxidation of ferrocyanide. As the temperature is increased this process becomes slightly more favorable and at temperatures higher than 250 K further conformational rearrangement of the ferrocyanide species is allowed. These observations directly support the idea that plasmon driven reactions are a complex interplay between hot carrier generation and local heating.

3.2 Introduction

Due to the extraordinary sensitivity for surface species enabled by the enhanced local electromagnetic field and the rich chemical information provided by the vibrational fingerprints, SERS is a powerful tool to study plasmon-driven processes. Previously, continuous wave (CW) pump-probe SERS measurements have been used to observe the generation of transient radical anion species at plasmonic hot spots of single nanoparticle oligomers[63, 64] as well as to investigate the mechanism of plasmon-induced hot electron transfer between gold nanoparticles and molecular

species.[82] These studies provide insight towards the nature of plasmon-driven chemistry both on ensemble averaged and few to single molecule levels.

Recently, the plasmon-enhanced photocatalysis of ferricyanide ($[Fe(III)(CN)_6]^{-3}$) to ferrocyanide ($[Fe(II)(CN)_6]^{-4}$) has been reported.[83, 84] Through UV-Vis absorption measurements of a colloidal gold nanoparticle solution, an increased rate of ferricyanide reduction to ferrocyanide under visible light irradiation was observed. This process was further optimized through the addition of hole scavengers in the form of ethanol or PVP.[84] In subsequent studies the authors found that the electron transfer could occur over distances of 1.8 nm using tethered Fe(II)/Fe(III) structures, as long as holes are sufficiently quenched at the nanoparticle surface.[85] It was also stated that two-electron transfer from excited gold nanoparticle to ferricyanide was observed under relatively intense laser irradiation,[85] which makes this reaction a potential model system for future investigations into other plasmonic multi-electron harvesting systems. Additionally, this system is an attractive candidate for a fundamental study since it is a well-studied classical electrochemical redox pair that has been investigated using electrochemical SERS techniques.[86]

Using an all optical measurement technique like cw pump-probe SERS to drive and monitor the oxidation of $[Fe(II)(CN)_6]^{-4}$ allows for additional experimental control of the sample environment. One of the major questions surrounding plasmon driven chemistry is what role local heating plays in these reactions. While one group[87-91] of experiments continually utilizes the local heating properties of plasmonic nanoparticles to develop applications for these materials, the other group[57, 59, 63, 92] of experimentalists routinely finds reactions and events that are more indicative of hot carrier transfer. With these experiments we conduct our pump-probe SERS technique using a

cryo-optic microscope to vary the ambient temperature of our sample from 200 K to 297 K. By extensively measuring the reaction kinetics under room temperature conditions, we established conditions for driving and observing the oxidation of $[Fe(II)(CN)_6]^{-4}$ to $[Fe(III)(CN)_6]^{-3}$ on the surface of aggregated gold nanoparticles. The SER spectra taken in the nitrile stretching region indicate a two-part mechanism. The Fe(II) surface species is first oxidized to Fe(III), then the bond between the nitrile group of the Fe(III) species and the gold surface is broken, resulting in a significant and observable peak shift. This mechanism is further elucidated through the temperature dependent experiments. Under the reduced environmental temperatures the oxidation of Fe(II) to Fe(III) is observed. Upon raising temperatures, the oxidation becomes increasingly more favorable, yet the reconfiguration of the oxidized species is still not favorable until temperatures above 250 K are reached. This highlights the fact that the reconfiguration step, not visualized in classic electrochemical measurements, is thermally limited. This fundamental reaction characterized with extensive detail represents a major step forward in elucidating the true nature of plasmon driven reactions and provides a strong basis for further investigation.

3.3 Experimental Details

Preparation of aggregated gold nanoparticle substrate. Gold nanosphere oligomers consist of aggregated 60 nm diameter gold spherical cores functionalized with potassium ferricyanide ($K_3[Fe(CN)_6]$). In a typical sample preparation, aggregation of gold sphere cores was induced by adding 20 μL of 3 mM aqueous solution of $K_3[Fe(CN)_6]$ (Sigma-Aldrich, ≥99 %) into 1mL of colloidal 60 nm diameter gold spherical cores (0.25 mg Au/mL, STA Technologies Inc.). The gold colloid was allowed to aggerate for 50 min under room temperature before a 10 μL aliquot

of aggregated gold colloid was dropcasted onto a microscope glass coverslip (VWR International, No.2) and allowed to dry naturally, forming layers of densely immobilized nanosphere oligomers at high concentration on the glass substrate.

Glass coverslip preparation. Microscope glass coverslips (VWR International, No.1, 25 mm diameter) underwent piranha treatment (3:1 H_2SO_4:30%H_2O_2) followed by thorough rinsing with Milli-Q water (18.2 MΩ/cm). Coverslips were then immersed in a base treatment, (5:1:1 H_2O:NH_4OH:30%H_2O_2), sonicated for sixty minutes, and again thoroughly rinsed with Milli-Q water. Sample grids were positioned on top of N_2 dried coverslips and mounted on a sample stage above the microscope objective.

Continuous wave pum-probe SERS measurements. CW pump-probe SERS measurement shown in Figure. 2 was performed on an epi-illumination microscope setup (Nikon Ti−U) using a 40× objective (Nikon, NA = 0.60). During measurements, samples were irradiated with spatially overlapped 785 nm CW probe laser beam (Renishaw Inc.) and 532 nm CW pump laser beam (Spectra-Physics). The scattered radiation was then sent into an Acton spectrograph (Princeton Instruments) equipped with a PIXIS 400BR CCD Camera (Princeton Instruments).

Temperature controlled cw pump-probe SERS measurements. samples were placed on an agile temperature stage module inside the optical sample chamber of a cryostat (Cryostation S50, Montana Instruments) equipped with a cryo-optic 100× objective (Zeiss, NA=0.9). A 785 nm cw laser (Renishaw Inc.) and a 532 nm cw laser (M Squared) were overlapped spatially in the focal plane. The scattered light was then collected by the same objective, Rayleigh scattering is filtered out using a 785 nm long pass (Thorlabs), and the remained sent into a SpectraPro HRS-500

Spectrograph (Princeton Instruments) equipped with a PIXIS 400BR CCD Camera (Princeton Instruments). A mechanic shutter (Picard Industries) was used to precisely control the pumping time.

Visible−NIR nanoparticle extinction characterization. The extinction spectrum for the ferri-/ferrocyanide @ AuNP was obtained in solution phase using a spectrophotometer in double beam mode (Cary 5000, Agilent Technologies). The sample was scanned over a wavelength range of 400-1000 nm.

3.4 Results and Discussion

For CW pump-probe SERS measurements, gold nanosphere oligomers are formed by aggregating a colloidal solution of 60 nm gold nanospheres with a small amount of potassium ferricyanide ($K_3[Fe(III)(CN)_6]$). After allowing the solution to aggregate for 50 min, a 10 μL aliquot of aggregated gold colloids is drop cast onto a glass coverslip and allowed to dry, forming layers of densely packed nanosphere oligomers. Samples prepared with this method are then used for cw pump-probe SERS experiments in an epi-illumination geometry. Based on the bulk extinction measurement of the aggregated gold colloids in solution (Figure 3.1), 532 nm light resonant with the monomer plasmon mode is chosen as the optical pump, while 785 nm light that overlaps with the broad multicore plasmon resonance is chosen as the probe to maximize the Raman enhancement factor.[13] SER spectra of the sample measured using 785 nm clearly display the characteristic nitrile stretching bands in the high wavenumber (2000-2500 cm^{-1}) region indicating the presence of the ferri-/ferrocyanide species at the plasmonic hot spots created by the aggregation of the gold nanospheres.

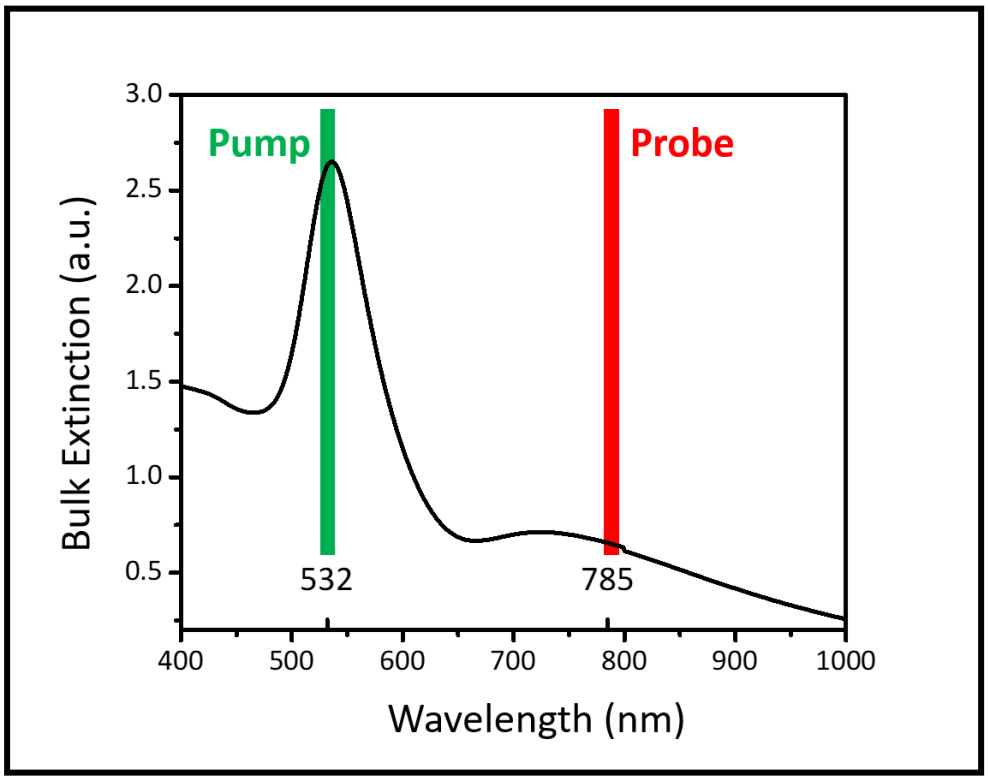

Figure 3.1. Visible-NIR extinction spectrum of the ferri-/ferrocyanide coated gold nanoparticle aggregates in solution phase.

A representative set of pump-probe SER spectra is presented in Figure 2. The sample is initially irradiated by the 785 nm probe beam (4.1 $\mu W/\mu m^2$=4.1*10^6 W/m^2=4100 kW/m^2=410 W/cm^2) and 5 consecutive SER spectra are collected with an acquisition time of 20 seconds each to check for stability of the surface species during exposure to the pump beam. At this point, two major bands are present at 2115 cm^{-1} and 2150 cm^{-1} with a relatively low intensity band centered at 2190 cm^{-1} with only small fluctuations in their intensity. Then the sample is exposed to the 532 nm pump (105 $\mu W/\mu m^2$) while continuing acquisition of the SER spectra with the 785 nm probe for another 720 seconds. Upon exposure to the pump an immediate and significant decrease in the

intensity at 2115 cm^{-1} and 2150 cm^{-1} is observed. The intensity of 2190 cm^{-1} band increases within the first 2 frames after pumping and then gradually drops below its initial intensity, with the emergence and increase of a distinctive new band centered at 2134 cm^{-1}. Afterwards, the pump beam is shuttered and continued acquisition of SER spectra with the 785 nm probe reveals that the spectral signatures remain unchanged after pump is turned off. The rise and subsequent depletion of 2190 cm^{-1} band suggests it is an intermediate species, while the accompanied appearance and continued growth of 2134 cm^{-1} band indicate its role as the signature for the final product within our experimental timescale. This is highlighted by the time trace of the peak areas shown in Figure 2c.

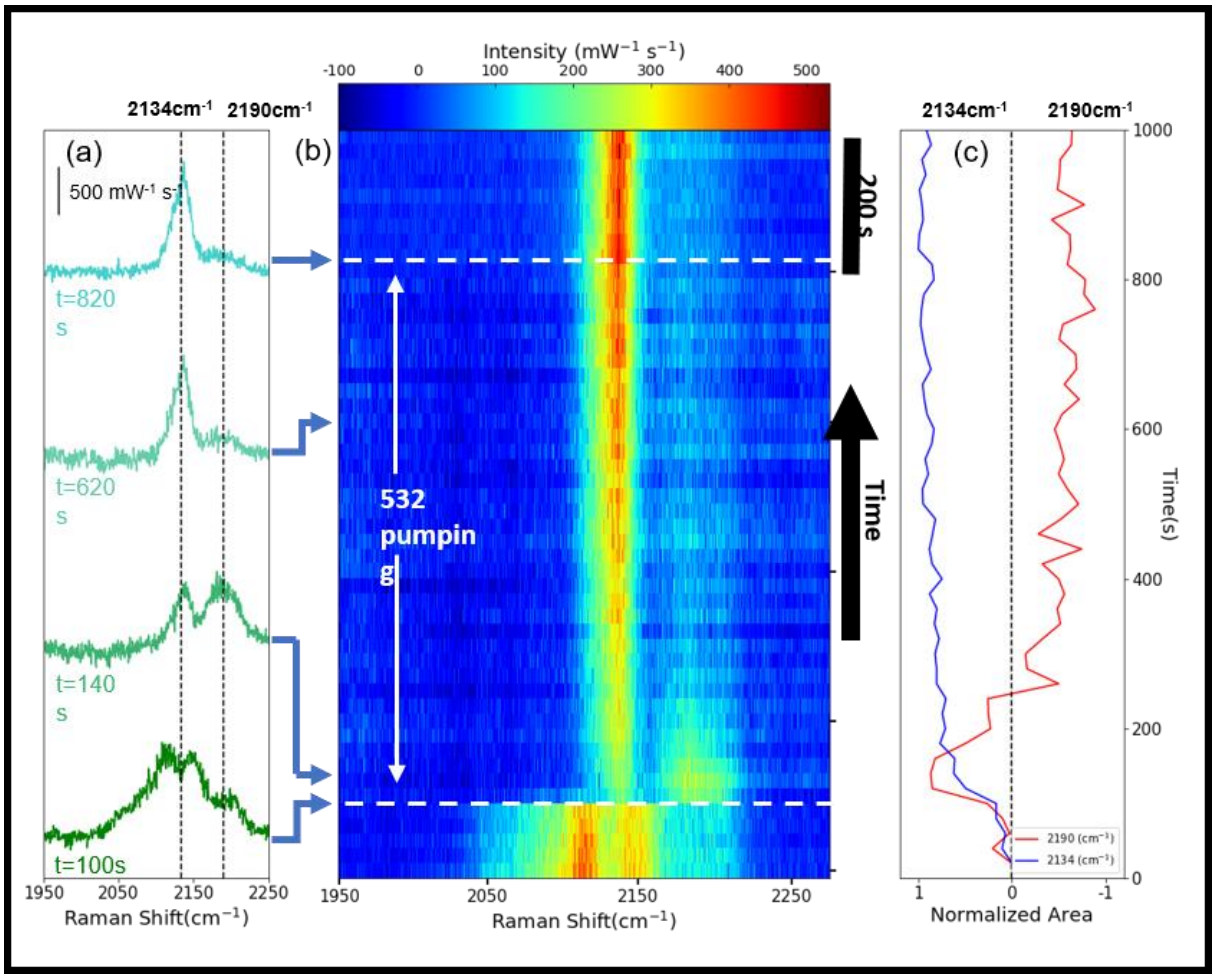

Figure 3.2. Representative plasmon-induced reaction of the ferri-/ferrocyanide @ AuNP system. (a) SER spectra at t=100 s (before pumping), t=140 s, t=620 s (during pumping) and t=820 s (after pumping). (b) Waterfall plot shows time-dependent SERS data recorded by 785 nm probe beam. And the ensuing spectral changes after 532 nm optical pumping. (c) Time profile of the relative peak areas centered at 2190 cm-1 band and 2134 cm-1 band relative to the initial peak area.

In order to identify these species apart from their being reactant, intermediate, and products, we use non-surface-enhanced Raman spectra of saturated potassium ferricyanide and potassium ferrocyanide in water as references. The spectra, taken using 785 nm excitation, are shown in Figure 3.3. The three peaks in the SERS spectrum prior to pumping with 532 nm light, are in good agreement with the two nitrile modes of Fe(II) and the major nitrile mode of Fe(III) in

solution-phase normal Raman spectra, albeit with a consistent blue-shift of around 55 cm^{-1} for all nitrile bands. The observed blue-shift in SERS compared to normal Raman spectra strongly suggests adsorption of Fe species to the surface of gold nanoparticles and the formation of Fe-CN-Au bridging bond during the aggregation. The blue-shifted stretching mode of the bridging nitrile group has commonly been reported, both within various organometallic complexes[93] and under electrochemical SERS context[86, 94] mainly due to the bonding of nitrile group through the nitrogen lone pair to the second metal center, which resides mostly in an antibonding orbital, thus increasing the strength of the carbon-nitrogen bond. From this we conclude our initial speciation of the gold nanoparticle surface consists of both Fe(II) and Fe(III) surface bound species, with a majority being Fe(II) assuming similar Raman cross sections. This indicates that upon association with the gold surface, Fe(III) in solution are reduced to Fe(II), and these species which have a higher affinity to the gold surface become bound through the nitrogen of a carbonyl group. Again, we see this spontaneous reduction upon association with the gold surface common in the plasmon driven chemistry literature,[41, 78] which seems to be indicating that their energy levels are close and a plasmon driven reaction may be accessible.

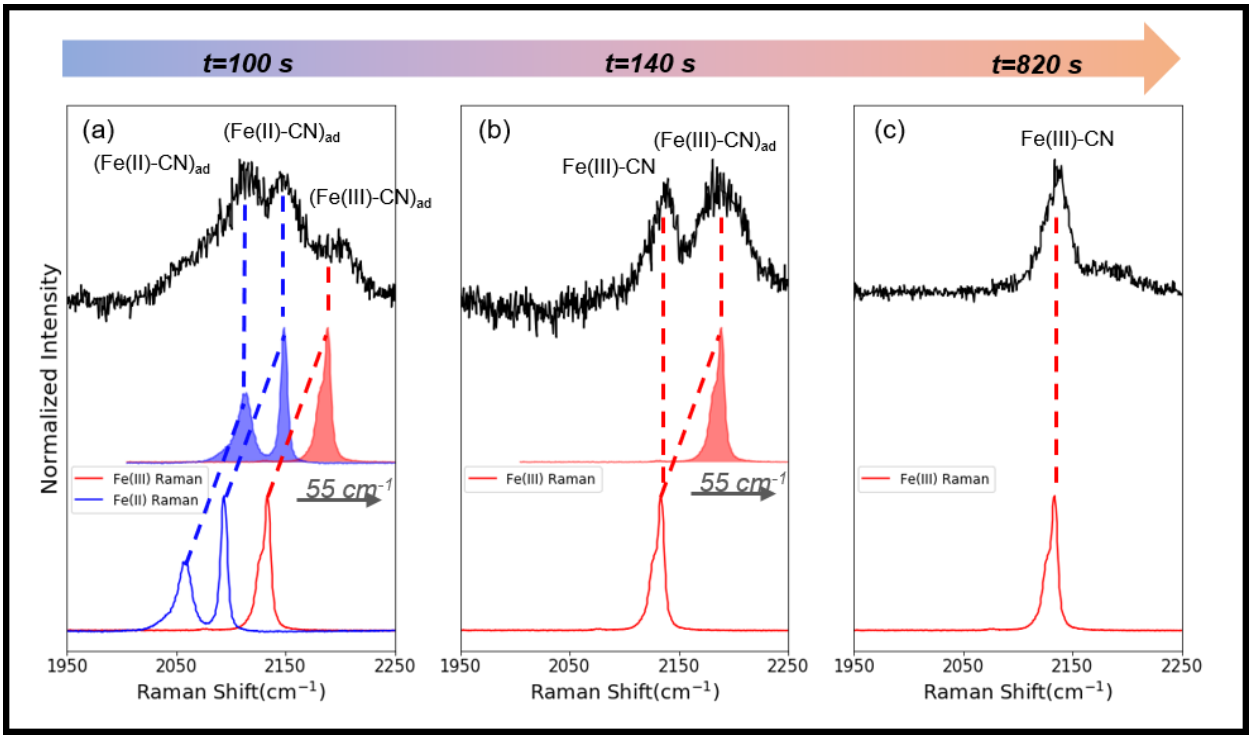

Figure 3.3. Comparison between solution-phase normal Raman spectra and selected cw pump-probe SER spectra before pumping (a), during pumping (b), and after pumping (c). Bottom: normal Raman spectra of saturated potassium ferricyanide (III) solution (red) and potassium ferrocyanide (II) solution (blue) using 785 nm excitation. Middle: blue-shifting the bottom spectra for 55 cm-1 to guide the comparison. Top: CW pump-probe SER spectra in ferri-/ferrocyanide @ AuNP system at various times, with proposed peak assignments.

When the plasmonic substrate is excited by 532 nm irradiation, we see an oxidation of the surface bound Fe(II) species to Fe(III) which is still bound to the gold surface as evidenced by its 55 cm^{-1} shift relative to the solution phase Raman. Upon continued illumination with 532 nm at power densities of ~100 $\mu W/\mu m^2$, a new mode dominates the spectrum at 2134 cm^{-1}. This is in agreement with the solution phase Fe(III) species, indicating the bond between the gold surface and carbonyl group has been broken or at least significantly weaken. These assignments are supported by previous electrochemical studies[86] but have not been previously studied with the level of detail SERS measurements afford. This reaction pathway provides an understanding of

the observed plasmon-induced processes. First a charge transfer step between the gold nanoparticles and surface Fe(II) species, followed by a bond-breaking step between the oxidized surface Fe(III) species and gold.

The observed two-step plasmon-driven process exhibits environmental temperature dependence, as is revealed by cw pump-probe SERS measurements carried out under various temperatures. For these measurements, the sample is placed on a temperature controlled stage within the optical chamber of a cryo-optic microscope for easy environmental temperature control ranging from 10 K to 295 K. A common sequence for data acquisition consisted of (1) collecting a single frame SER spectrum at 785 nm for 20 s as the initial spectrum, (2) exposing the sample to the 532 nm laser for 40 seconds while the probe is shuttered, then (3) collecting a second SER spectrum at 785 nm for 20 s as the final spectrum. Difference spectra are made by subtracting the corresponding initial spectra from the final spectra and then normalized to the intensity of the initial spectrum to account for differences in enhancement factors at different sample sites. Difference spectra for each excitation power and temperature are taken at least 5 spots and averaged to account for sample heterogeneity. To obtain data as a function of pumping time, this experimental routine was simply repeated with new spots and a different duration of exposure to the 532 nm laser.

The experimental scheme described above was performed for select temperatures ranging from 200 K to 295 K with an incident pump power of 350 μW (Figure 3.4(a)). At 200 K, oxidation of the surface Fe(II) species leads to depletion in intensity at 2115 cm^{-1} with a corresponding increase in intensity at around 2190 cm^{-1} indicating formation of the surface bound oxidized Fe(III)

species. At this temperature, a small peak centered at 2134 cm^{-1} is just noticeable, indicating a most of the generated Fe(III) species remain bound to the gold surface. As we increase the temperature, we observe similar behavior at both 219 K and 238 K with slightly increasing intensity in the difference spectra, indicating the oxidation is becoming more favorable. When exposed to 350 μW of pump power at 257 K, the peak centered at 2134 cm^{-1} gains considerable intensity, which increases dramatically upon increasing the temperature to 276 K and 295 K. This indicates that at these temperatures a majority of the oxidized Fe(III) species are not directly bound through the nitrile group, but rather resemble free Fe(III) in solution. This is a significant result because the data indicates this is a consistent, repeatable reaction that relies on plasmon excitation and has a clear dependence on the environmental temperature. In effort to resolve the kinetics of this reaction, SERS difference spectra were measure with variable pumping times from XXX to XXX at temperatures of 200 K, 257 K, and 295 K. The normalized area for the peaks centered at 2190 cm^{-1} and 2134 cm^{-1} are then calculated and then plotted as a function of pumping time (Figure 3.4 (b,c)). While not quantitative, these kinetic traces confirm the patterns we saw previously in that this reaction has a strong environmental temperature dependence. Looking at panel (b) in Figure 3.4 it is clear that the initial oxidation step takes much longer (~10X) to complete at 200 K versus at 257 K and 295 K. The subsequent bond breaking step, visualized in Figure 3.4(c), shows a significant temperature dependence as well, with the reaction completing in about 80 seconds of pump exposure at 295 K and 160 seconds at 257 K. At 200 K, after 640 seconds of pump exposure measurements were concluded, however, observed peak intensity at 2134 cm^{-1} never reached levels seen in the experiments at 257 K and 295 K.

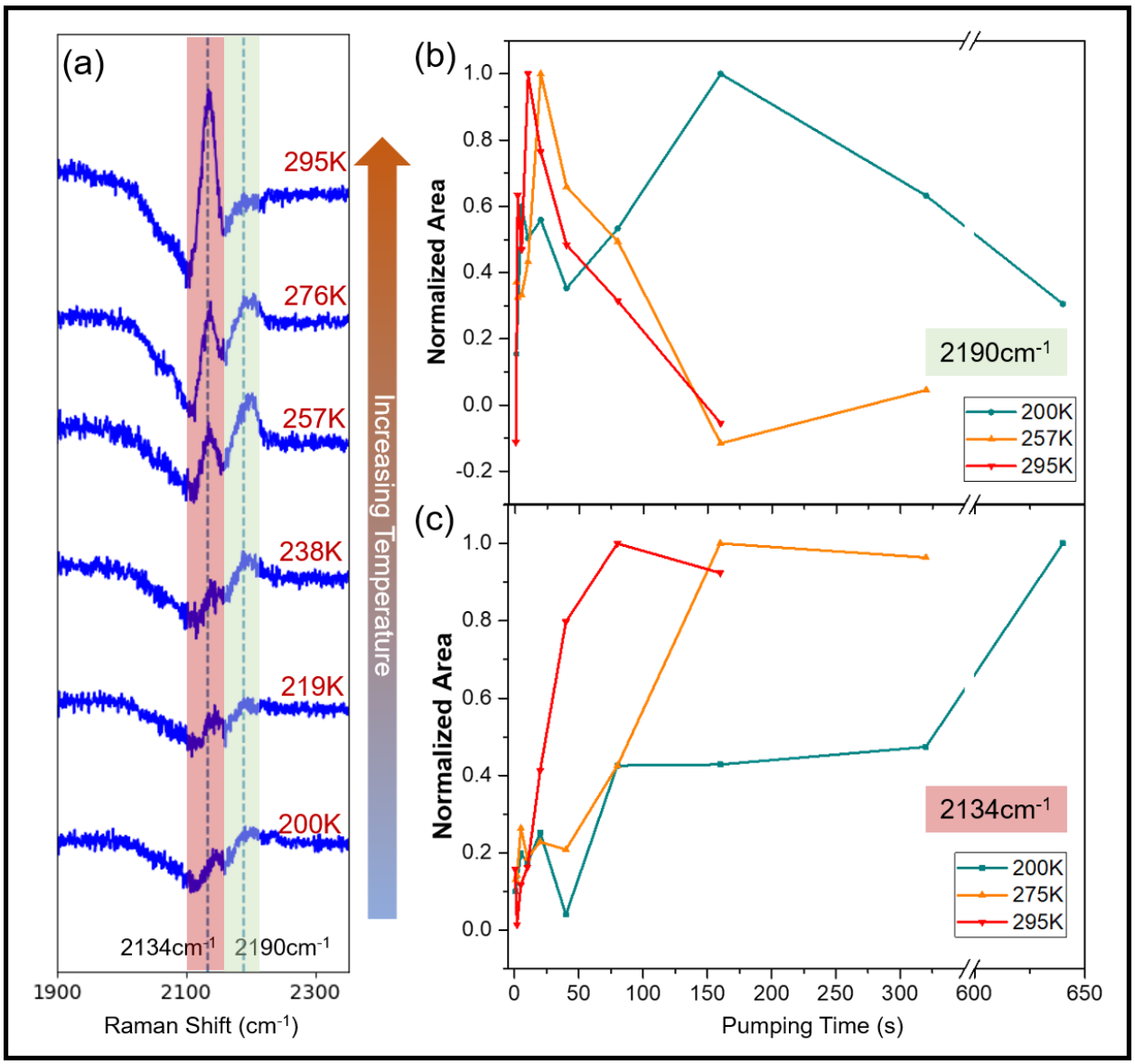

Figure 3.4. a) SERS difference spectra taken at various temperatures ranging from 200 K to 295 K after exposure to 350 μW of 532 nm light for a duration of 40 seconds. Oxidation of Fe(II) to Fe(III) is indicated by depletion of the 2115 cm^{-1} peak and increase of the peak at 2190 cm^{-1}. Bond breaking between the nitrile group of the oxidized species and gold is indicated by the appearance of the peak at 2134 cm^{-1}. b) Normalized areas of the 2190 cm^{-1} and the 2134 cm^{-1} peaks as a function of pumping time with XXX μW of 532 nm light for 3 temperatures.

The results this far show that this reaction exhibits a strong temperature dependence and that it can be driven by exposure to 532 nm light. To investigate the role of local heating, measurements above ambient temperature were conducted. For this the temperature of the sample was raised using a heating stage while monitoring the SERS response at 785 nm. For the first trial, a freshly prepared sample was heated to 356 K and allowed to equilibrate for around 1000 seconds. No substantial spectral variances were observed by 785 nm Raman probe except for a slow, gradual decrease in the overall intensity due to thermal expansion of the apparatus, which suggests that the first step cannot be purely thermal driven. In order to investigate how the second step is related to environmental heating, the intermediate was first generated by irradiating the sample with 532 nm pump beam for 20 s under room temperature, then the sample was heated to 356 K to see if the bond breaking step could be driven through heating. As can be seen in Figure 3.5, no increase in the 2134 cm^{-1} peak was observed over the course of 300 seconds. After which the sample was exposed to the 532 nm pump which immediately induced a rise in the 2190 cm^{-1} followed by its depletion and accompanied by the continued increase of the 2134 cm^{-1} peak. This result indicates that the observed reaction is not a purely thermal one and does in fact rely on 532 nm excitation.

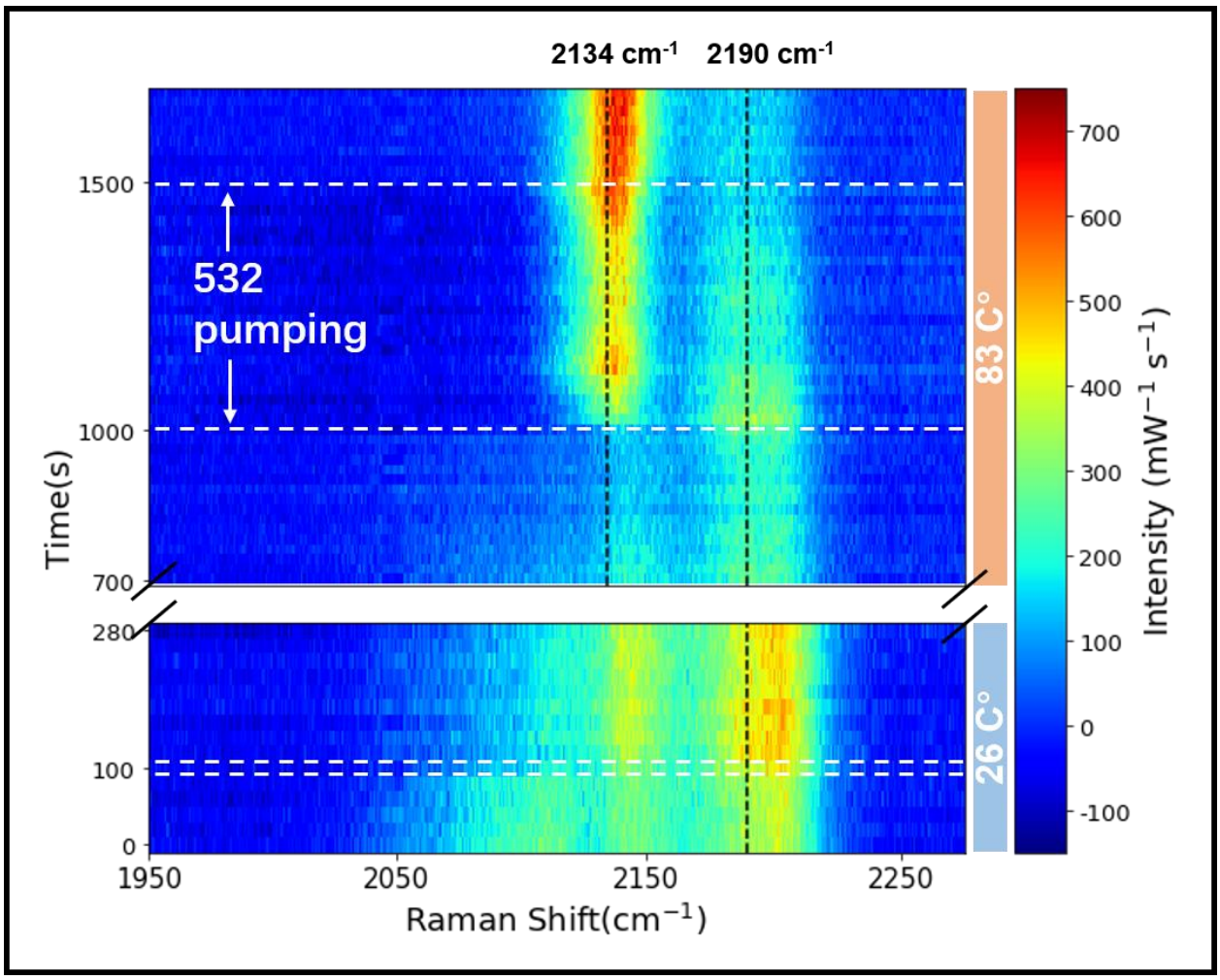

Figure 3.5. The water fall plot shows time dependent SERS spectra. At time 0 the sample is at 299 K. At t=100 the sample is exposed to the 523 nm pump for 20 seconds, driving some Fe(II) oxidation to Fe(III). The sample is then heated to 356 K and allowed to equilibrate over the course of 420 seconds. Observation for the next 300 seconds revealed no forward progress in the reaction. The sample was again exposed to the 532 nm pump resulting in further oxidation followed by the bond breaking step.

3.5 Conclusions

In summary, we have used SERS to directly observe the two step plasmon-driven reaction between ferricyanide and ferrocyanide ions within SERS active hot spot formed by gold nanosphere oligomers. The plasmon-induced oxidation of adsorbed surface Fe(II) into Fe(III) is

followed by a bond-breaking step between gold surface and Fe(III) species. The vibrational signatures of reactant, intermediate and final product are rigorously assigned, allowing the plasmon-driven processes to be fully characterized. By acquiring the reaction kinetic time traces at different environmental temperatures, qualitative observations of this temperature dependence can be made. Furthermore, experiments above ambient temperature confirm that this reaction is not due purely to local heating.

CHAPTER 4

Plasmon Driven Chemistry on Ultrafast Timescales: Trial and Error

4.1 Introduction

Plasmon driven chemistry offers a novel route of chemical transformation and has significant potential impacts on applications such as energy conversion and photocatalysis. The processes of plasmon excitation and relaxation, along with associated cascade of chemical events, occur through multiple time scales. Elucidating the full extent of plasmonically driven chemical events is key to deepening our fundamental understanding, enabling novel applications.

The majority of plasmon driven chemistry literature looks at these reactions and their products on macroscopic timescales,[52, 63, 83] which was largely covered in the previous chapters. In these experiments a plasmonic substrate is excited with continuous wave irradiation with equal or higher energy than the plasmon resonance. It is postulated that this results in a non-equilibrium electron distribution at the surface of the plasmonic substrate from which hot carriers can transfer to nearby molecular species causing a reaction by reduction or oxidation with one or more hot electrons or holes, respectively.[35] One specific example of this is the recent work by Sprague-Klein et. al.[63] In this measurement a 532 nm cw laser source is used to excite on the high energy side of the 90 nm gold nanoparticle LSPR for sufficient coupling and excitation energy. This results in an excitation of electrons from the d-band to sp-bands.[20] The local molecular population is then monitored using SERS from a 785 nm cw probe. The results show that in the hot spot of the nanosphere oligomer, electrons are being transferred from the gold surface to BPY resulting in the vibrational signature of the BPY radical anion appearing in the SERS spectra (summarized in Figure 4.1). Additionally, subsequent measurements revealed that this process can be generalized to the structurally similar molecule, BPE, indicating this is most like a result of indirect charge

transfer, as opposed to direct charge transfer which relies on a hybrid resonance being directly excited.[20] These experiments demonstrate the types of reactions accessible with this technique but does little to elucidate the timescales and thus the driving force of the reaction.

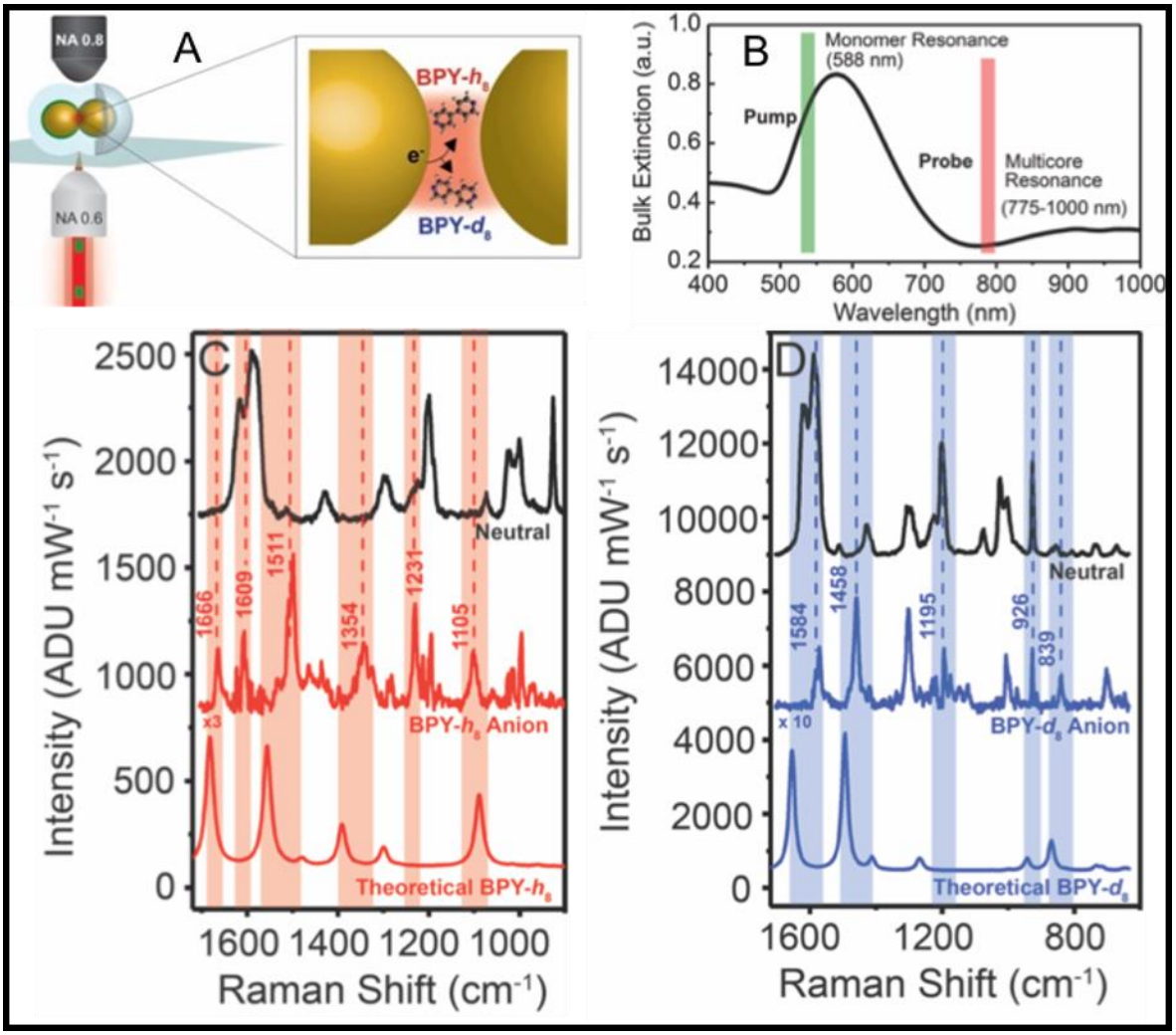

Figure 4.1. A) Single particle pump-probe scheme for generation and detection of radical anion species due to plasmon-driven electron transfer in 4,4'-BPY-h_8/d_8 gold nanosphere oligomers. B) Visible-NIR extinction spectrum of BPY-h_8/d_8 gold nanosphere oligomers in solution phase. Monomer resonance is observed at 588 nm while the multicore resonance is the broad feature in the near-infrared. C) Neutral spectrum for a BPY-h_8 + BPY-d_8 nanosphere assembly (black). Middle spectrum depicts BPY-h_8 anion modes that appear (red). Bottom spectrum shows open-shell DFT calculation for radical BPY-h_8 anion. D) Top spectrum consists of neutral molecules only (black), mid-spectrum is BPY-d_8 anion modes, and bottom spectrum is DFT calculated BPY-d_8 anion modes. Figure adapted from Ref[63] with permission from Dr. Emily Sprague-Klein. Copyright 2017 American Chemical Society.

In order to probe these events on the timescale on which they occur, a large amount of experimental effort was put in to translating these experiments to ultrafast Raman techniques.

Herein I will focus on the most direct effort which implemented ps-pump-probe spontaneous SERS. This technique has been well established in the field and has been shown to have similar signal to noise ratios as cw SERS and sufficient spectral resolution given a narrow bandwidth (<10 cm-1) Raman probe pulse.[31] Also, the experimental design allows for a direct analogue to the previous cw experiments with one additional parameter, time delay between the actinic and probe pulses. In this experiment it is not expected to see the rise time of these processes because the electron distributions that drive this chemistry is created instantaneously upon exposure to the pump pulse, but ideally the decay times would be captured on this timescale, allowing us to rule out long-term local heating as a driving force.

4.2 Experimental Details

Picosecond pump-probe SERS measurements. An 80 MHz Ti:sapphire oscillator (Tsunami, Spectra-Physics) generates a 1.5 ps pulse centered at 775 nm (2 W). This is split by a 90:10 by a beamsplitter. The larger portion (1.8 W) pumps an optical parametric oscillator (OPO) tuned to generate a 1.5 ps pulse centered at 532 nm (300 mW). This is used as the pump pulse and is direct to a retroreflector before it is coupled into the inverted microscope (Ti-U, Nikon). The remaining 200 mW of 775 nm light is used as the Raman probe. Its pathlength is matched to the pump pulse, then it is coupled into the microscope and overlapped spatial with the pump pulse. Sum frequency generation (SFG) in a 5 mm thick beta barium borate (BBO) crystal is performed at the sample plane of the inverted microscope using an long working distance 50x objective (Nikon) to find temporal overlap between the two pulse trains.

Glass coverslip preparation. Microscope glass coverslips (VWR International, No.1, 25 mm diameter) underwent piranha treatment (3:1 H_2SO_4:30%H_2O_2) followed by thorough rinsing with Milli-Q water (18.2 MΩ/cm). Coverslips were then immersed in a base treatment, (5:1:1 H_2O:NH_4OH:30%H_2O_2), sonicated for sixty minutes, and again thoroughly rinsed with Milli-Q water. Sample grids were positioned on top of N2 dried coverslips and mounted on a sample stage above the microscope objective.

Single nanoparticle oligomer sample preparation. Silica coated gold nanosphere oligomers functionalized with bipyridine or bipyridyl ethylene were diluted 1:10^4 with Milli-Q water (18.2 MΩ/cm) and were drop-casted onto 3 nm thick carbon/Formvar TEM grids (Ted Pella, Inc.).

4.3 Results and Discussion

In the time-resolved version of the experiment we pump the BPY coated nanoparticle oligomers in an inverted microscope with a ~1.5 ps 532 nm pump pulse and probe the system with a ~1.5 ps 775 nm probe pulse at a given time delay. Observing the frequency of electron transfer events as a function of probe pulse delay will allow us to determine the timescales on which these events occur and possibly observe any intermediate species generated. For a single nanoparticle aggregate, a sequence of spectra is taken with a 1 second acquisition time for 100 sequential spectra. This is analogous to our continuous wave experiments, the idea being that these events often blink in with large Raman activity for short amounts of time. By dividing a longer time acquisition into individual frames, we can count the number of events observed to estimate the activity at a given time delay. In the continuous wave experiments[63, 64] this acquisition scheme

shows numerous events occurring on a large amount of the aggregates measured (Figure 4.1). While the events are common the type of event can vary from isomerization to reduction of the molecule.[64] With the picosecond pulsed experiment this is largely not the case. Performing the analogous experiment with power densities, we see a steady, uniform degradation of the BPY spectroscopic signature with no signs of plasmon driven chemical products. The obvious explanation for this is that the incident power density is too high and the resulting local fields are degrading the molecules of interest. Upon reducing the incident pump field power about an order of magnitude, a regime can be reached where the degradation is negligible; however, almost no events that could be attributed to plasmon driven chemistry were observed. After approximately 100 individual nanoparticle aggregates probed through this technique, a total of one event was observed. This can be seen in the spectra shown in Figure 4.2, where over the course of 3 sequential spectra you see the appearance of a peak around 1510 cm^{-1} which our previous works attribute to a vibrational mode of the BPY radical anion. This observed event provided a short burst of motivation towards this work, but unfortunately after many more successive attempts, including ones with BPE, more events were not observed. While this result is not necessarily groundbreaking, it is quite important to take note of due to the amount of effort and interest towards this direction within the field of plasmon driven chemistry.[65, 68, 78, 95]

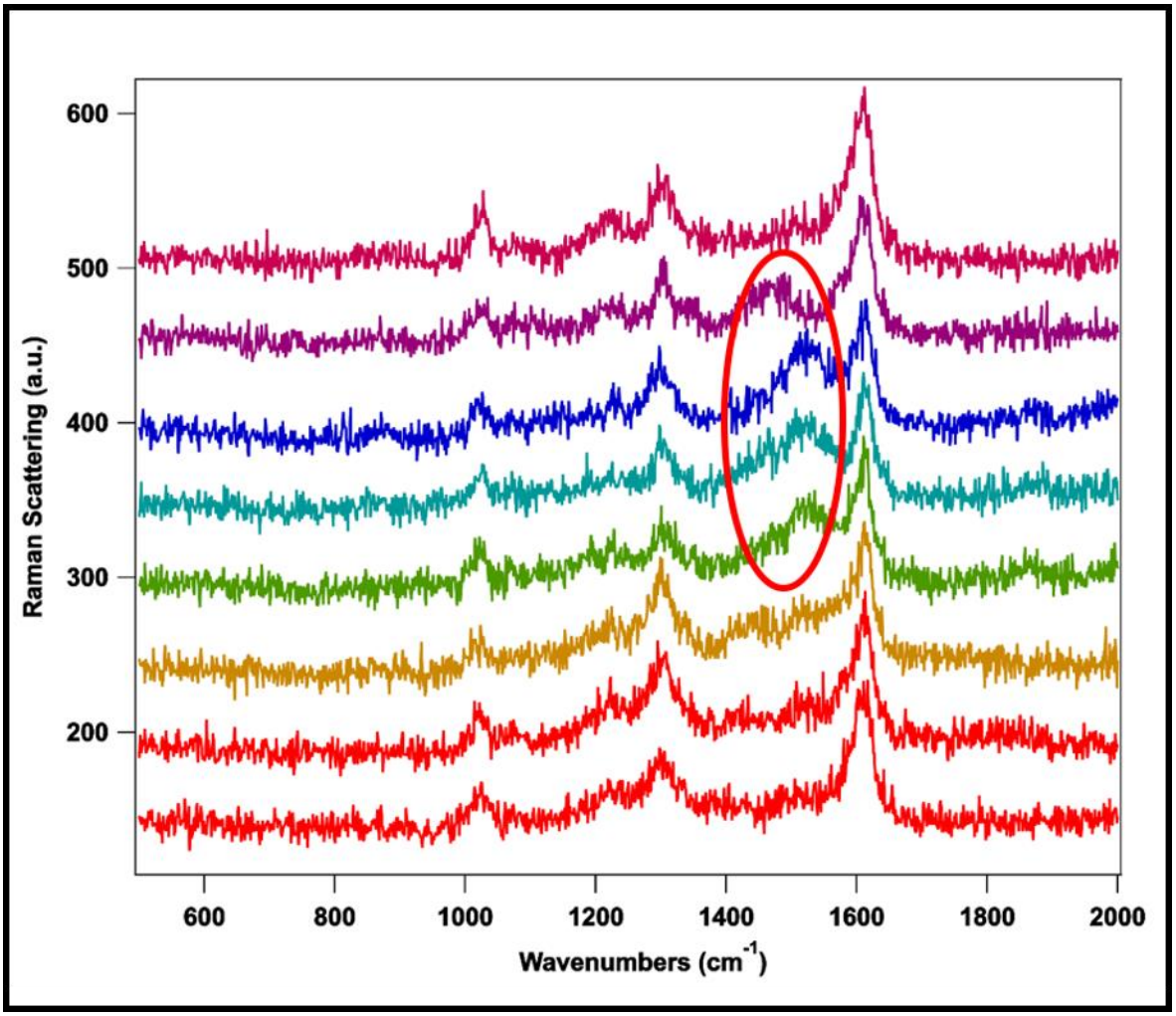

Figure 4.2. Sequential SERS spectra from a ps-pump-probe SERS measurement. At the bottom is the initial BPY spectrum before pumping with 532 nm. In the sequential 1 second acquisitions, upon exposure to the 532 nm pump, a feature centered at 1510 cm^{-1} appears for a total of 3 seconds before shifting slightly and returning to the baseline.

4.4 Possible Conclusions and Future Directions

From this work nothing is definitive but two reasonable conclusions can be drawn. The first of which would be that the chemistry we are attributing to a plasmon driven reaction is a result of local heating caused by the extreme localization of the electric field in plasmonic hotspots. This

theory has been supported in some respects by the literature. Often referred to as plasmon assisted local heating, plasmonic substrates have been used in many studies to do things from boiling water[90, 91] to locally heating and killing tumor cells.[87] These studies often rely on simple plasmonic structures such as spherical or rod-shaped gold nanoparticles.[87, 90] The interesting thing here is that the degree of localization in monomer particles is vastly lower than nanoparticle oligomers due to the geometries of the resonance. This hints that it is possible for nanoparticle aggregates to provide higher rates of local heat within the nanoparticle junctions, which is significant because that is where a majority of the surface-enhanced spectroscopic signal originates. From this it is reasonable that the molecules in these experiments are experiencing very high temperatures that could potentially degrade them or initiate thermally limited reactions. However, this local heating theory has been explored in a ps-pump-probe Raman experimentd by the Frontiera Group in which they calculate an effective temperature at the hot spot using the Stokes/anti-Stokes ratio of the vibrational modes of a local reporter molecule.[68] The results indicated only modest increase of the local effective temperature, with an effective heating of approximately 50 K for most vibrational modes and plasmonic structures which would not be sufficient to result in things like steam generation.

These contradictions are abundant in the plasmon driven chemistry literature, which leads to the second theory, that pulsed and continuous wave irradiation is vastly different from the perspective of the plasmon. While it may be apparent that pulsed and cw light are very different, it is not immediately clear why they would be able to access different reaction regimes on the same plasmonic substrate. However, there has yet to be any studies that directly aim to bridge this gap. A possibility is that by driving a plasmon resonance for longer durations of time (seconds vs

picoseconds) leads to a different division in the incoming energy between heating and electron excitation. Presumably in the cw case the local heating will dominate due to the lack of a null phase, while the high energies of picosecond pulses could lead to more nonlinear effects producing hotter carriers. To fully address this question a comprehensive study would measure the Stoke/anti-Stokes ratios to approximate the local heating as a function of actinic pulse duration from femtosecond to nanosecond to continuous wave. You would also need to pair this with an experiment to determine the product yield as a function of actinic pulse duration. For this using a simple well characterized plasmon driven reaction such as our recently established ferricyanide oxidation reaction would be beneficial. The molecular signatures would be monitored by a continuous wave probe to avoid unnecessary perturbation and experimental complexity and allowing for a direct kinetic trace of the reaction under the given pulse length.

With this I will note the above discussion is mostly conjecture; however, these ideas are fundamental to the field of plasmon driven chemistry and its future. I am confident that this field will be avidly pursued and the answers eventually uncovered.

CHAPTER 5

Time Resolved Surface-Enhanced Femtosecond Stimulated Raman

5.1 Abstract

Time-resolved coherent Raman scattering (tr-CRS) techniques are ideally suited for observing molecular dynamics on ultrafast time scales. Specifically, the development of femtosecond stimulated Raman scattering (FSRS) experiments has allowed for vibrational characterization of molecules with a spectral resolution of 10 cm^{-1}, while providing an instrument response times as low as 50 femtoseconds.[96] Recently the Van Duyne group has demonstrated surface enhancement of the FSRS process is possible.[16] Further works established the origin of dispersive line shapes in the vibrational spectrum,[97] in addition to optimizing power density and sample concentrations for optimal signal to noise ratios.[98] Much like the previous attempts to observe plasmon driven chemistry on ultrafast time scales, SE-FSRS was applied to this problem with no avail. In order to demonstrate time resolved experiments are possible with the SE-FSRS technique, the dynamic response of the nanoparticle substrate was used to modulate the SE-FSRS signal. For this, a colloidal solution of gold nanosphere oligomers functionalized with bipyridyl ethylene and encapsulated in a silica shell is exposed to a 532 nm actinic pulse (150 fs) to pump the monomer plasmon resonance of the substrate, then at a given time delay (0 – 100 ps) the local environment is probed with the FSRS pulse pair consisting of a 800 nm Raman pump (1.5 ps) and a broadband Raman probe (100 fs). The actinic pulse induces a non-equilibrium electron distribution that decays on the femtosecond-picosecond timescale resulting in population of the low-lying phonon modes of the nanoparticle oligomers. The result is in an initial broadening of the localized surface plasmon, which then modulates due to the expansion and contraction induced by the phonon modes of the nanoparticles. From the perspective of the molecular reporter, the environment is rapidly transitioning from one with a highly delocalized electron distribution to

one with a modulating nanogap, effectively changing the coupling of the molecule with the far-field radiation. Both the rapidly changing electronic environment as well as the interaction of molecules within this environment can be observed through tr-SE-FSRS, providing a first step toward fully understanding plasmon-molecule interactions on ultrafast timescales.

5.2 Introduction

When a metal system is excited by electromagnetic radiation of sufficient energy, electrons from the conduction band are instantaneously promoted to energy levels above the Fermi level creating a non-equilibrium electron distribution consisting of high energy electrons (hot electrons) and positive vacancies (hot holes).[35] Molecules at the metal surface can then interact with these excited carriers, resulting in chemical processes such as oxidation, reduction, or desorption.[64] In the case of bulk metal substrates this process is inefficient due to the high reflectivity of most metals to visible irradiation.[35] However, by exploiting the high extinction cross section and ability to localize electromagnetic fields of noble metal nanoparticles this generation of hot carriers is more efficient and can be used to drive chemistry on the nanoscale.[36, 46] This is a direct result of the fact that noble metal nanoparticles have a localized surface plasmon resonance in the visible region. The decay of this plasmon resonance then results in a hot carrier distribution analogous to the bulk metal system, but with much higher efficiency with respect to incident laser intensity.[59] Now the field of plasmon driven chemistry has demonstrated applications including energy conversion[36, 44] and catalysis[39-43, 45] at the nanoscale. However, the fundamental mechanisms, time scales, and driving forces still remain a mystery. For these reasons plasmon driven chemistry poses many questions that will continue to be researched for many years.

Besides plasmonic chemistry, the initial non-equilibrium electron distribution also drives phonon mode oscillations.[70, 99, 100] Immediately following excitation of the plasmon resonance and hot carrier distribution, the electrons begin to cool via electron-electron collisions on the femtosecond (fs) timescale.[100] The resulting thermalized electron distribution then couples to the phonon modes of the metal lattice resulting in phonon oscillations on the picosecond (ps) timescale.[100] By monitoring the LSPR as a function of time with respect to the initial excitation a far-field response to the local environment can be measured. The result is an initially broadened LSPR due to the thermalized electron distribution.[70] After this distribution begins to equilibrate with the metal lattice, the oscillation of the phonon modes causes correlated shifts in the LSPR.[70] The measured intensity of the LSPR as a function of time yields insight to the NP size, degree of expansion due to phonon oscillations, and monodispersity.[70, 101] While these dynamics are well understood, they provide a good basis for demonstrating the feasibility of time-resolved surface-enhanced Raman techniques.

Femtosecond stimulated Raman scattering has been successfully used to monitor the vibrational signature of molecules with both high temporal resolution (10–100 fs) and high spectral resolution (5–20 cm-1).[102, 103] However, these experiments necessitate high analyte concentrations and large Raman cross sections. In effort to combat these challenges early attempts were made by Ploetz et al. to combine the high enhancement factors of plasmonic substrates with FSRS but using a 1 kHz repetition rate laser system and a resonant plasmonic substrate they were unable to observe surface-enhanced FSRS signals.[104] By using a 100 kHz repetition rate laser system with average powers high enough for signal generation, but low peak powers to avoid substrate damage, the Van Duyne group was able to successfully combine SERS and FSRS in 2011.[105] This proof-of-

principle paper presented ground-state SE-FSRS spectra with characteristic Fano-like lineshapes. The authors conservatively estimated time- and ensemble- averaged enhancement factors for SE-FSRS to be 10^4-10^6, however this estimated EF was limited by sample degradation. While the dependence of SE-FSRS gain on Raman pump power was shown to be linear in extremely low power regimes, with increasing power sample degradation resulted in a signal decreased on the minutes timescale. In order to improve the signal to noise ratio (SNR) of SE-FSRS both concentration and pathlength were varied to find the optimal balance between signal generation and probe extinction.[106]

Herein we will apply the newly developed SE-FSRS technique to monitor the molecular response to plasmon excitation. For this a colloidal solution of bypridine functionalized gold nanoparticle oligomers encapsulated in a silica shell is excited by a 532 nm actinic pulse. The resulting non-equilibrium distribution in the gold nanoparticle and the molecular response to this is probe by a FSRS probe pair consisting of a 1.5 ps 800 nm Raman pump and 100 fs broadband Raman probe. The measured SE-FSRS response contains information pertaining to both the electronic and molecular components as a function of actinic pulse delay. This information can be directly attributed to the process of electron delocalization and subsequent electron cooling through correlated transient absorption (TA) measurements which captures the purely electronic response.

5.3 Experimental Details

Functionalized gold nanoparticle oligomers. Gold nanoparticle oligomers consisting of 90 nm spherical nanoparticles functionalized with bipyridyl ethylene encapsulated in a 60 nm

thick silica shell were sourced from Cabot Security Materials. Samples for TA and FSRS measurements were diluted 1:100 with Milli-Q water (18.2 MΩ/cm) and put in a 2 mm pathlength quartz cuvette.

Transient absorption measurement. Transient absorption measurements were performed with a regenatively amplified ti:sapphire laser system (RegA 9050, Coherent) which produces a 100 fs pulse centered at 800 nm with a repetition rate of 100 kHz (1 W). This is split 50/50 by a plate beamsplitter. Half is used to drive an optical parametric amplifier (Coherent) where 20% is used to generate a white light continuum in a 4 mm thick yttrium aluminum garnet (YAG) plate. The other 80% is double in an angle tuned BBO crystal which is then overlapped with a portion of the white light in a second angle tuned BBO crystal to drive the optical parametric process. The pulses are then passed back through the BBO in the double pass configuration to further amplify the desired visible wavelength. The OPA is tuned to 532 nm to generate the actinic pulse for these experiments. The actinic pulse is directed through a motorized retroreflector with the equivalent of approximately 150 ps of range (Newport Optics) to provide the time delay. The broadband continuum and actinic paths are then combine using a dichroic mirror and focused collinearly on the sample plane. Temporal overlap is verified by SFG in a BBO crystal in the sample plane. For acquisition the actinic beam is modulated at 500 Hz by an optical chopper synchronized to a CCD (PIXIS, Princeton Instruments) and spectrometer (Spectra-Pro 2300i, Princeton Instruments) using a custom LabView program to collect the data and control the delay stage. For various actinic pulse delays ranging from -5 ps to 60 ps, 1 second acquisitions are taken in random order. This was repeated for a total of 5 sets, which were then averaged.

Surface-enhanced femtosecond stimulated Raman scattering measurements. For SE-FSRS measurements the same regeneratively amplified system is used as the transient absorption experiments. To drive the FSRS process a Raman pump pulse is generated using the portion of the fundamental split off before the OPA. The 100 fs pulse centered at 800 nm is sent through a homebuilt spectral grating filter to reduce the bandwidth to 10 cm^{-1}, stretching the pulse to 1.5 ps. The Raman pump is then sent through an adjustable retroreflector and then combine with the broadband continuum and actinic pulse using a dichroic mirror and focused collinearly on the sample plane. Temporal overlap is verified by SFG in a BBO crystal in the sample plane. For acquisition the Raman pump beam is modulated at 500 Hz by an optical chopper synchronized to a CCD (PIXIS, Princeton Instruments) and spectrometer (Spectra-Pro 2300i, Princeton Instruments) using a custom LabView program to collect the data and control the delay stage. For ground state SE-FSRS spectra, the actinic pulse is blocked and the Raman pump is modulated to measure the FSRS gain; typical spectra are acquired for 10 seconds. For excited state SE-FSRS spectra the actinic pulse is incident on the sample but not modulated, the Raman pump is again modulated to measure the FSRS gain. For the time dependent data sets, for various actinic pulse delays ranging from -5 ps to 60 ps, 10 second acquisitions are taken in random order plus a ground state spectrum (actinic blocked). The sample was replaced to prevent degradation from long acquisition times and the measurement was repeated for a total of 5 sets,

which were then averaged and the ground state spectrum was subtracted to determine the change in FSRS gain induced by the actinic pulse (Figure 5.1).

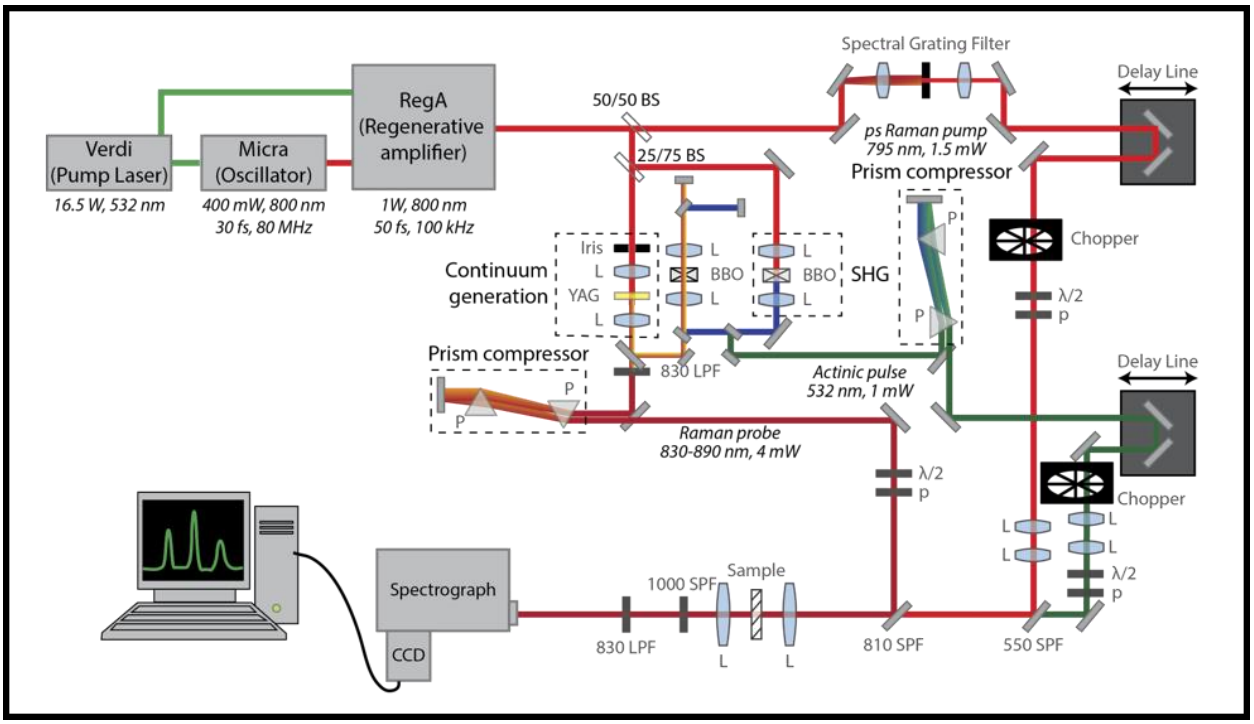

Figure 5.1. Experimental apparatus for transient absorption and surface-enhanced femtosecond stimulated Raman scattering measurements.

5.4 Results and Discussion

In order to build a fundamental understanding of the gold nanoparticle response on our system, we first examined the gold nanoparticle oligomer samples using previously established transient absorption experiments.[69] For this experiment an actinic pulse centered at 532 nm (150 fs, 500μW) is used to excite the monomer plasmon resonance of the gold nanoparticles. This is overlapped at the sample with a near-IR broadband continuum to probe the response of the nanoparticles in the dimer region (Figure 5.2. inset). The delay of the actinic pulse is varied from -5 to 60 ps with respect to the broadband probe to measure the transient response of the colloidal

sample to plasmon excitation. The delays were measure in random order and averaged across 5 sets of experiments to negate any effects of sample degradation. The time trace for this experiment is shown in Figure 5.2 for a probe wavelength of 875 nm. At zero delay between the actinic and probe pulses and an immediate increase in the extinction is measured due to the initial broadening of the LSPR upon electron delocalization.[69] The hot distribution immediately begins to cool, causing the increased extinction to subside over the course of picoseconds. This process is fit wit a single exponential decay; the fitted parameters give a decay time, τ, of 2.7 ps which is similar to other measurements in the literature on gold nanoparticles.[79] At longer time delays we do not observe phonon oscillations in the transient spectra, which is most likely a result of the low peak power of the actinic pulse as most studies rely on 1 kHz systems as opposed to our 100 kHz system. We do see, however, that at longer delay the transient change in extinction does not return to zero but rather stays slightly positive indicating some heating of the nanoparticle lattice, which is understood through the two-temperature model.[107] This established case provides us a framework to understand and describe the SE-FSRS measurements to follow.

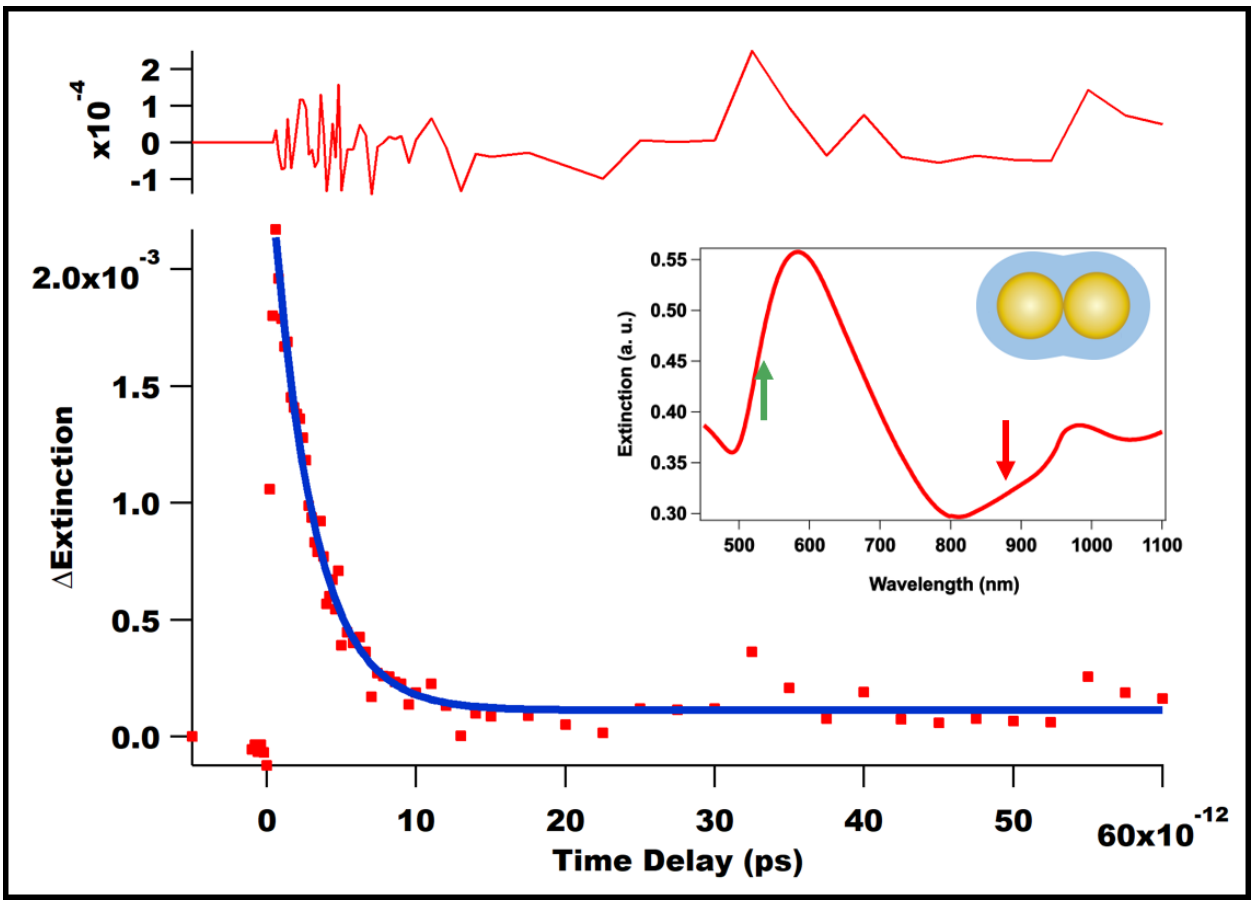

Figure 5.2. Time profile of the change in extinction of the colloidal nanoparticle solution. The inset shows the steady state extinction spectrum of the sample. The actinic pulse is centered at 532 nm (500 μW) and the sample is probed at 875 nm. The decay time is fit with a singe exponential for a τ=2.7 ps. The residual of the fit is present in the top panel.

With our substrate well characterized though traditional transient absorption experiments, it is time to probe the molecular response via SE-FSRS. In these experiments the 532 nm actinic pulse excites the same process, but here the molecular response is probed with a FSRS probe pair consisting of a 1.5 ps Raman pump at 800 nm and 100 fs stokes shifted broadband probe pulse. The experiment is repeated with varying time delay between -5 and 60 ps, then the 'ground-state' spectrum is subtracted from the set of excited state spectra to provide the change in SE-FSRS gain as a function of time delay. All of the spectra were collected at randomly selected time delays in a

variable order and averaged over 5 individual experiments to ensure effects from sample degradation did not appear as time dependent features. The results presented in Figure 5.3 show select spectra from the time series, both before and after excitation. Its apparent from the negative time delay spectra that before the actinic pulse no activity is occurring, and our system fully relaxes between subsequent pulse sets. At zero time delay between the actinic and probe, immediate FSRS gain depletion is visible, which increases to about a 10% loss in signal. Then the FSRS gain starts to return to baseline levels around 5 ps. The initial FSRS gain depletion can be attributed to the initial electron delocalization in the plasmonic structure, decreasing the efficiency of the FSRS process. As the electrons cool and transfer their energy to the phonon modes of the gold nanoparticles, the FSRS gain returns to baseline levels.

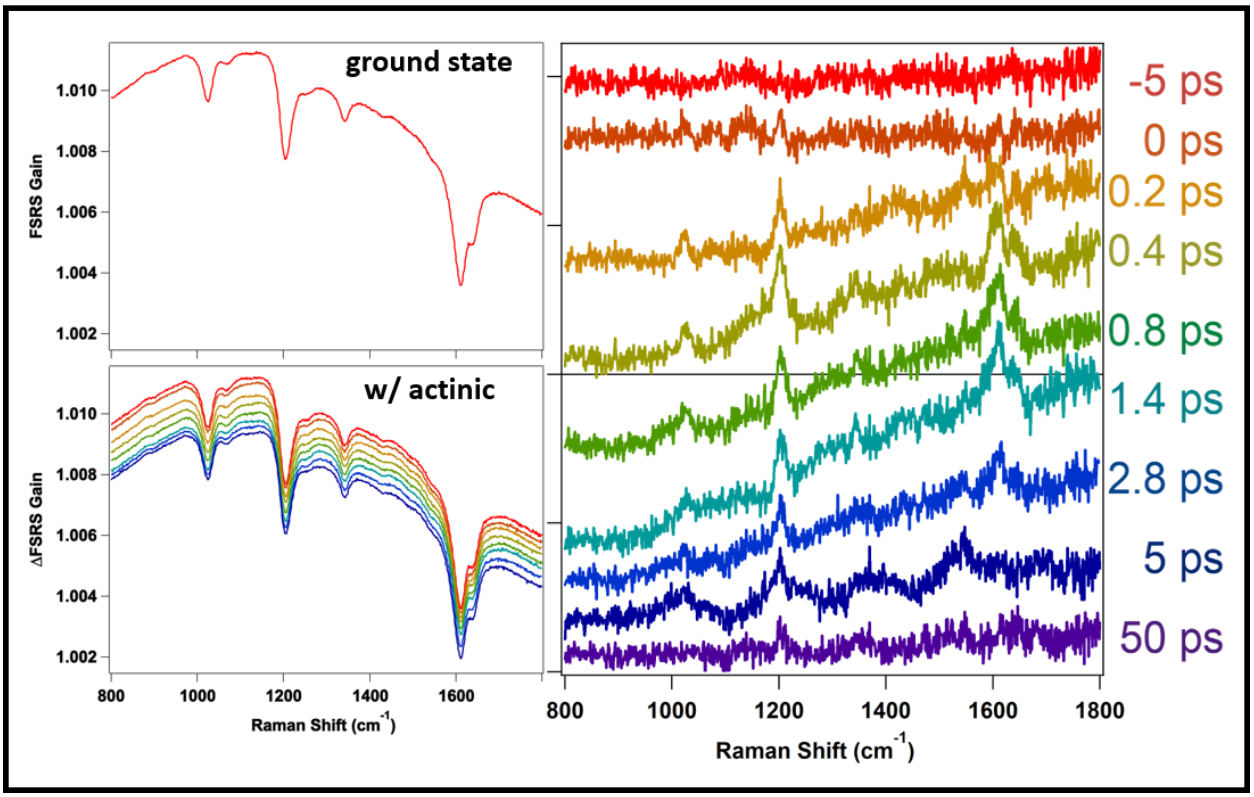

Figure 5.3. Representative spectra from the SE-FSRS dataset. The top left shows the ground state SE-FSRS spectrum of BPE exhibiting the characteristic peaks and dispersive line shapes. The bottom left panel show select SE-FSRS spectra with actinic pump offset for clarity. The spectra in the right panel are produced by subtracting the ground state spectrum from the spectra in the lower left panel. With this you can see the time dependent features in the depletion of SE-FSRS signal and the change in background.

To look at this effect in the SE-FSRS experiment it is easier to look at a single Raman shift as a function of time. Select time profiles for the SE-FSRS experiment are presented in Figure 5.4 for direct comparison to the analogous TA experiment. Looking at the time-profiles it appears that the depletion and return of the FSRS signal is correlated to the electron delocalization observed in the TA experiments. To verify this the decay profiles are fit with a single exponential and compared to the TA result. For the 1204 cm^{-1} vibrational mode the decay is fit to a τ of 2.9 ps, while the 1610 cm^{-1} vibrational mode had a decay constant of 2.5 ps. The values are in excellent

agreement with the TA result of 2.7 ps for the electron delocalization process, so the signal depletion can be confidently attributed to that process. The peaks at 1641 cm^{-1} and 1027 cm^{-1} were also analyzed in this manor to yield decay constants of 2 ps, but due to the signal to noise in these time profiles it is difficult to say the difference in decay time is significantly different than the other vibrational modes. The SE-FSRS background was also probed during these measurements and its time dependence can be examined by looking at an off resonant portion of the spectrum. Using the intensity at 900 cm^{-1}, near the 875 nm probe position in TA measurement, a time profile can be obtained. Subsequent fitting results in a decay constant of 1.8 ps, which is significantly shorter than the measured cooling in the TA experiment of 2.7 ps.

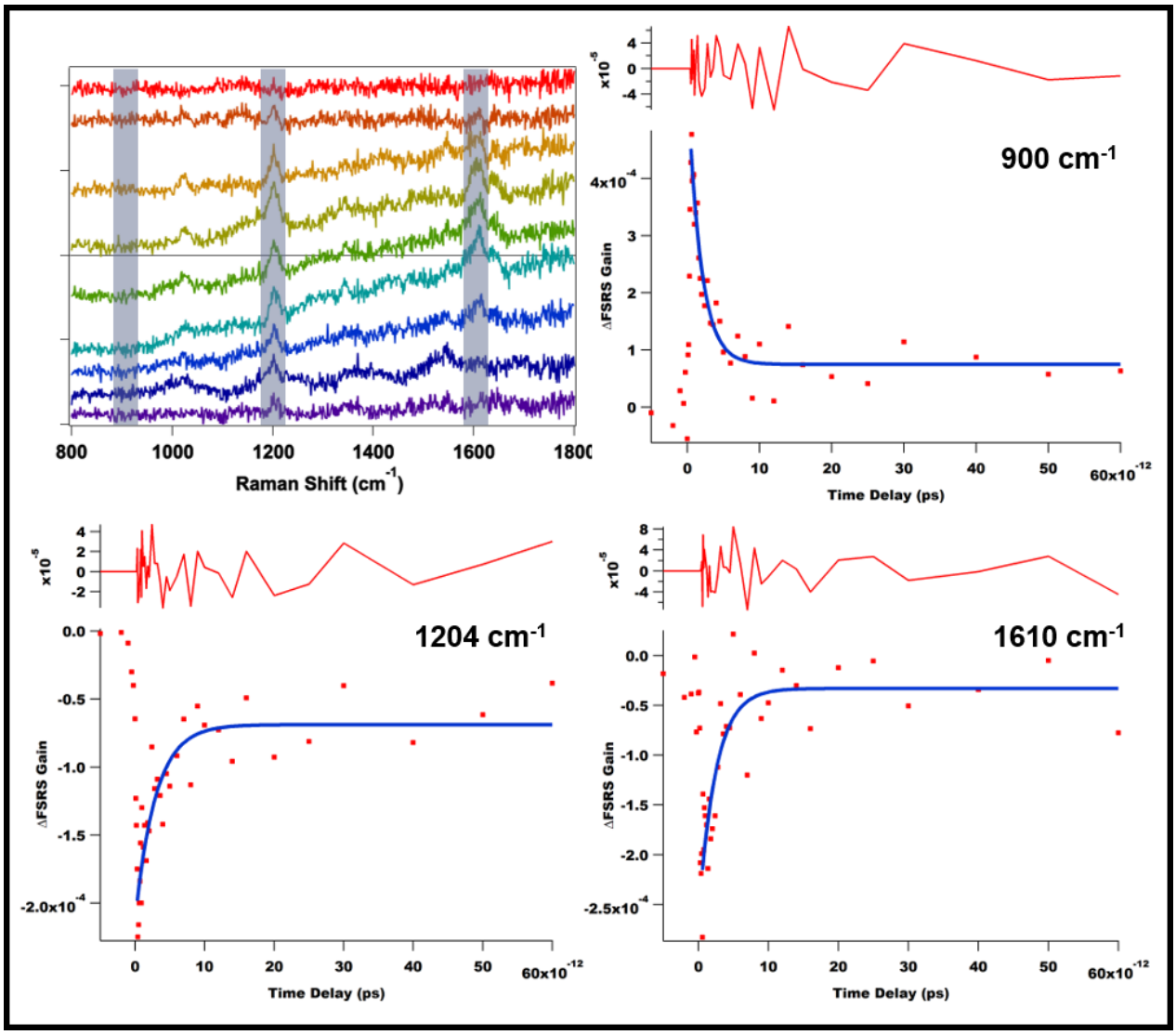

Figure 5.4. The three regions highlighted in the top left panel are plotted as a function of actinic pulse delay to compare the relaxation times to the transient absorption experiment. The region at 900 cm^{-1} is off of a molecular resonance and shows the behavior of the SE-FSRS background (top right). The single exponential fit yielded a decay constant τ=1.8 ps. For the 1204 cm^{-1} vibrational mode (bottom left) the change in peak amplitude is fit to a decay constant τ=2.9 ps. For the 1610 cm^{-1} vibrational mode (bottom right) the change in peak amplitude is fit to a decay constant τ=2.5 ps.

This difference can possibly be explained through the two-temperature model.[107] The LSPR response measured by TA has components related to both the electronic temperature and the temperature of the nanoparticle lattice.[69] Electron cooling leads to heating of the lattice

resulting in a slight variation in extinction over the picosecond timescale. At delays close to time zero both of the mechanisms are at play and contribute to the measure response in TA experiments. However, in SE-FSRS experiments the non-vibrationally resonant background only captures the electronic response of the gold nanoparticles leading to a faster return to baseline levels. Additionally, the vibrational modes of the molecules do see this local temperature rise so the decay times for their response more closely match the TA experiments.

Interestingly, in all cases and at all time-delays, no features attributed to transient species were observed despite the observation of plasmon-driven chemistry reported for both BPY and BPE in continuous wave experiments. This can be indicative of a few things. First, it is possible and likely that the plasmon response to femtosecond pulse and continuous wave excitation is quite different. While it is well known pulsed excitation is not equivalent to cw excitation, it is not straight forward why the femtosecond pulses are not generating enough hot carriers to be seen in transient experiments and why cw excitation is able to efficiently generate and measure transient species that appear to be generated by hot carriers. The answer to this may be the simplest one; plasmon driven chemistry is too inefficient to be observed with current time resolved experiments. Looking at the estimated yields from plasmon driven reactions in the literature, even the most efficient ones only reach ~1% conversion. While this doesn't directly indicate the populations that are present in a plasmonic hot spot, it does hint that these species could be present in our experiment but simply not observed. With the current signal to noise ratio a transient species would have to comprise about 10% of the molecular species measured and occur simultaneously. Unfortunately for most plasmon driven processes, yields of this magnitude have not been realized and transient species often occur randomly in time and exist for periods of seconds. While this is

not the ideal result it does not spell certain doom for plasmon driven chemistry or time resolved surface-enhanced coherent Raman techniques. Further development and knowledge of the field will almost certainly result in increased yields and higher signal to noise ratios, allowing for a revisiting of these experiments.

5.5 Conclusions

For the first time, we have demonstrated time-resolved SE-FSRS. By pumping the plasmon resonance of a colloidal sample of gold nanoparticle oligomers functionalized with bipyridyl ethylene with a 532 nm actinic pulse and probing the subsequent dynamics with a Raman pump and broadband probe to drive the FSRS process, we observed a transient response. The response for various vibrational modes as well as the FSRS background were examined as a function of actinic pulse delay to determine the decay constant for the process observed. An apparent decay constant of 2.5 - 2.9 ps was measured for the vibrational modes, while the FSRS background dependent on the electronic cooling process relaxed faster with a decay time of 1.8 ps. Transient absorption experiments performed on the same samples verified that the transient response in the SE-FSRS spectra is a result of plasmon excitation and its subsequent relaxation.

CHAPTER 6

Surface-Enhanced Raman Excitation Spectroscopy:

Probing Hybrid Plasmon-Molecular Resonances

6.1 Abstract

Recent works have demonstrated that a strongly coupled plasmon-molecule system can be formed through assembly of j-aggregates on the surface of silver nanoprisms. By tuning the size of the silver nanoprisms the effective coupling between the plasmonic and molecular resonances can be controlled. It has been postulated that these strongly coupled systems can be used to manipulate and/or control chemical reactivity by tuning the overlap of the contributing resonances. Towards this goal, we first investigate how the properties of the hybrid resonances change as the plasmon is tuned from the blue of the molecular resonance to the red. For this we employ Raman excitation spectroscopy, where Raman spectra are collected for various excitation wavelengths over the spectral range of the hybrid resonances and compared to a non-resonant standard to determine the relative Raman enhancement for a given vibrational mode. The resultant Raman enhancement profile is indicative of the contributing resonance and its spatial overlap with molecules on the nanoparticle surface. For these strongly coupled molecule-plasmon systems we observe that in all splitting regimes the Raman enhancement profiles are dominated by a single resonance despite the splitting observed by UV-Vis spectrophotometry. Furthermore, when the plasmon is tuned from the blue to the red of the molecular resonance, the observed resonance red shifts. The dependence of the enhancement profile maximum on the vibrational mode energy is also decreased as the resonance red shifts, mirroring the shift in behavior that occurs when transitioning from plasmonic enhancement to resonant Raman enhancement. The possibility of tuning the observed resonance from a plasmonic to a molecular one is discussed, while other possible explanations are outlined as well.

6.2 Introduction

Strong coupling is a non-perturbative regime of light-matter interaction, in which the rate of coherent energy oscillation between optical modes and excitons exceeds their individual spontaneous decay rates. For this to occur, the exciton must have high oscillator strength, the cavity must confine light for long periods of time, and/or the light must be confined to extremely small volumes. Classically this has been observed using high quality factor cavities that confine light for long periods, allowing for repeated interaction with a cloud of atoms that provide a high oscillator strength excited state with a well resolved frequency. More recently this has been experimentally achieved by employing plasmonic nanostructures which are very low quality factor cavities but they have the ability to confine light into subwavelength mode volumes[108]. These confined modes are then coupled with high oscillator strength quantum emitters, like organic dye molecules,[108, 109] J-aggregates,[110-113] quantum dots,[114] and two-dimensional transition metal dichalcogenides (TMDC).[115-117] Besides the fundamental interest in manipulating light-matter interactions on the nanoscale, plasmon-exciton strong coupling also has promising application-potential for single-photon high speed switches,[6, 7] hybrid waveguides,[118] light-harvesting devices[119, 120] and control of chemical reaction pathways.[121-123]

The most prominent feature of plasmon-exciton strong coupling is the two new hybrid modes generated by coupling the plasmonic and molecular resonances, referred to as Rabi splitting.[124] This energy level splitting behavior provides a new method to possibly manipulate the energy landscapes of chemical reactions. If the plasmon and exciton are both treated as harmonic

oscillators and the damping is neglected, the energy levels of the two split hybrid eigenstates can be theoretically expressed as:[124, 125]

$$E_{\pm}(\omega_p) = \frac{1}{2}(\omega_p + \omega_0) \pm \frac{1}{2}\sqrt{g^2 + (\omega_p - \omega_0)^2} \qquad \text{(Equation 6.1)}$$

Here ωp is the plasmon resonance frequency, ω0 is the exciton resonance frequency and g is the coupling constant. Equation 6.1 describes the split energy levels of the hybrid eigenstates, as the coupling is increased the energy difference between the two resonances increases. This coupling constant is directly related to the quality factor of the cavity as well as the inverse volume. Therefore, in order to observe Rabi splitting using a plasmonic cavity, you must have a very small mode volume.

The near field behavior of plasmonic resonances has been exploited to provide electromagnetic field enhancement to boost the Raman scattering process by Surface enhanced Raman scattering (SERS) experiments since its discovery in 1977.[12] Since, field enhancements of up to 10^3 have been reported using aggregated noble metal nanostructures.[3] The near field properties of these field enhancements have also been probed in depth by excitation dependent SERS experiments, revealing the presence of near-field dark modes that significantly contribute to the enhancement of the Raman scattering signal and the localization of fields on the nanoscale[13]. Similarly, the Raman scattering process can be enhanced by the presence of a molecular resonance, known as Resonance Raman scattering (RRS). When the Raman excitation wavelength is aligned with a molecular resonance, Raman signals can be enhanced up to ~10^3 but is strongly dependent

on the molecular species.[25] These two techniques have also been combined in surface-enhanced resonance Raman scattering (SERRS). Together these two enhancement mechanisms work multiplicatively allowing for enhancement factors up to 10^{12}, enabling single molecule sensitivity in Raman experiments.[126]

While both of these enhancement mechanisms result in an increase in the observable Raman scattering signal, their dependence on excitation wavelength allows them to be distinguished in excitation dependent Raman scattering experiments. For Resonance Raman, the enhancement of an individual vibrational mode is dependent on the overlap of the vibrational normal mode with the transition dipole of the electronic transition. This mechanism provides enhancement to the polarizability of the molecule, increasing the induced dipole measured through Raman scattering. Inagaki[27] and Myers[26] demonstrated that for the case of Raman excitation spectroscopy around a molecular resonance, the Raman excitation profiles have the same peak position and similar lineshape as the absorption spectrum of the resonant molecule.

For the case of SERS, the enhancement mechanism is quite different. When molecules are at or near the surface of a plasmonic nanostructure, the Raman signals can be enhanced up to 10^7~10^8 due to the enhancement of the local electric fields.[3] The plasmonic enhancement of SERS is directly dependent on the enhancement of the electric field at both the excitation wavelength and the stokes scattered wavelength of the observed vibrational mode. Surface-enhanced Raman excitation spectroscopy (SERES) was first demonstrated in 2005.[28] In this work, periodic particle arrays (PPA) of gold nanotriangles fabricated by nanosphere lithography were used as SERS substrates. They found that the Raman excitation profiles were blue shifted compared to the

localized surface plasmon resonance (LSPR) of PPAs and the shift for a given normal mode was approximately half of the vibrational energy, which can be explained by the electromagnetic (EM) mechanism of SERS (Equation 6.2).[11]

$$I_{Raman} \propto \frac{|E(\omega_{exc})|^2 |E(\omega_{exc} - \omega_{vib})|^2}{|E_0^4|} \qquad \text{(Equation 6.2)}$$

Later works found that in the hot-spot-dominated plasmonic nanostructures like gold nanoparticle dimers, the Raman excitation profiles did not have a clear correlation with the far field LSPR spectral position.[13] Further computational work on the dimer hot-spots revealed that plasmonic "dark" modes, which are not seen in the far-field measurements, also greatly enhance the electromagnetic field near the hot spot.[13] These two techniques were combine in a final study to investigate the interplay between the molecular resonance and the plasmon in terms of scattering enhancement.[127] They focus on probing the molecular resonance and find that the enhancement profile follows the absorbance of the rhodamine-6G molecules on the silver surface. While they do not aim to directly probe the plasmon resonance they clearly see it contribution on the blue side of the absorption spectrum, indicating the enhancement mechanism exist concurrently. This body of previous work shows that Raman excitation spectroscopy is a powerful tool for analyzing the near-field response of plasmon-molecule systems.

In this paper, we conducted surface enhanced Raman excitation spectroscopy (SERES) on the Ag nanoprism/TDBC J-aggregates strongly coupled system. In the past the biggest problem of SERES was the low data point density limited by the tunability of laser system.[28] To overcome

this problem, we used a tunable continuous wave laser system which covers a broad spectral range from 305-1000 nm with fine spectral linewidth of 0.0001 nm. It enables collection of Raman spectra over the visible region to cover the split, hybrid resonances of the strongly coupled systems. Measuring the enhancement of the individual vibrational modes of the TDBC molecules located within the strongly coupled structures compared to a non-resonant standard, allowed for detailed enhancement profiles to be formed. By repeating this measurement on strongly coupled samples using various sizes of Ag nanoprisms, we were able track the contribution of the plasmon resonance to the SERS excitation profiles. We found that the SERES profiles of different samples always have one dominate peak, unlike the UV-Vis spectra that show splitting in the samples. This indicates that the Raman enhancement is being dominated by a single plasmonic mode located near the molecular resonance. As the nanoprism size is increased the enhancement profiles have a reduced dependence on the vibrational mode measured indicating higher overlap of the plasmonic mode with the molecular resonance of the TDBC J-aggregates. Correlated darkfield-TEM measurements found a stacked nanoprism structure leads to observable Rabi splitting and high enhancements. This suggests the far-field hybrid resonances measured by UV-Vis are dominated by monomer nanoprisms encapsulated in TDBC j-aggregates. However, the near-field response as measured by SERES is dominated by the dark modes of the aggregated Ag nanoprism/TDBC structures that provide significantly more electromagnetic enhancement due to the high degree of localization at plasmonic hotspots where TDBC j-aggregates are located. These results imply that despite significant splitting observed in the far field, the highest degree of electromagnetic field interaction with molecules on the nanoprisms' surface will occur at energies near the molecular resonance of the TDBC j-aggregates and is largely invariant with nanoprism size.

6.3 Experimental Details

Sample preparation. Silver nanoprisms were synthesized with a two-step seeded growth method adapted from literature.[128] First, 5 mL $AgNO_3$ aqueous solution (0.5mM) were added at a rate of 2 mL/min to 5 mL trisodium citrate (2.5mM), 250 μL poly(sodium 4-styrenesulfonate) (500mg/L) and 300 μL freshly-prepared $NaBH_4$ solution (10mM) to produce Ag seeds approximately 5 nm in diameter. Second, 3 mL $AgNO_3$ aqueous solution (0.5mM) was added at a rate of 1 mL/min to 5mL of an aqueous ascorbic acid solution (150 μM), immediately following the addition of Ag seed solution. The amount of Ag NP seed solution ranged from 20 -400 μL to produce silver nanoprisms with different LSPRs. During the synthesis the rate of adding silver nitrite solution was controlled with a syringe pump (Harvard Instruments). 5,5′,6,6′-tetrachloro-1,1′-diethyl-3,3′-di(4–sulfobutyl) -benzimidazolocarbocyanine (TDBC) was purchased from Alfa Aesar (95%). TDBC forms J-aggregates when dissolved in an aqueous solution of KBr (1 mM). The plasmon-molecule strongly coupled samples were prepared by adding TDBC J-aggregate solution (1mM) to silver nanoprism colloids in a ratio of 1:10. The solution was centrifuged and resuspend in water twice to remove excess dye.

Vis-NIR extinction measurement. The extinction spectra of all the samples in the solution were obtained by a spectrometer (Cary 5000, Agilent Technologies) in double beam mode. Quartz cuvettes with a pathlength of 2 mm were used for all measurements.

Surface-enhanced Raman excitation spectroscopy. The strongly coupled samples with different sizes of Ag nanoprisms were mounted in a 3D printed sample holder on an auto stage

(Thorlabs) controlled by a Labview program. The Raman signals were collected with a TriplePro three-stage spectrometer (Princeton Instruments, SpectraPro 300i) equipped with a thermoelectrically cooled CCD detector (Princeton Instruments, ProEM 1024). The laser excitation was provided by M squared tunable continuous wave laser system which covers a broad spectral range from 305-1000 nm with fine spectral linewidth of 0.0001 nm. In the experiments, Raman spectra of pure cyclohexane under each excitation laser wavelength was acquired as an intensity standard. The SERS intensity of TDBC J-aggregates were all normalized to the intensity of cyclohexane 801 cm-1 Raman mode to correct for instrumental variations and each wavelength.

Transmission electron microscopy imaging. About 7 μL Ag nanoprism/TDBC J-aggregates solution was dropped on the TEM grid (Ultrathin type A TEM grid from Ted Pella) and dried in air. The TEM images were obtained by a Hitachi-8100 TEM using 200 kV of thermionic emission.

6.4 Results and Discussion

Silver nanoprisms (NP) of varying sizes were synthesized using a previously reported seeded growth method.[128] This allows for straight forward control of the resulting Ag NP size, allowing for a plasmonic substrate with a highly tunable LSPR. The nanoprisms are then mixed with an aqueous solution of the j-aggregate, TDBC. After which, centrifugation and resuspension in water yields the hybridized plasmon molecule system. Examination of the resulting hybridized systems using UV-Vis absorption measurements for a sequence of initial plasmon resonances produces an anti-crossing plot characteristic of a strongly coupled system (Figure 6.1).

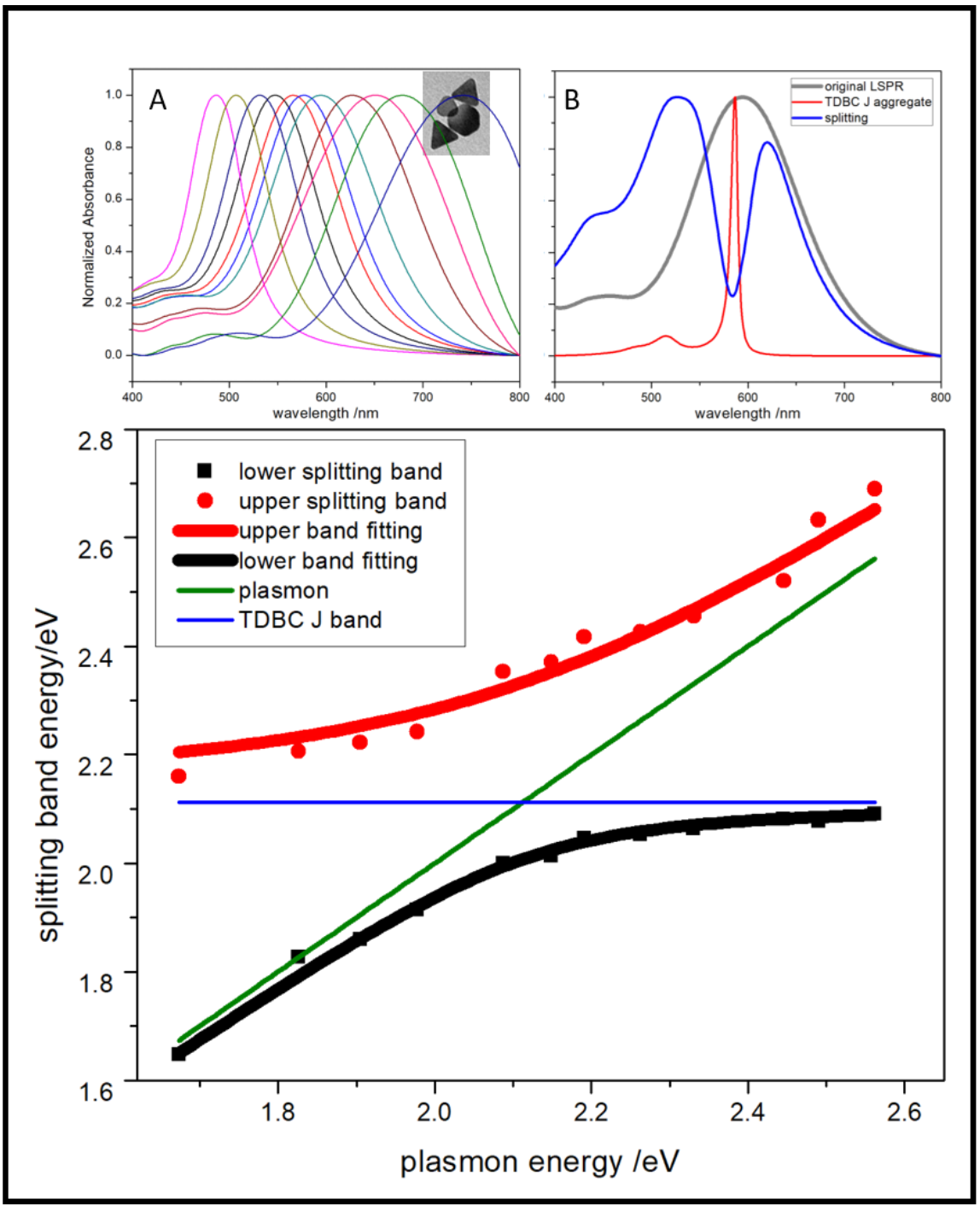

Figure 6.1. a) Shown on the top left is the UV-vis extinction spectra for various sizes of silver nanoprisms, a TEM image of the nanoprisms is in the inset. b) On the top right is the extinction spectra for a strongly coupled sample (blue) shown along with the molecular resonance (red) and LSPR used in the sample (grey). The bottom panel is a plot of the lower and upper band energies as a function of the plasmon energy of the contributing LSPR. This shows the characteristic Rabi splitting of a strongly coupled system.

These hybrid structures now have bimodal absorption spectra as observed from the far-field via UV/Vis absorption measurements. Following the standard energy mixing model for Rabi splitting each of the hybrid modes are a linear combination of the molecular and plasmonic components.[124, 125] The contribution from molecule or plasmon to each mode is dependent on the overlap of the original LSPR and molecular resonance. Thus, for an LSPR that is blue shifted with respect to the molecular resonance, you would expect the upper band (UB) to have mostly plasmonic character and for the lower band (LB) to be mostly molecular. Conversely, for an LSPR red shifted with respect to the molecular resonance the opposite is anticipated

Using Equation 6.2 we can model anticipated enhancement profiles for various vibrational energies and a given a plasmon resonance. If the LSPR is approximated as a Gaussian positioned at 600 nm with a FWHM of 100 nm, then the resulting normalized enhancement profiles calculated according to Equation 6.2 are distributed as shown in Figure 6.2a. In effort to quantify the spread of the enhancement profiles discussed above, the position of the enhancement profile maximum is plotted as a function of vibrational energy and then fit with a linear regression (Figure 6.2c). From this line of best fit we can extract information related to the plasmon resonance producing the enhancement profiles measured. The slope of the line corresponds to dependence of the enhancement on the vibrational mode measured, while the y-intercept indicates the approximate spectral position of the resonance contributing to the enhancement. For this first case modeling a purely plasmonic case yields a slope of 0.60, similar to the dependence found in experimental studies. The y-intercept for this case is 602 nm, a deviation of only 2 nm from the original LSPR used in the calculation. Additionally, if you perform this analysis assuming a solely molecular

resonance you find that the slope of the line is 0 indicating no dependence on the vibrational energy, while the y-intercept still points towards the contributing resonance (Figure 6.2b,d).

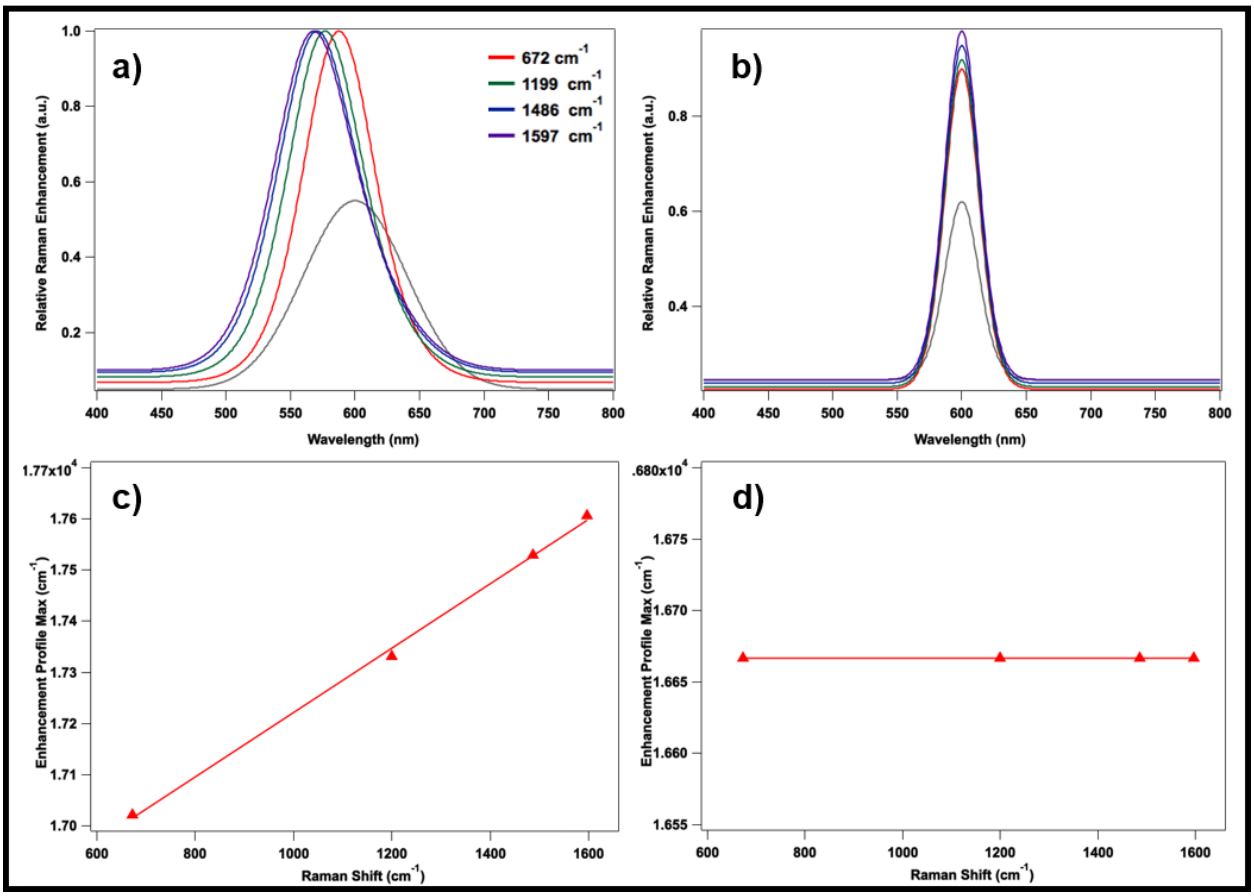

Figure 6.2 a) Modeled plasmonic enhancement profiles for various vibrational modes of TDBC using Equation 6.2 and a gaussian LSPR centered at 600 nm with a FWHM of 100 nm. b) Modeled enhancement profiles for a molecular resonance centered at 600 nm with a FWHM of 50 nm for various vibrational modes of TDBC; it is assumed the enhancement has no dependence on the vibrational mode. c) Position of the enhancement profile maximum plotted as a function of vibrational energy for the modeled profiles in panel (a) and fit with a linear regression (slope = 0.6, y-intercept = 602 nm). d) Position of the enhancement profile maximum plotted as a function of vibrational energy for the modeled profiles in panel (b) and fit with a linear regression (slope = 0, y-intercept = 600 nm).

From the set of strongly coupled samples used to produce the anti-crossing plot, three were selected for Raman excitation experiments, one with an initial LSPR blue-shifted with respect to

molecular resonance (sample 1), one where the resonance are close in energy (sample 2), and one where the LSPR is red-shifted with respect to the molecular resonance (sample 3). When examining our experimental data by comparing the extinction spectrum of the sample to the measured enhancement profile for the various vibrational modes, it is immediately apparent that the two peak structure of the extinction spectrum is not reproduced in the enhancement profiles (Figure 6.3). The enhancement profiles for all of the samples only show a single dominant peak. Highly shifted enhancement regions were probed with various wavelengths from 400-800 nm, but no additional regions with significant enhancement were found. The second observation is that between the 3 samples selected from different regions of the anti-crossing plot, the distribution of the enhancement profiles varies drastically. With the LSPR to the blue of the molecular resonance the profiles are well shifted with respect to one another; however, with the LSPR to the red of the molecular resonance the profiles seem to overlap one another. A similar trend was observed in experiments performed by Zhao et al. who measured the Raman excitation profile of $Ru(BPY)_3$ on a SERS substrate and saw that when the plasmon resonance is near the molecular one the enhancement profiles are multiplicative resulting in a response that favor the spectral position of the excitation wavelength. This results in the enhancement profiles for the different vibrational modes to overlap spectrally. This is similar to what is observed in our experiments, but does not explain why we do not see contributions from both hybrid resonances observed by UV-Vis.

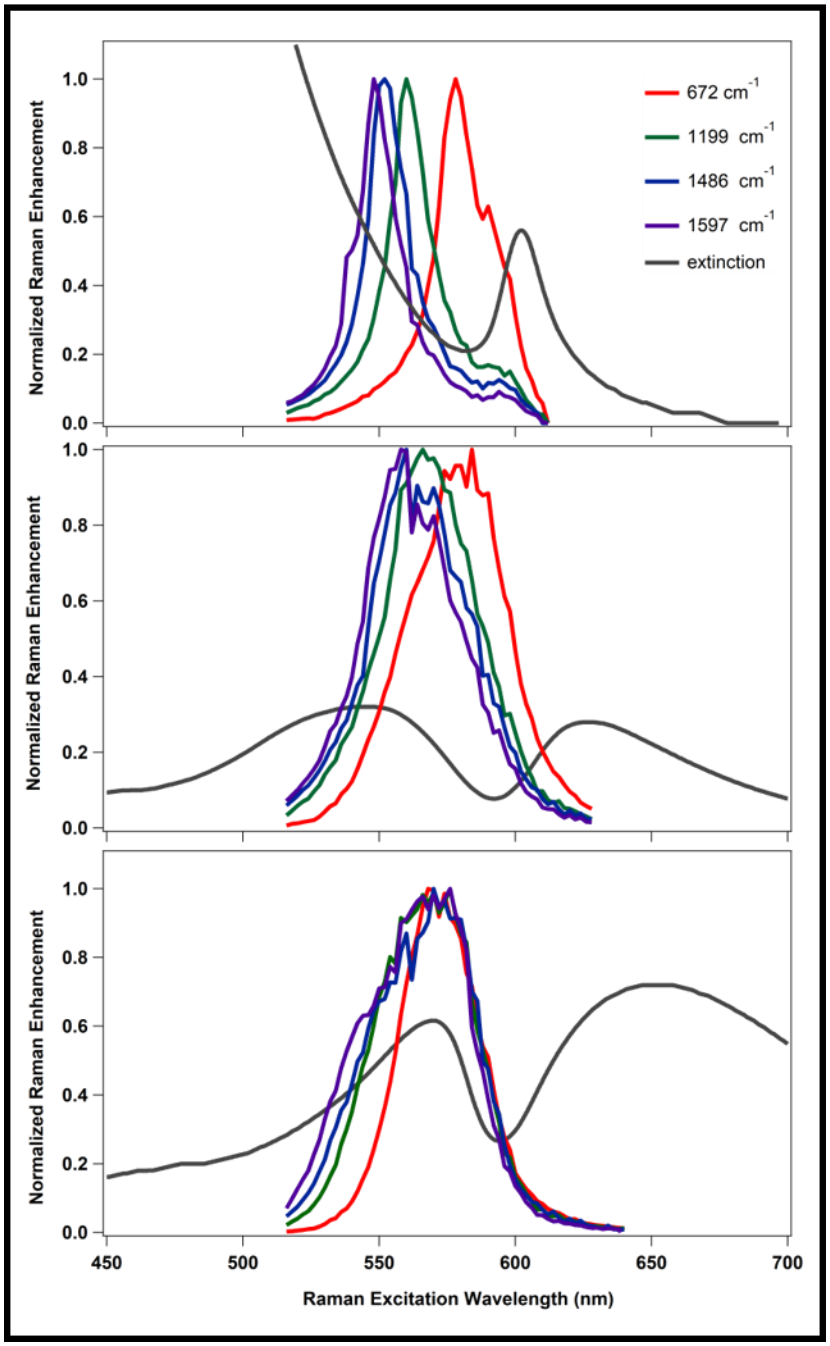

Figure 6.3. Normalized Raman enhancement profiles from three strongly coupled j-aggregate-silver nanoprism samples. The extinction spectrum for each sample is shown in gray for comparison.

By plotting the peak position of the enhancement profile for a given vibrational mode we can quantify this effect (Figure 6.4). For the three sample we see the line of best fit varies dramatically as the nanoprism size is increased. Samples 1 and 2 have slopes greater than 0.5, indicating an increased dependence on the stokes scattered wavelength. These slopes indicate mostly plasmon like behavior. However, for sample 3 the line of best fit shows a slope of ~ 0, indicating almost entirely molecular behavior. A closer look at the widths of the enhancement profiles show that for the higher wavenumber modes the profile is broader that the low wavenumber modes indicating some plasmonic effect, but the molecular resonance dominates the enhancement. While these observations are rather straight forward given the measured enhancement profiles, there is no clear correlation to the measured extinction spectra.

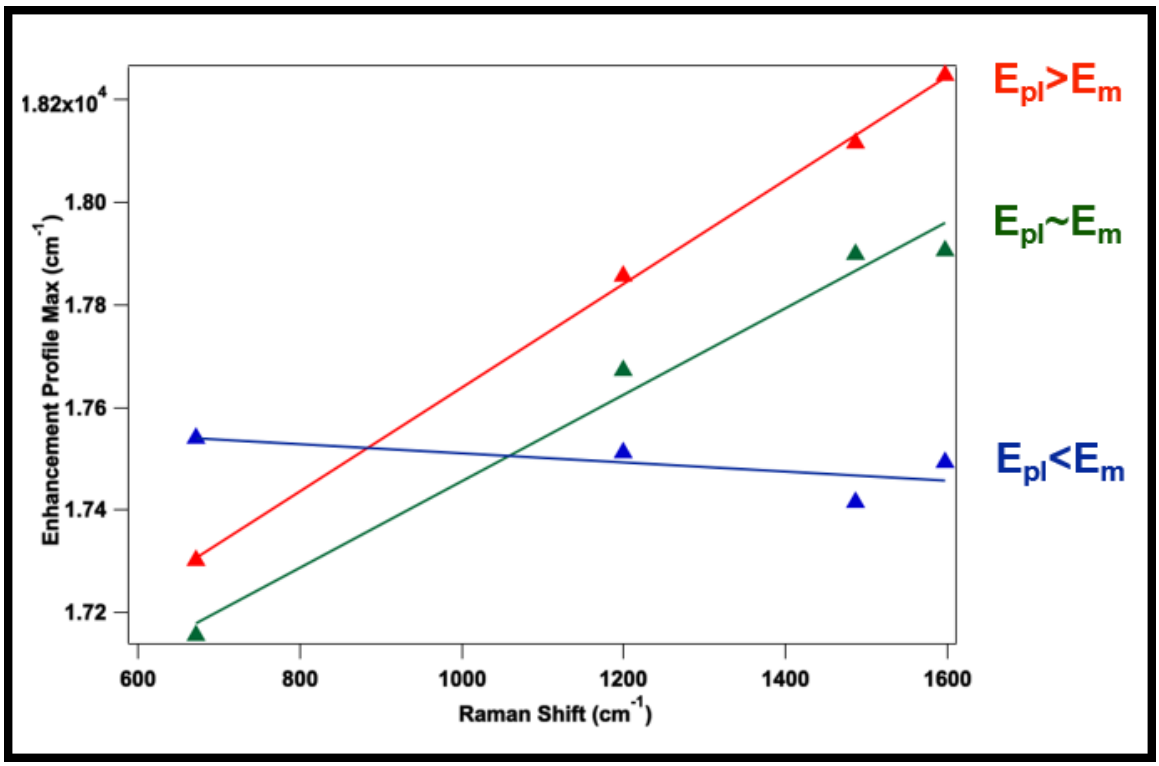

Figure 6.4. Positions of the enhancement profile maximum plotted as a function of vibrational energy for the measured Raman enhancement profiles in Figure 6.3. A linear regression is performed to find a line of best fit. For the red line, the slope is 1 and the y-intercept is 601 nm. For the blue line, slope = 0.8 and y-intercept = 602 nm. For the blue line, slope = -0.1 and y-intercept = 580 nm.

To verify the results we obtained are consistent, we repeated the process with a new batch of strongly coupled samples. Three of these samples were chosen much like the first set to reside in the three distinct splitting regimes. The experiment and analysis are outlined in Figure 6.5. Largely the results are consistent with the first data set. With a plasmon energy greater than the molecular resonance, plasmon like behavior is observed in the enhancement profiles. And when the plasmon is red shifted with respect to the molecular resonance the enhancement profiles exhibit molecular resonance like character.

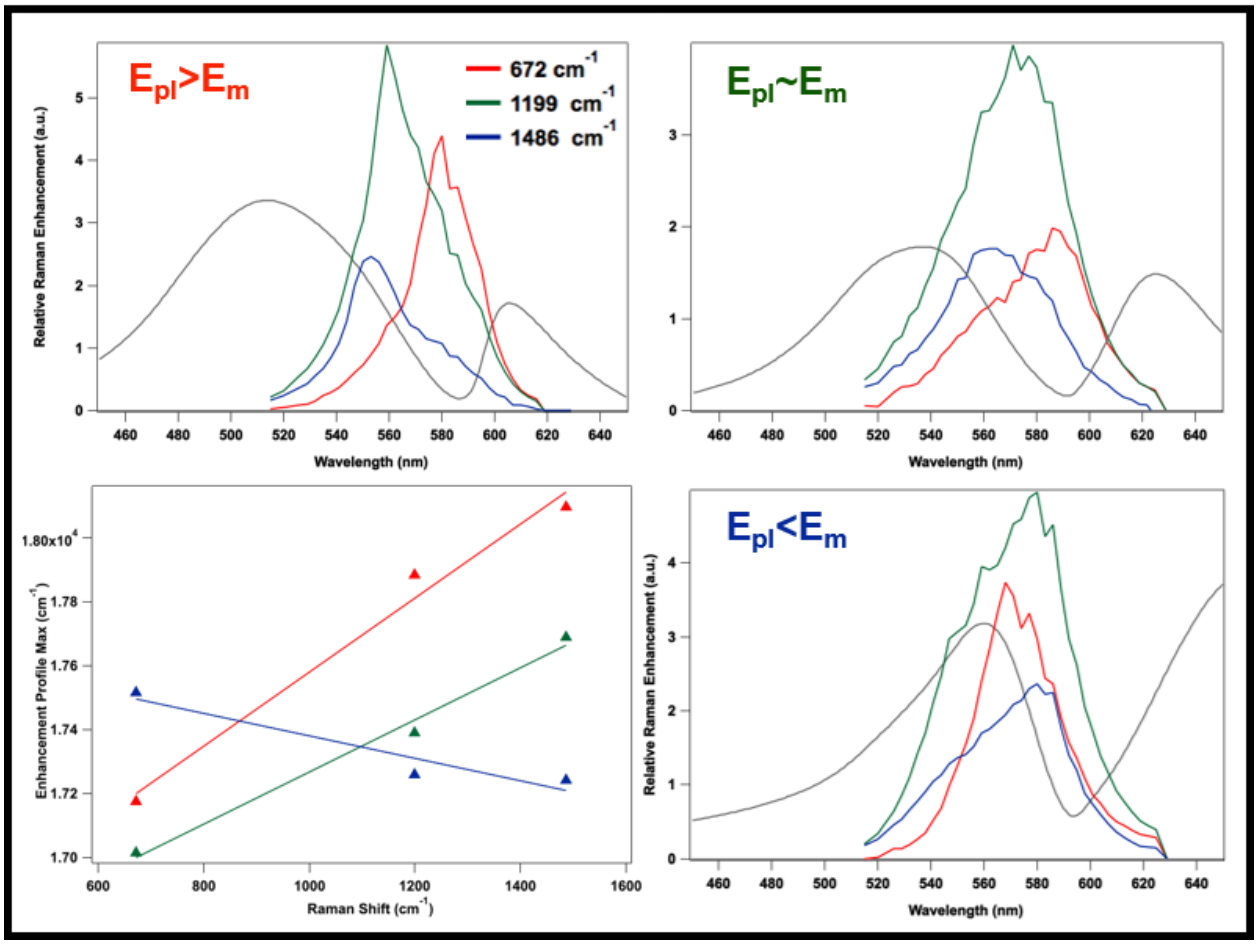

Figure 6.5. Normalized Raman enhancement profiles from three strongly coupled j-aggregate-silver nanoprism samples are shown in the top left, top right, and bottom right panels. The extinction spectrum for each sample is shown in gray for comparison. The positions of the enhancement profile maximums plotted as a function of vibrational energy for the measured Raman enhancement profiles are plotted in the bottom left panel. A linear regression is performed to find a line of best fit. For the red line, the slope is 1.1 and the y-intercept is 608 nm. For the blue line, slope = 0.8 and y-intercept = 607 nm. For the blue line, slope = -0.3 and y-intercept = 560 nm.

In effort to explain these trends, we measured extinction spectra on the single aggregate level through dark-field microspectroscopy and further correlated TEM imaging (Figure 6.6). The subsequent strong-coupling spectra and images informed us that the system was forming stacked structures where the nanoprisms were stacking face-to-face, presumably with interspersed TDBC

j-aggreagates. From previous works we know that plasmonic hotspots between closely spaced nanoparticles lead to the highest degrees of EM field localization and thus enhancement factors.[3] With increasing nanoprism size this gap mode resonance should red shifts slight. If this results in better alignment with the molecular resonance, then the observed enhancement profiles could resemble resonance Raman enhancement profiles due to the increased dependence on the excitation photon. However, verifying this is the operative mechanism would require SERES experiments on the single aggregate level with correlated structural properties and appropriate TDDFT calculation. Regardless, the presence of a single dominant peak in the enhancement profile indicates that the degree of electromagnetic field enhancement and subsequent coupling to the molecule is highest between the two hybrid resonances observed by UV-visible absorption measurements. This seems to indicate that coupling between the plasmon and molecular systems in the highly shifted split resonances is not as significant as the resonance found through the Raman excitation spectroscopy experiments.

6.5 Conclusions

Using recently developed methods we generated a distribution of samples that exhibited characteristics of strong coupling. Using surface-enhanced Raman excitation spectroscopy, the near-field response of the hybrid system was measured as a function of excitation wavelength. In all experiments the Raman excitation profiles exhibited one dominant peak. When the plasmon resonance in the coupled system was of higher or equal energy to the molecular resonance, the enhancement profiles had a strong dependence on the vibrational mode measured. With the

plasmon resonance red-shifted with respect to the molecular resonance, this vibrational mode dependence was diminished. This is likely a result of a gap plasmon resonance not seen by UV-vis measurements that overlaps with the molecular resonance as the nanoprism size is increased. This result seems to indicate that for these systems the larges amount of overlap and interaction between the plasmon and molecular resonances is in the middle of the visible range rather than in the highly shifted regions observed by UV-vis absorption.

Appendix A

An Original Research Proposal:

Reactivity of Titanium Dioxide Nanoparticles in Environmentally Relevant Systems

A.1 Introduction, Background, and Significance

Both titanium dioxide and PAHs present a possible risk to the environmental under intense UV irradiation, due to the toxic photooxidation products they can produce.[129, 130] Sensitization of titanium dioxide in the environment may enable enhanced photo activity of this system under visible light.[131, 132] In fact, degradation of PAHs in soil under UV light in the presence of presence of titanium dioxide has already been observed.[133] In aquatic systems the levels of visible, and even UV-A and UV-B, irradiation are much higher than soil.[134] The PAHs within these environments are likely candidates to be oxidized by the available titanium dioxide nanoparticles.[129, 130, 135] With this in mind, this research aims to evaluate the potential reaction pathways for the photooxidation of anthracene by hydrogen peroxide sensitized titanium dioxide nanoparticles. Using anthracene as a representative PAH and varying reaction conditions including the size of TiO_2 nanoparticles, concentration of H_2O_2, and pH of the solution will allow us to estimate impacts in different environments. Further studies to evaluate environmental implications of sensitized TiO_2 nanoparticles will be done under environmentally relevant conditions. In these studies, a representative population of PAHs in the environment will be added at the appropriate concentration. Degradation of the PAHs will be monitored upon simulated sun exposure for a week. This data along with the previous study of anthracene will allow for projection of possible photooxidation products that could be produced in this ecosystem. This body of work will allow for the environmental impact of titanium dioxide to be evaluated for the modern era.

A.2 Scientific Objectives

- **General:** Evaluate the photo-oxidative effects of titanium dioxide nanoparticles under environmentally relevant conditions.
- **Specific Aim 1:** Measure the photooxidation products of anthracene by sensitized titanium dioxide nanoparticles under UV-A, UV-B, and visible irradiation.
- **Specific Aim 2:** Quantify the photodegradation of environmentally present PAHs by titanium dioxide nanoparticles.

A.3 Previous Work

A.3.1 Titanium Dioxide Photooxidation

Over one million metric tons of titanium dioxide has been produced annually since 1950 for use as food additives and pigments.[136-138] These additives were largely comprised of micron sized particles; however, recently there has been a sharp increase in nanoscopic titanium dioxide production (Figure A.1).[136, 139] Within the context of photocatalysis, titanium dioxide has been researched for many years and is known to catalyze oxidation reactions under exposure to ultraviolet light.[140-142] In addition to their inherent photocatalytic properties, titanium dioxide nanoparticles are also sensitized by doping methods or molecules on the nanoparticle surface, allowing for oxidation to be driven with visible light.[131, 143] While most of these visible photocatalytic systems are confined to research implementations, the increasing presence of nanoscopic titanium dioxide in the environment is reason for assessment. Previously the only risk

assessment of these mass produced particles was performed in 1969 in the context of a food additive before titanium dioxide nanoparticles were being produced.[144] This evaluation of TiO_2 toxicity to humans was only based on a total of five studies that showed little absorption or accumulation of TiO_2 in the digestive process.[136] While it is true that titanium dioxide's insolubility lends itself to low toxicity in mammalian systems,[138, 145, 146] it also lends itself to long term presence in the biosphere and eventual accumulation in aquatic systems.[138] It is here that titanium dioxide particles are no longer bystanders to geochemical processes, but instead have the potential to catalyze them.[147]

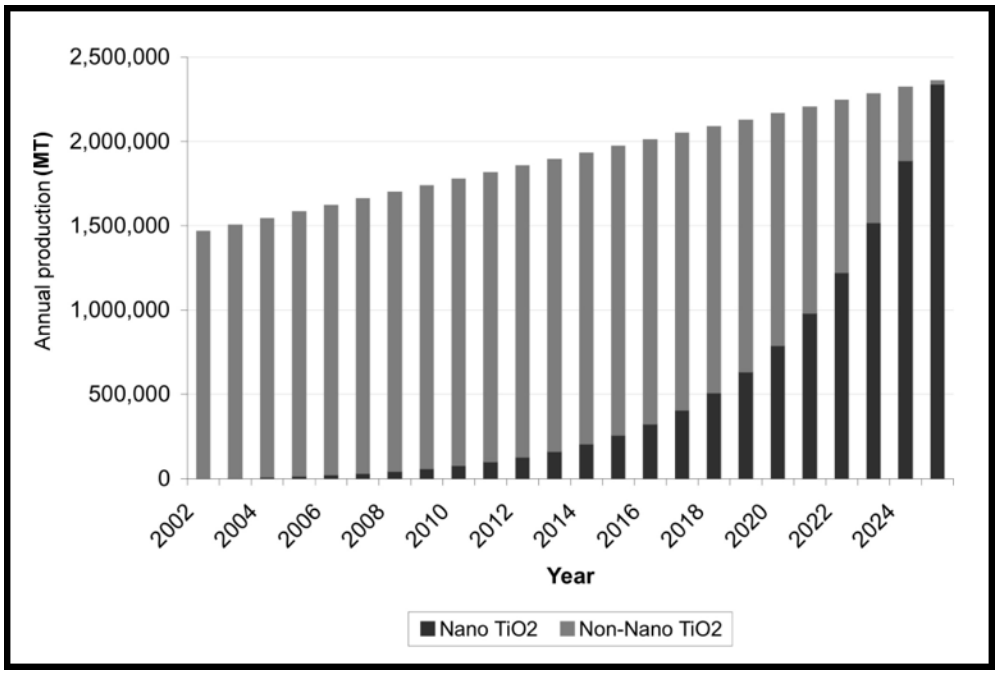

Figure A.1. Projected nano-TiO_2 production as a portion of the total U.S. production. Values shown are an upper limit. Adapted from ref[139]. Copyright 2009 American Chemical Society.

The photocatalytic activity of TiO_2 nanoparticles is well known and heavily researched. In the majority of systems UV radiation is used to excited the TiO_2 nanoparticles to drive oxidation and/or degradation of organic molecular species. However, in some situation TiO_2 nanoparticles

can become sensitized to visible light by small molecules binding to the surface.[134, 148] One example of this is hydrogen peroxide, which can also be found in some aquatic systems. Upon association with TiO_2, hydrogen peroxide binds and forms >Ti-OOH surface species.[131] Due to the affinity of H_2O_2 for the TiO_2 surfaces, this process happens readily even under low concentrations of H_2O_2 (Figure A.2). This results in increased absorbance in the visible region between 400-420 nm. When these sensitized particles are exposed to visible light excited electrons

at the surface can transfer to the conduction band of TiO_2 where it can readily transfer to electron acceptors in the solution resulting in reactive radical species.[131]

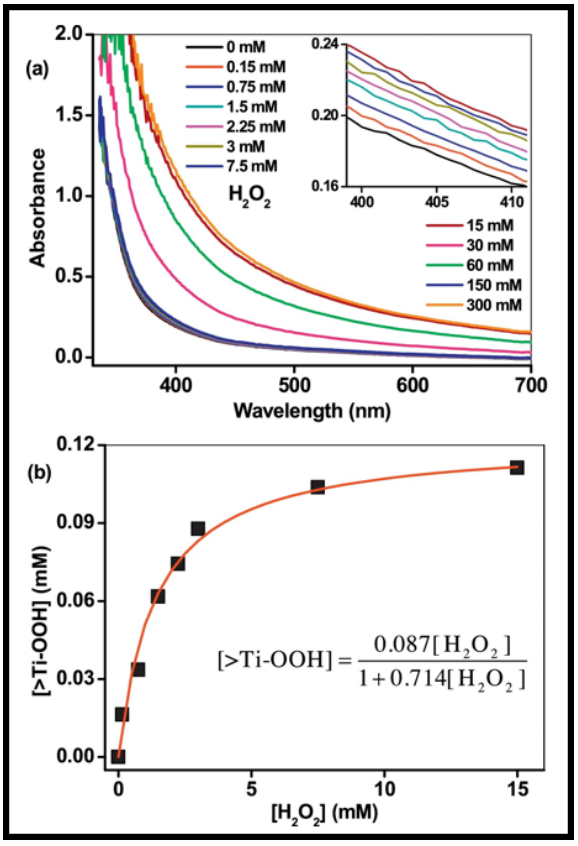

Figure A.2. a) Absorbance of TiO_2 sol as a function of H_2O_2 concentration. b) Concentration of Ti-OOH surface species as a function of H_2O_2 concentration. Adapted from ref[131]. Copyright 2016 Elsevier B.V.

A.4.2 Polycyclic Aromatic Hydrocarbons

In environmental systems there is plenty of molecular candidates for photocatalytic degradation by titanium dioxide; however, we will focus specifically on polycyclic aromatic hydrocarbons (PAHs) due to their prevalence in polluted environments. This wide class of organic compounds occurs naturally and are produced anthropogenically.[149, 150] The most prevalent source of anthropogenically produced PAHs is combustion. Thus concentrations vary significantly from rural to urban areas depending on both automobile traffic and industrial activity.[151] These volatile organic compounds exist readily in the atmosphere both in gas and associated with airborne particulates.[152] It has also been found that around urbanized waterfront areas PAHs are present in both the sediment and the water column, with increased levels in areas with high boat traffic.[153] This group of compounds is of particular interest because many of them are known carcinogens and can cause paralysis in aquatic invertebrates.[154, 155]

Additionally, it has been shown that under sunlight PAHs can undergo rapid structural photomodification, generally via oxidation reactions.[130] These PAH photoproducts range in toxicity and reactivity; they include anthraquinones, benzoic acids, benzaldehydes and phenols (Figure A.3). With an increased presence of TiO_2 nanoparticles in the environment, it is important to evaluate the reactivity and photoproducts of PAH degradation in these systems. To this effect, previous studies have investigate PAH degradation in the presence of TiO_2 but have done little to go beyond a simple demonstration of principle. For this reason a more systematic, comprehensive analytical study is necessary.

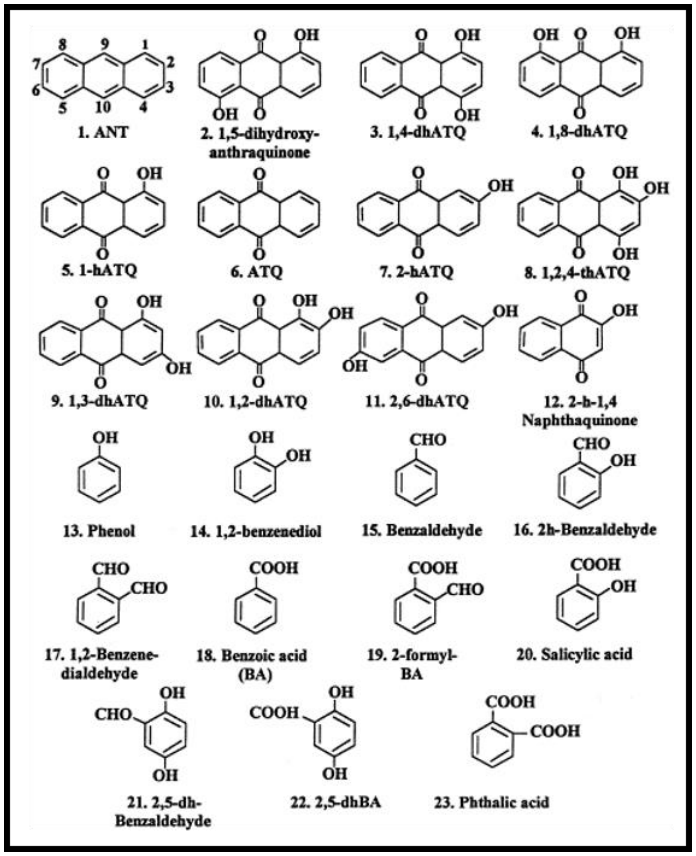

Figure A.3. Products of photooxidation of anthracene under simulated sunlight exposure for 9 hours. Adapted from ref[130]. Copyright 2000 Elsevier B.V.

A.4 Research Effort

The question this research poses is what effect the shift to nanosized titanium dioxide will have on the environments they end up in. With the increased production in nanoscale titanium dioxide, eventual accumulation in the biosphere is inevitable. The most likely environment to find these inert particles are aquatic ones. In addition to the photocatalytic properties of the titanium dioxide particles themselves, aquatic environments contain molecular species that can further sensitize the particles to visible irradiation. The most likely candidates in these environments to be

oxidized by this process are PAHs, which are known to photo-oxidize under ultraviolet light on their own.

The first proposed experiment aims to investigate which specific photoproducts can be generated by hydrogen peroxide sensitized titanium dioxide nanoparticles in the presence of PAHs. To this effect, colloidal solutions of titanium dioxide nanoparticles will be used as the photocatalyst. Ideally nanoparticles with sizes ranging from 10 nm to 100 nm will be tested systematically to determine any size effects on the catalytic activity. Most likely the higher surface area of the smaller particles will result in the highest activity from the 10 nm particles.

The first set of experiments will use 10 nm anatase titanium dioxide nanoparticles with anthracene as the reactant. Anthracene is chosen because it is a representative PAH that is known to be found in the environment and its photooxidation products have been measured previously under UV light.[130] This will allow us to determine if the proliferation of oxidized molecular species is different with and without the presence of titanium dioxide. The reaction will be initiated by a high power white light sources filtered to expose the sample to either UV-A, UV-B, or visible wavelengths. Testing the reactivity under different spectral regions will allow for predictions on reactivities in areas with different light exposure such as terrestrial versus aquatic systems. Along the course of the reaction, 100 μL samples will be taken from the reaction vessel. These small samples will allow for identification and quantification of the generated photoproducts by high performance liquid chromatography (HPLC) techniques which have high precision and sensitivity. Based on reactivities measure in similar systems, the reaction should be carried out for

approximately 8 hours for most of the anthracene to have reacted, samples taken every hour will provide a trajectory of the products as the reaction progresses.

An HPLC analysis of the small sample taken during the reaction will be used to identify and quantify the photoproducts. To accomplish this previously documented methods used to identify the photooxidation products of anthracene will be used.[130] This involves loading the sample in a Superlco LC-18 column with 5 µm particle size and running the column with an acetonitrile: water gradient at 1% acetonitrile for 2 minutes, which is then increased linearly to 90% acetonitrile over the course of 32 minutes, then held at 90% for 20 minutes with a consistent flow rate of 1 mL/min.[130] A UV-visible detection system is used to measure the separated photoproducts as they come of the column for identification and quantification. The data obtained through these methods can then be directly compared to the photoproducts of anthracene photooxidation on its own to determine the effects of titanium dioxide nanoparticle additions.

With this base case established we can then explore the dependence of reactivity on the presence of hydrogen peroxide as a representative small molecule sensitizer. Repeating the above experiment and analysis with various concentrations of hydrogen peroxide in the solution will allow us to quantify any acceleration of the reaction dependent on its presence. It is expected that the addition of H_2O_2 will increase reaction rates under visible light exposure, but it is unclear if it will have a significant effect compared to bare TiO_2 nanoparticles under UV excitation. In these experiments it will also be important to control the pH of the solution. Under different pH the TiO_2 nanoparticles will have a different balance between OH and O^- groups on the surface. In some

environments this could lead to the acceleration or limiting of hydrogen dependent oxidation reactions.

With the experiments outlined above we will be able to measure and quantify the degree to which TiO_2 nanoparticles effect the reactivity of anthracene under UV-A, UV-B, and visible light exposure. In addition, by independently varying the hydrogen peroxide concentration, we will be able to explore the possibility of TiO_2 sensitization in the environment and its possible role in the overall reactivity and products. With this established, pH can be systematically sampled to begin to understand the role varying environmental conditions can have on the reactivity of this system.

While the experiments above will provide a detail picture of the possible photoproducts for anthracene, a more direct effort is needed to determine reactivity of TiO_2 nanoparticles in actual aquatic environments. To this effect, an urban aquatic environment will be modeled. This is a suitable choice for a first examination of this system since both TiO_2 nanoparticles and PAHs are present in significant quantities in these areas. The important difference in these environments compared to the initial experiments is the population of PAHs extends beyond just anthracene. While these molecules are similar, their degradation may vary considerably in these reactions. With this in mind the environmental system will be modeled with the set of 16 priority PAHs (Figure A.4).[156] All of these PAHs are known to be found in polluted environments and have standardized analytical methods for their quantification.[157] These methods utilize standard gas chromatography mass spectrometry (GC/MS) techniques that are highly sensitive and can measure the molecular concentrations of PAHs at the parts per billion level. This amount of sensitivity will

allow us to perform detailed degradation studies on this wide range of PAHs to estimate their reactivity in these aquatic environments.

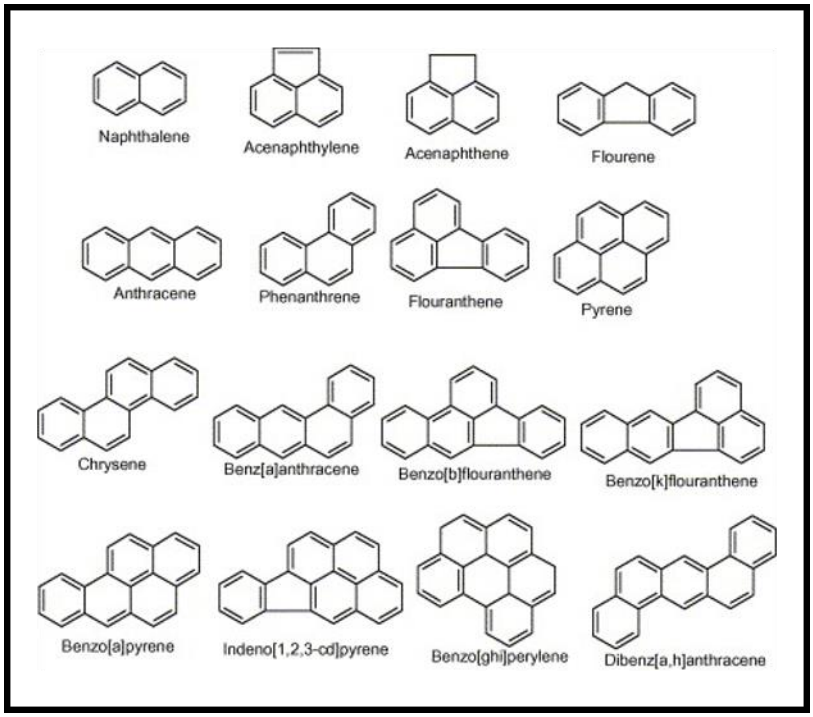

Figure A.4. Representative set of PAHs found in the environment. Ref[156]

Successfully recreating a complex aquatic ecosystem in a laboratory environment is exceedingly difficult. Thus, to accomplish this environmental comparison we will settle for control of a few key parameters that will most effect the reactivity in this system. As mentioned previously, the first of these parameters will be the concentrations of the PAHs used. As a representative environment we can refer to the concentrations found in Lake Michigan and the associated sediment.[157] The next control parameter will be dissolved mineral levels. The dissolved minerals may not have a large influence on the reactivity directly, but the ionic strength of the water will

have an impact on the pH and its variance. Which leads to the third parameter, pH level. This parameter is important because it effects the ultimate speciation of the TiO_2 surface and the ionic species in solution. With these parameters set we should be able to mirror reactivity in the actual aquatic ecosystem. From here the concentration of hydrogen peroxide and titanium dioxide nanoparticles will adjusted to levels found in the environment. The system will be exposed to simulated sunlight during daylight hours for 1 week. Each day a 1 mL aliquot of water will be removed from the reaction vessel to measure the remaining concentration of PAHs in solution. This will enable a detailed picture of the degradation process for the overall population of PAHs. Using the data and experience from the previous studies on anthracene, possible photoproducts for the other degraded PAHs can be predicted. By increasing titanium dioxide nanoparticle concentrations, future environmental conditions can be modeled. Since TiO_2 nanoparticles are inert, their concentration in the biosphere will be ever increasing which may pose a future threat. The extent of this threat can be predicted through this body of work allowing for appropriate regulation and oversite of these materials.

A.5 Conclusions

Titanium dioxide is naturally occurring and is widely produced for commercial products ranging from toothpaste to sunscreen.[158, 159] About 6 million metric tons are produced annually and recent production has had a marked shift towards TiO_2 in its nano-form.[136, 137, 159] The photoactivity of TiO_2 has been heavily investigated in terms of photocatalysis, but comprehensive studies concerning reactivity in the environment are limited.[147] In hopes of

realizing the environmental impact of increased production of TiO_2 nanoparticles, the proposed research will study the photoproducts of anthracene oxidation under UV-A, UV-B, and visible light in the presence of TiO_2. By varying the size of nanoparticles, pH, and presence of sensitizing molecules such as hydrogen peroxide, possible reaction pathways and conditions for reactivity can be mapped. With this information a comprehensive study of PAH degradation will developed. By tracking 16 priority PAHs in a simulated urban aquatic environment upon exposure to simulated sunlight, we can predict activity of TiO_2 nanoparticles in the environment to evaluate their ability to degrade PAHs and uncover any possible toxic photoproducts.

References

1. Pitarke, J. M.; Silkin, V. M.; Chulkov, E. V.; Echenique, P. M., *Reports on Progress in Physics* **2007,** *70* (1), 1-87.

2. Henry, A.-I.; Bingham, J. M.; Ringe, E.; Marks, L. D.; Schatz, G. C.; Van Duyne, R. P., *The Journal of Physical Chemistry C* **2011,** *115* (19), 9291-9305.

3. Haes, A. J.; Haynes, C. L.; McFarland, A. D.; Schatz, G. C.; Van Duyne, R. P.; Zou, S., *MRS Bulletin* **2005,** *30* (5), 368-375.

4. Piliarik, M.; Vaisocherová, H.; Homola, J., **2005,** *20* (10), 2104-2110.

5. Rahn, J.; Hallock, R., *Langmuir* **1995,** *11* (2), 650-654.

6. Vasa, P.; Wang, W.; Pomraenke, R.; Lammers, M.; Maiuri, M.; Manzoni, C.; Cerullo, G.; Lienau, C., *Nature Photonics* **2013,** *7* (2), 128-132.

7. Pala, R. A.; Shimizu, K. T.; Melosh, N. A.; Brongersma, M. L., *Nano Letters* **2008,** *8* (5), 1506-1510.

8. Haynes, C. L.; Van Duyne, R. P., *The Journal of Physical Chemistry B* **2001,** *105* (24), 5599-5611.

9. Ringe, E.; McMahon, J. M.; Sohn, K.; Cobley, C.; Xia, Y.; Huang, J.; Schatz, G. C.; Marks, L. D.; Van Duyne, R. P., *The Journal of Physical Chemistry C* **2010,** *114* (29), 12511-12516.

10. Wriedt, T., Mie Theory: A Review. Springer Berlin Heidelberg: 2012; pp 53-71.

11. Schatz, G. C.; Young, M. A.; Duyne, R. P., Electromagnetic Mechanism of SERS. Springer Berlin Heidelberg: pp 19-45.

12. Jeanmaire, D. L.; Van Duyne, R. P., *Journal of Electroanalytical Chemistry and Interfacial Electrochemistry* **1977,** *84* (1), 1-20.

13. Kleinman, S. L.; Sharma, B.; Blaber, M. G.; Henry, A.-I.; Valley, N.; Freeman, R. G.; Natan, M. J.; Schatz, G. C.; Van Duyne, R. P., *Journal of the American Chemical Society* **2013,** *135* (1), 301-308.

14. Baldelli, S.; Eppler, A. S.; Anderson, E.; Shen, Y.-R.; Somorjai, G. A., *The Journal of Chemical Physics* **2000,** *113* (13), 5432.

15. Li, Q.; Kuo, C. W.; Yang, Z.; Chen, P.; Chou, K. C., *Physical Chemistry Chemical Physics* **2009,** *11* (18), 3436.

16. Frontiera, R. R.; Henry, A. I.; Gruenke, N. L.; Van Duyne, R. P., *J. Phys. Chem. Lett.* **2011,** *2* (10), 1199-1203.

17. Steuwe, C.; Kaminski, C. F.; Baumberg, J. J.; Mahajan, S., *Nano Letters* **2011,** *11* (12), 5339-5343.

18. Kundu, J.; Le, F.; Nordlander, P.; Halas, N. J., **2008,** *452* (1-3), 115-119.

19. Fort, E.; Grésillon, S., *Journal of Physics D: Applied Physics* **2008,** *41* (1), 013001.

20. Christopher, P.; Moskovits, M., *Annual Review of Physical Chemistry* **2017,** (ASAP).

21. Raman, C. V., *Transactions of the Faraday Society* **1929,** *25*, 781-792.

22. Kip, B. J.; Meier, R. J., *Appl. Spectrosc.* **1990,** *44* (4), 707-711.

23. Smith, J. D.; Cappa, C. D.; Drisdell, W. S.; Cohen, R. C.; Saykally, R. J., *Journal of the American Chemical Society* **2006,** *128* (39), 12892-12898.

24. Masango, S. S.; Hackler, R. A.; Large, N.; Henry, A.-I.; McAnally, M. O.; Schatz, G. C.; Stair, P. C.; Van Duyne, R. P., *Nano Letters* **2016,** *16* (7), 4251-4259.

25. Clark, R. J. H.; Dines, T. J., *Angewandte Chemie International Edition in English* **1986,** *25* (2), 131-158.

26. Myers, A. B.; Harris, R. A.; Mathies, R. A., *Journal of Chemical Physics* **1983,** *79* (2), 603-613.

27. Inagaki, F.; Tasumi, M.; Miyazawa, T., *J. Mol. Spectrosc.* **1974,** *50* (1-3), 286-303.

28. McFarland, A. D.; Young, M. A.; Dieringer, J. A.; Van Duyne, R. P., *Journal of Physical Chemistry B* **2005,** *109* (22), 11279-11285.

29. Iwata, K.; Hamaguchi, H.-o., *The Journal of Physical Chemistry A* **1997,** *101* (4), 632-637.

30. Everall, N.; Hahn, T.; Matousek, P.; Parker, A. W.; Towrie, M., *Appl. Spectrosc.* **2001,** *55* (12), 1701-1708.

31. Iwata, K.; Hamaguchi, H.-O., *Chemical Physics Letters* **1992,** *196* (5), 462-468.

32. Kash, J. A.; Tsang, J. C.; Hvam, J. M., *Physical Review Letters* **1985,** *54* (19), 2151-2154.

33. Doig, S. J.; Reid, P. J.; Mathies, R. A., *The Journal of Physical Chemistry* **1991,** *95* (16), 6372-6379.

34. Kwok, W. M.; Ma, C.; Matousek, P.; Parker, A. W.; Phillips, D.; Toner, W. T.; Towrie, M.; Umapathy, S., *The Journal of Physical Chemistry A* **2001,** *105* (6), 984-990.

35. Frischkorn, C.; Wolf, M., *Chemical Reviews* **2006,** *106* (10), 4207-4233.

36. Knight, M. W.; Sobhani, H.; Nordlander, P.; Halas, N. J., *Science* **2011,** *332* (6030), 702-704.

37. Mukherjee, S.; Libisch, F.; Large, N.; Neumann, O.; Brown, L. V.; Cheng, J.; Lassiter, J. B.; Carter, E. A.; Nordlander, P.; Halas, N. J., *Nano letters* **2012,** *13* (1), 240-247.

38. Willets, K. A.; Van Duyne, R. P., *Annu. Rev. Phys. Chem.* **2007,** *58*, 267-297.

39. Dai, Z.; Xiao, X.; Zhang, Y.; Ren, F.; Wu, W.; Zhang, S.; Zhou, J.; Mei, F.; Jiang, C., *Nanotechnology* **2012,** *23* (33), 335701.

40. Sun, M.; Zhang, Z.; Zheng, H.; Xu, H., *Scientific Reports* **2012,** *2*, 647.

41. Xu, P.; Kang, L.; Mack, N. H.; Schanze, K. S.; Han, X.; Wang, H.-L., *Scientific Reports* **2013,** *3*, 2997.

42. Tang, X.; Cai, W.; Yang, L.; Liu, J., *Nanoscale* **2014,** *6* (15), 8612-8616.

43. Sun, M.; Xu, H., *Small* **2012,** *8* (18), 2777-2786.

44. Lee, Y. K.; Jung, C. H.; Park, J.; Seo, H.; Somorjai, G. A.; Park, J. Y., *Nano letters* **2011,** *11* (10), 4251-4255.

45. Qian, K.; Sweeny, B. C.; Johnston-Peck, A. C.; Niu, W.; Graham, J. O.; DuChene, J. S.; Qiu, J.; Wang, Y.-C.; Engelhard, M. H.; Su, D., *Journal of the American Chemical Society* **2014,** *136* (28), 9842-9845.

46. Christopher, P.; Moskovits, M., *Annual Review of Physical Chemistry* **2017,** *68* (1), 379-398.

47. Linic, S.; Christopher, P.; Ingram, D. B., *Nature Materials* **2011,** *10*, 911.

48. Brongersma, M. L.; Halas, N. J.; Nordlander, P., *Nature Nanotechnology* **2015,** *10* (1), 25-34.

49. Zhan, C.; Chen, X.-J.; Yi, J.; Li, J.-F.; Wu, D.-Y.; Tian, Z.-Q., *Nature Reviews Chemistry* **2018**, 1.

50. Thomann, I.; Pinaud, B. A.; Chen, Z.; Clemens, B. M.; Jaramillo, T. F.; Brongersma, M. L., *Nano Letters* **2011,** *11* (8), 3440-3446.

51. Wu, K.; Chen, J.; McBride, J. R.; Lian, T., *Science* **2015,** *349* (6248), 632-635.

52. Clavero, C., *Nature Photonics* **2014,** *8* (2), 95-103.

53. Jin, R.; Cao, Y. C.; Hao, E.; Métraux, G. S.; Schatz, G. C.; Mirkin, C. A., *Nature* **2003,** *425* (6957), 487.

54. Mubeen, S.; Lee, J.; Singh, N.; Krämer, S.; Stucky, G. D.; Moskovits, M., *Nature nanotechnology* **2013,** *8* (4), 247.

55. Nguyen, V.-Q.; Ai, Y.; Martin, P.; Lacroix, J.-C., *ACS Omega* **2017,** *2* (5), 1947-1955.

56. Lee, S. J.; Piorek, B. D.; Meinhart, C. D.; Moskovits, M., *Nano Letters* **2010,** *10* (4), 1329-1334.

57. Christopher, P.; Xin, H.; Linic, S., *Nature Chemistry* **2011,** *3*, 467.

58. Christopher, P.; Xin, H.; Marimuthu, A.; Linic, S., *Nature materials* **2012,** *11* (12), 1044.

59. Mukherjee, S.; Libisch, F.; Large, N.; Neumann, O.; Brown, L. V.; Cheng, J.; Lassiter, J. B.; Carter, E. A.; Nordlander, P.; Halas, N. J., *Nano Letters* **2013,** *13* (1), 240-247.

60. Lee, J.; Mubeen, S.; Ji, X.; Stucky, G. D.; Moskovits, M., *Nano Letters* **2012,** *12* (9), 5014-5019.

61. Gieseking, R. L.; Ratner, M. A.; Schatz, G. C., *Frontiers of Plasmon Enhanced Spectroscopy* **2016,** *1*, 1-22.

62. Boerigter, C.; Aslam, U.; Linic, S., *ACS Nano* **2016,** *10* (6), 6108-6115.

63. Sprague-Klein, E. A.; McAnally, M. O.; Zhdanov, D. V.; Zrimsek, A. B.; Apkarian, V. A.; Seideman, T.; Schatz, G. C.; Van Duyne, R. P., *Journal of the American Chemical Society* **2017,** *139* (42), 15212-15221.

64. Sprague-Klein, E. A.; Negru, B.; Madison, L. R.; Coste, S. C.; Rugg, B. K.; Felts, A. M.; McAnally, M. O.; Banik, M.; Apkarian, V. A.; Wasielewski, M. R., *Journal of the American Chemical Society* **2018**.

65. Brandt, N. C.; Keller, E. L.; Frontiera, R. R., *The journal of physical chemistry letters* **2016,** *7* (16), 3179-3185.

66. Dombi, P. t.; Hörl, A.; Rácz, P. t.; Márton, I. n.; Trügler, A.; Krenn, J. R.; Hohenester, U., *Nano letters* **2013,** *13* (2), 674-678.

67. Kang, L.; Xu, P.; Zhang, B.; Tsai, H.; Han, X.; Wang, H.-L., *Chemical Communications* **2013,** *49* (33), 3389-3391.

68. Keller, E. L.; Frontiera, R. R., *ACS Nano* **2018,** *12* (6), 5848-5855.

69. Hartland, G. V., *Chemical reviews* **2011,** *111* (6), 3858-3887.

70. Hartland, G. V., *The Journal of Chemical Physics* **2002,** *116* (18), 8048-8055.

71. Johnson, F. P.; George, M. W.; Hartl, F.; Turner, J. J., *Organometallics* **1996,** *15*, 3374-3387.

72. Schneider, T. W.; Ertem, M. Z.; Muckerman, J. T.; Angeles-Boza, A. M., *ACS Catalysis* **2016,** *6* (8), 5473-5481.

73. Keith, J. A.; Grice, K. A.; Kubiak, C. P.; Carter, E. A., *Journal of the American Chemical Society* **2013,** *135* (42), 15823-15829.

74. Paolucci, F.; Marcaccio, M.; Paradisi, C.; Roffia, S.; Bignozzi, C. A.; Amatore, C., *The Journal of Physical Chemistry B* **1998,** *102* (24), 4759-4769.

75. Grice, K. A.; Gu, N. X.; Sampson, M. D.; Kubiak, C. P., *Dalton Transactions* **2013,** *42* (23), 8498-8503.

76. Negru, B.; McAnally, M. O.; Mayhew, H. E.; Ueltschi, T. W.; Peng, L.; Sprague-Klein, E. A.; Schatz, G. C.; Van Duyne, R. P., *The Journal of Physical Chemistry C* **2017,** *121* (48), 27004-27008.

77. Vander Ende, E.; Bourgeois, M. R.; Henry, A.-I.; Chávez, J. L.; Krabacher, R.; Schatz, G. C.; Van Duyne, R. P., *Anal. Chem.* **2019,** *91* (15), 9554-9562.

78. Keller, E. L.; Frontiera, R. R., *ACS Photonics* **2017**.

79. Link, S.; Burda, C.; Wang, Z. L.; El-Sayed, M. A., *The Journal of Chemical Physics* **1999,** *111* (3), 1255-1264.

80. Nakamura, I.; Takahashi, A.; Fujitani, T., *Catalysis letters* **2009,** *129* (3-4), 400-403.

81. Stacy, A. A.; Van Duyne, R. P., *Chemical Physics Letters* **1983,** *102* (4), 365-370.

82. Yu, Y.; Wijesekara, K. D.; Xi, X.; Willets, K. A., *ACS Nano* **2019**.

83. Carregal-Romero, S.; Pérez-Juste, J.; Hervés, P.; Liz-Marzán, L. M.; Mulvaney, P., *Langmuir* **2010,** *26* (2), 1271-1277.

84. Kim, Y.; Dumett Torres, D.; Jain, P. K., *Nano letters* **2016,** *16* (5), 3399-3407.

85. Kim, Y.; Wilson, A. J.; Jain, P. K., *ACS Catalysis* **2017,** *7* (7), 4360-4365.

86. Lowry, R., *Journal of Raman spectroscopy* **1991,** *22* (12), 805-809.

87. Hirsch, L. R.; Stafford, R. J.; Bankson, J. A.; Sershen, S. R.; Rivera, B.; Price, R. E.; Hazle, J. D.; Halas, N. J.; West, J. L., *Proceedings of the National Academy of Sciences* **2003,** *100* (23), 13549-13554.

88. Zharov, V. P.; Mercer, K. E.; Galitovskaya, E. N.; Smeltzer, M. S., **2006,** *90* (2), 619-627.

89. RöNtzsch, L.; Heinig, K.-H.; Schuller, J. A.; Brongersma, M. L., **2007,** *90* (4), 044105.

90. Neumann, O.; Urban, A. S.; Day, J.; Lal, S.; Nordlander, P.; Halas, N. J., *ACS Nano* **2013,** *7* (1), 42-49.

91. Neumann, O.; Feronti, C.; Neumann, A. D.; Dong, A.; Schell, K.; Lu, B.; Kim, E.; Quinn, M.; Thompson, S.; Grady, N.; Nordlander, P.; Oden, M.; Halas, N. J., *Proceedings of the National Academy of Sciences* **2013,** *110* (29), 11677-11681.

92. Clavero, C., *Nature Photonics* **2014,** *8*, 95.

93. Kettle, S. F. A.; Aschero, G. L.; Diana, E.; Rossetti, R.; Stanghellini, P. L., *Inorganic Chemistry* **2006,** *45* (13), 4928-4937.

94. Korzeniewski, C.; Severson, M. W.; Schmidt, P. P.; Pons, S.; Fleischmann, M., *The Journal of Physical Chemistry* **1987,** *91* (22), 5568-5573.

95. Keller, E. L.; Kang, H.; Haynes, C. L.; Frontiera, R. R., *ACS Applied Materials & Interfaces* **2018,** *10* (47), 40577-40584.

96. Kukura, P.; McCamant, D. W.; Yoon, S.; Wandschneider, D. B.; Mathies, R. A., *Science* **2005,** *310* (5750), 1006-1009.

97. Frontiera, R. R.; Gruenke, N. L.; Van Duyne, R. P., *Nano Letters* **2012,** *12* (11), 5989-5994.

98. Gruenke, N. L.; McAnally, M. O.; Schatz, G. C.; Van Duyne, R. P., *The Journal of Physical Chemistry C* **2016,** *120* (51), 29449-29454.

99. Tchebotareva, A. L.; Van Dijk, M. A.; Ruijgrok, P. V.; Fokkema, V.; Hesselberth, M. H.; Lippitz, M.; Orrit, M., *ChemPhysChem* **2009,** *10* (1), 111-114.

100. Brown, A. M.; Sundararaman, R.; Narang, P.; Schwartzberg, A. M.; Goddard III, W. A.; Atwater, H. A., *Physical Review Letters* **2017,** *118* (8), 087401.

101. Kirschner, M. S.; Lethiec, C. M.; Lin, X.-M.; Schatz, G. C.; Chen, L. X.; Schaller, R. D., *ACS Photonics* **2016,** *3* (5), 758-763.

102. Frontiera, R. R.; Mathies, R. A., *Laser & Photonics Reviews* **2011,** *5* (1), 102-113.

103. Kukura, P.; McCamant, D. W.; Mathies, R. A., *Annu. Rev. Phys. Chem.* **2007,** *58*, 461-488.

104. Ploetz, E.; Gellner, M.; Schütz, M.; Marx, B.; Schlücker, S.; Gilch, P. In *Surface Enhancement in Femtosecond Stimulated Raman Scattering*, American Institute of Physics Conference Series, 2010; pp 88-89.

105. Frontiera, R. R.; Henry, A.-I.; Gruenke, N. L.; Van Duyne, R. P., *The journal of physical chemistry letters* **2011,** *2* (10), 1199-1203.

106. Gruenke, N. L.; McAnally, M. O.; Schatz, G. C.; Van Duyne, R. P., **2016**.

107. Chen, J. K.; Tzou, D. Y.; Beraun, J. E., *International Journal of Heat and Mass Transfer* **2006,** *49* (1-2), 307-316.

108. Chikkaraddy, R.; de Nijs, B.; Benz, F.; Barrow, S. J.; Scherman, O. A.; Rosta, E.; Demetriadou, A.; Fox, P.; Hess, O.; Baumberg, J. J., *Nature* **2016,** *535* (7610), 127-130.

109. Rodarte, A. L.; Tao, A. R., *J. Phys. Chem. C* **2017,** *121* (6), 3496-3502.

110. Schlather, A. E.; Large, N.; Urban, A. S.; Nordlander, P.; Halas, N. J., *Nano Letters* **2013,** *13* (7), 3281-3286.

111. Zengin, G.; Johansson, G.; Johansson, P.; Antosiewicz, T. J.; Kall, M.; Shegai, T., *Scientific Reports* **2013,** *3*, 8.

112. Balci, S.; Kucukoz, B.; Balci, O.; Karatay, A.; Kocabas, C.; Yaglioglu, G., *ACS Photonics* **2016,** *3* (11), 2010-2016.

113. Stete, F.; Koopman, W.; Bargheer, M., *ACS Photonics* **2017,** *4* (7), 1669-1676.

114. Santhosh, K.; Bitton, O.; Chuntonov, L.; Haran, G., *Nature Communications* **2016,** *7*, 5.

115. Wen, J.; Wang, H.; Wang, W.; Deng, Z.; Zhuang, C.; Zhang, Y.; Liu, F.; She, J.; Chen, J.; Chen, H.; Deng, S.; Xu, N., *Nano Letters* **2017,** *17* (8), 4689-4697.

116. Cuadra, J.; Baranov, D. G.; Wersall, M.; Verre, R.; Antosiewicz, T. J.; Shegai, T., *Nano Letters* **2018,** *18* (3), 1777-1785.

117. Stührenberg, M.; Munkhbat, B.; Baranov, D. G.; Cuadra, J.; Yankovich, A. B.; Antosiewicz, T. J.; Olsson, E.; Shegai, T., *Nano Letters* **2018**.

118. Lin, L. H.; Wang, M. S.; Wei, X. L.; Peng, X. L.; Xie, C.; Zheng, Y. B., *Nano Letters* **2016,** *16* (12), 7655-7663.

119. Hsu, L. Y.; Ding, W. D.; Schatz, G. C., *J. Phys. Chem. Lett.* **2017,** *8* (10), 2357-2367.

120. Nan, F.; Ding, S. J.; Ma, L.; Cheng, Z. Q.; Zhong, Y. T.; Zhang, Y. F.; Qiu, Y. H.; Li, X. G.; Zhou, L.; Wang, Q. Q., *Nanoscale* **2016,** *8* (32), 15071-15078.

121. Hutchison, J. A.; Schwartz, T.; Genet, C.; Devaux, E.; Ebbesen, T. W., *Angew. Chem.-Int. Edit.* **2012,** *51* (7), 1592-1596.

122. Galego, J.; Garcia-Vidal, F. J.; Feist, J., *Nature Communications* **2016,** *7*, 6.

123. Stranius, K.; Hertzog, M.; Borjesson, K., *Nature Communications* **2018,** *9*, 7.

124. Rudin, S.; Reinecke, T. L., *Physical Review B* **1999,** *59* (15), 10227-10233.

125. Hennessy, K.; Badolato, A.; Winger, M.; Gerace, D.; Atature, M.; Gulde, S.; Falt, S.; Hu, E. L.; Imamoglu, A., *Nature* **2007,** *445* (7130), 896-899.

126. Zrimsek, A. B.; Henry, A.-I.; Van Duyne, R. P., *The Journal of Physical Chemistry Letters* **2013,** *4* (19), 3206-3210.

127. Dieringer, J. A.; Wustholz, K. L.; Masiello, D. J.; Camden, J. P.; Kleinman, S. L.; Schatz, G. C.; Van Duyne, R. P., *Journal of the American Chemical Society* **2009,** *131* (2), 849-854.

128. Aherne, D.; Ledwith, D. M.; Gara, M.; Kelly, J. M., *Advanced Functional Materials* **2008,** *18* (14), 2005-2016.

129. Wang, Y.; Fengkai, L.; Zhulu, L.; Zheng, X.; Yubin, T., *Chemosphere* **1999,** *38* (6), 1273-1278.

130. Mallakin, A.; Dixon, D. G.; Greenberg, B. M., *Chemosphere* **2000,** *40* (12), 1435-1441.

131. Liu, T.; Li, X.; Yuan, X.; Wang, Y.; Li, F., *Journal of Molecular Catalysis A: Chemical* **2016,** *414*, 122-129.

132. Seo, J.; Lee, H.; Lee, H.-J.; Kim, M. S.; Hong, S. W.; Lee, J.; Cho, K.; Choi, W.; Lee, C., *Applied Catalysis B: Environmental* **2018,** *225*, 487-495.

133. Zhang, L.; Li, P.; Gong, Z.; Li, X., *Journal of Hazardous Materials* **2008,** *158* (2-3), 478-484.

134. Williamson, C. E.; Stemberger, R. S.; Morris, D. P.; Frost, T. M.; Paulsen, S. G., **1996,** *41* (5), 1024-1034.

135. Vione, D.; Maurino, V.; Minero, C.; Pelizzetti, E.; Harrison, M. A.; Olariu, R. I.; Arsene, C., *Chem Soc Rev* **2006,** *35* (5), 441-53.

136. Jovanović, B., *Integrated environmental assessment and management* **2015,** *11* (1), 10-20.

137. Robichaud, C. O.; Uyar, A. E.; Darby, M. R.; Zucker, L. G.; Wiesner, M. R., *Environmental science & technology* **2009,** *43* (12), 4227-4233.

138. Weir, A.; Westerhoff, P.; Fabricius, L.; Hristovski, K.; von Goetz, N., *Environmental science & technology* **2012,** *46* (4), 2242-2250.

139. Robichaud, C. O.; Uyar, A. E.; Darby, M. R.; Zucker, L. G.; Wiesner, M. R., *Environmental Science & Technology* **2009,** *43* (12), 4227-4233.

140. Peng, T.; Zhao, D.; Dai, K.; Shi, W.; Hirao, K., *The Journal of Physical Chemistry B* **2005,** *109* (11), 4947-4952.

141. Rodríguez-González, V.; Terashima, C.; Fujishima, A., *Journal of Photochemistry and Photobiology C: Photochemistry Reviews* **2019,** *40*, 49-67.

142. Boehme, M.; Ensinger, W., *Nano-Micro Letters* **2011,** *3* (4), 236-241.

143. Ansari, S. A.; Khan, M. M.; Ansari, M. O.; Cho, M. H., *New Journal of Chemistry* **2016,** *40* (4), 3000-3009.

144. Jovanovic, B., *Integr Environ Assess Manag* **2015,** *11* (1), 10-20.

145. Jani, P.; HALBERT, G. W.; LANGRIDGE, J.; FLORENCE, A. T., *Journal of pharmacy and pharmacology* **1990,** *42* (12), 821-826.

146. Koeneman, B. A.; Zhang, Y.; Westerhoff, P.; Chen, Y.; Crittenden, J. C.; Capco, D. G., *Cell biology and toxicology* **2010,** *26* (3), 225-238.

147. Liu, T.; Li, X.; Yuan, X.; Wang, Y.; Li, F., *Journal of Molecular Catalysis A: Chemical* **2016**.

148. Liu, G.; Sun, C.; Yang, H. G.; Smith, S. C.; Wang, L.; Lu, G. Q.; Cheng, H.-M., *Chem. Commun.* **2010,** *46* (5), 755-757.

149. Khalili, N. R.; Scheff, P. A.; Holsen, T. M., *Atmospheric environment* **1995,** *29* (4), 533-542.

150. Wang, X.-C.; Sun, S.; Ma, H.-Q.; Liu, Y., *Marine Pollution Bulletin* **2006,** *52* (2), 129-138.

151. Benlahcen, K.; Chaoui, A.; Budzinski, H.; Bellocq, J.; Garrigues, P., *Marine Pollution Bulletin* **1997,** *34* (5), 298-305.

152. Vione, D.; Maurino, V.; Minero, C.; Pelizzetti, E.; Harrison, M. A.; Olariu, R.-I.; Arsene, C., *Chemical Society Reviews* **2006,** *35* (5), 441-453.

153. Mastran, T. A.; Dietrich, A. M.; Gallagher, D. L.; Grizzard, T. J., *Water Research* **1994,** *28* (11), 2353-2366.

154. Eisler, R., *US fish and wildlife service biological report* **1987,** *85* (1.11), 81.

155. Baird, W. M.; Hooven, L. A.; Mahadevan, B., *Environmental and molecular mutagenesis* **2005,** *45* (2-3), 106-114.

156. Food; Administration, D., *Part 21 current good manufacturing practice for finished pharmaceuticals United State* **1994**.

157. Huang, L.; Chernyak, S. M.; Batterman, S. A., **2014,** *487*, 173-186.

158. Lademann, J.; Weigmann, H.-J.; Rickmeyer, C.; Barthelmes, H.; Schaefer, H.; Mueller, G.; Sterry, W., *Skin Pharmacology and Physiology* **1999,** *12* (5), 247-256.

159. Chen, X.; Mao, S. S., *Chemical reviews* **2007,** *107* (7), 2891-2959.